

A Low Cost, Self-Acting, Liquid Hydrogen Boil-Off Recovery System

Final Report

Contract NAS13-98018

Prepared for:

National Aeronautics and Space Administration
John C. Stennis Space Center
Stennis space Center, MS 39529-6000

Prepared by:

AFAB Technologies, Inc.

Mailing Address:

P.O. Box 1519
Loxahatchee, FL 33470

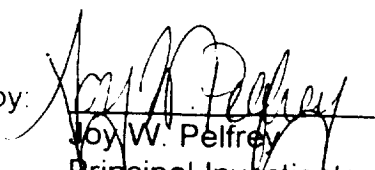
Shipping Address:

11420 Fortune Circle, Suite 3
West Palm Beach, FL 33414

Period Covered:

February 23, 1998 – June 23, 2000

Written by:


Joy W. Pelfrey
Principal Investigator
AFAB Technologies, Inc.

Approved by:


Joy W. Pelfrey
President
AFAB Technologies, Inc.

TABLE OF CONTENTS

<u>Section</u>	<u>Page</u>
PROJECT SUMMARY	1
PROJECT OBJECTIVES	2
Detail Design	2
Final Analysis	2
Hardware Procurement	2
Component Tests	2
System Tests	3
Prototype Tests	3
WORK PERFORMED	4
Detail Design	4
Final Analysis	22
Hardware Procurement	28
Component Tests	29
System Tests	31
Prototype Tests	31
RESULTS OBTAINED	32
Detail Design	32
Final Analysis	37
Hardware Procurement	42
Component Tests	47
System Tests	53
Prototype Tests	57
TECHNICAL MERIT AND FEASIBILITY ASSESSMENT	58
APPENDIX A: A-SIZE DETAIL DRAWINGS	A1
APPENDIX B: CONSULTANTS SENSITIVITY STUDY	B1
APPENDIX C: CONSULTANTS REPORT: ROTORDYNAMIC ANALYSIS	C1
SF298 REPORT DOCUMENTATION PAGE	

LIST OF FIGURES

<u>Figure</u>		<u>Page</u>
1	Initial Compressor Geometry.....	9
2	Turbine Sizing Parametric Study.....	10
3	Turbine Efficiency.....	11
4	Comparison of NBS Baseline Turbine.....	12
5	Radial Pressure Distribution Across Compressor.....	13
6	Radial Pressure Distribution Across Turbine.....	13
7	Final Compressor Geometry.....	15
8	Load Capacity of Spiral Groove Thrust Bearing.....	18
9	Load Capacity of Spiral Groove Thrust Bearing vs. Clearance	19
10	Plexiglas Model Separator.....	20
11	Separator Operation Schematic.....	21
12	Liquid Hydrogen Boil-Off Recovery System Flow Model.....	23
13	Sensitivity of Liquid Production to J-T Valve Inlet Temp.....	24
14	Schematic of Bypass Flow Configuration.....	25
15	Flow Model of Bypass Flow Configuration.....	26
16	Stage Performance of Hydrogen Compressor.....	26
17	Flow Rate vs. Pressure Ratio of Baseline Compressor.....	27
18	Compressor Exit Temperature as a Function of Mass Flow.....	27
19	Compressor Exit Pressure as a Function of Mass Flow.....	28
20	Thermal Contour Plot of Compressor Blades.....	32
21	Stage Performance of Hydrogen Compressor.....	33
22	Flow Rate vs. Pressure Performance.....	33
23	Production Turbine Geometry.....	34
24	Journal Bearing Stiffness vs. Speed and Clearance.....	35
25	Journal Bearing Damping vs. Speed and Clearance.....	36
26	Journal Bearing Load Capacity vs. Speed and Clearance.....	36
27	Compressor-End Journal Bearing Power Loss.....	36
28	Turbine-End Journal Bearing Power Loss.....	37
29	Compressor Efficiency vs. Bypass Flow.....	37
30	Compressor Pressure Ratio vs. Bypass Flow.....	38
31	Liquid Yield vs. Bypass Flow.....	40
32	Cp vs. Temperature for Hydrogen at 14.7 psia.....	41
33	Cp vs. Temperature for Hydrogen at 4.1 atm.....	41
34	Heat Exchanger Length vs. Bypass Flow.....	42
35	Turbocompressor Housing.....	43
36	Journal Bearing.....	44
37	Thrust Bearing.....	44
38	Turbine Nozzle Ring (Scroll).....	45
39	Cover.....	45
40	Rotor.....	46

LIST OF FIGURES CONTINUED

<u>Figure</u>		<u>Page</u>
41	Separator, Heat Exchanger, and Joule-Thompson Valve.....	46
42	Sample Data Acquisition Screen	47
43	Sample Pressure Transducer Calibration Curve	48
44	Journal Bearing Web Springrate	48
45	Flow Parameter: 0.026 inch Diameter Orifice.....	49
46	Flow Parameter: 0.029 inch Diameter Orifice.....	50
47	Flow Parameter: 0.030 inch Diameter Orifice.....	50
48	Flow Parameter: 0.031 inch Diameter Orifice.....	51
49	Flow Parameter: 0.035 inch Diameter Orifice.....	51
50	J-T Factor vs. Flow Parameter for 0.035 Orifice.....	52
51	Heat Exchanger Efficiency vs. Flow Parameter.....	53
52	Turbocompressor Rotor Stack.....	54
53	System Test Setup.....	55
54	Liquid Yield vs. Heat Exchanger Efficiency	56
55	Liquid Yield vs. J-T Factor.....	56
56	Prototype System.....	57

LIST OF TABLES

<u>Table</u>		<u>Page</u>
1	Recovery System List of Parts	5
2	Compressor Operating Conditions	7
3	Impeller Geometry	8
4	Diffuser Geometry	8
5	Scroll or Collector Geometry	8
6	Turbine Design Requirements	9
7	Comparison of NBS Baseline Turbine to Recovery System	11
8	Spiral Groove Thrust Bearing Geometry	18
9	Hydrostatic Thrust Bearing Geometry	19
10	Steady-State, Design Point Results from Flow Model	24
11	Data Acquisition System	30
12	Production Turbine Performance and Operating Conditions	35

Project Summary

Purpose of Research

The purpose of this research was to develop a prototype liquid hydrogen boil-off recovery system. Perform analyses to finalize recovery system cycle, design detail components, fabricate hardware, and conduct sub-component, component, and system level tests leading to the delivery of a prototype system.

Research Conducted and Findings

Design point and off-design analyses, along with a sensitivity study, identified cycle improvements to increase the robustness of the Phase I system by adding a by-pass heat exchanger. All components, including a high-speed, miniature turbocompressor, were designed and manufacturing drawings were created. All hardware was fabricated and tests were conducted in air, helium, and hydrogen. Testing validated the design and analyses, except for the turbocompressor. A rotor-to-stator clearance issue was discovered as a result of a concentricity tolerance stack-up.

Potential Applications

A ground-based cryogenic boil-off recovery system could be used on NASA propellant storage tanks. A flight-weight system could be used to minimize propellant losses for current launch vehicles, the space station, interplanetary missions, and long duration satellites. Non-government applications include cryogenic storage tanks at industrial gas factories, distribution centers and hospitals. A "flight-weight" version could be used on roadable dewars used to transport cryogenics throughout the country.

Project Objectives

During Phase II, our primary objective was to develop a prototype liquid hydrogen boil-off recovery system and place it into service on a Stennis Space Center liquid hydrogen storage tank for demonstration and evaluation. This overall objective has been sub-divided into the following specific objectives:

- Detail Part Design
- Final Analysis
- Hardware Procurement
- Component Tests
- System Tests
- Prototype Tests

Detail Design

Create manufacturing drawings and identify off-the-shelf (OTS) components for all hardware that comprises the liquid hydrogen boil-off recovery system. The major objectives for this effort were the detail design of the compressor and turbine, including the blade geometry, as well as conducting the mechanical design necessary to generate the drawings for the unique hardware.

Final Analysis

Using the cycle and design point performance analysis conducted in Phase I, the objective of this effort was to conduct off-design and transient analysis to ensure the recovery system will function over a wide range of operating conditions, in addition to the laboratory design point. Additionally, this analysis allows the operating envelope, capabilities, and limitations of the recovery system to be identified.

Hardware Procurement

The focus of this objective is to acquire all hardware necessary to conduct sub-component, component, system, and prototype testing. Additionally, this objective will be used to identify manufacturing issues and refine low-volume production cost estimates.

Component Tests

This objective is to test each part at the lowest possible level beginning with sub-components and continuing with components. This approach will identify design or performance issues at the lowest possible level, which improves the

probability of success at higher level system and prototype tests. The bearings, regulator, and Joule-Thompson valves will be tested at the sub-component level. The turbo-compressor, heat exchangers, and separator will be tested at the component level.

System Tests

The components will be assembled into a recovery system. Testing of this system will be conducted with the objective of measuring operating points throughout the cycle. Data will be used to quantify and optimize performance at design point. Off-design point testing will be conducted to quantify the operating envelope.

Prototype Tests

The results from the system tests will be used to identify the prototype configuration and performance. This configuration will be built, tested, and delivered to Stennis Space Center for continued testing and field evaluation in accordance with the primary objective.

Work Performed

Detail Design

The detail design effort consisted of identifying all the hardware that comprises the liquid hydrogen boil-off recovery system. If a suitable off-the-shelf component could not be found, the part was designed and a manufacturing drawing was created. Table 1 lists the resulting bill-of-material for the recovery system.

There are 37 unique parts (part numbers, not total number of pieces) that make-up the recovery system (note that AT98011 and AT98012 are assembly drawings and not parts and AT98010 is an alternate bearing configuration). Of these 38 parts (including the alternate bearing configuration), 30 are off-the-shelf components and 8 were custom designed by AFAB Technologies (A-Size versions of the detail assembly and manufacturing drawings are included as Appendix A).

The eight custom parts are AT98003 – AT98010. AT98009 is the gas/liquid separator used in the recovery system, the remaining custom parts are used in the turbocompressor. Level 1 represents the entire liquid hydrogen boil-off recovery system. Level 2 are all the parts that make-up the recovery system. Level 3 are the parts that make-up the turbocompressor assembly, and Level 4 are the parts that make-up the bearing assembly.

The majority of the design effort was spent on the turbocompressor. As such, the major design features of each custom part will be discussed.

Level	Part Number	Part Name	Description
1	AT98012	Liquid Hydrogen Boil-Off Recovery System	
2	AT98011	Cryogenic Turbocompressor Assembly	
3	AT98003	Rotor	
3	AT98004	Bearing, Tilting Pad	
4	D12-2	Pin, Dowel	Brg. Pad Actuator
4	SC2-51	Screw, Set	Brg. Pad Adjustment
4	SPR9-1	Spring	Brg. Pad Pre-load
3	AT98005	Housing, Main	
3	AT98006	Cover, Turbocompressor	
3	AT98007	Ring, Turbine Nozzle	
3	AT98008	Bearing, Thrust	
3	AT98010	Bearing, Tilting Pad	Alternate Configuration
3	6757782	Bolt	1/4-28 x 1"L
3	384-129-01-01	Face Seal, Spring Energized	
3	48002-3-15-2-SPA	Seal, Enerring	
3	48005-5-15-2-SPA	Seal, Enerring	
3	MS9193-03	Threaded Boss	
3	MS9193-05	Threaded Boss	
3	A/R	Shim Stock	Stainless Steel
2	AT98009	Separator, Gas/Liquid	
2	413	Heat Exchanger	Exergy, Inc.
2	4ALOK-316	Ferrule, Nut	1/4"
2	4ET4-316	Tee, Fitting	1/4"
2	4FSC4N-316	Adapter	1/4" to 1/4 FNPT
2	4MSC4N-316	Adapter	1/4" to 1/4 MNPT
2	4MSC8N-316	Adapter	1/4" to 1/2 MNPT
2	4NU4-316	Nut, Tubing	1/4"
2	4SC4-316	Union, Fitting	1/4"
2	A/R	Seamless Tubing	316 CRES SS
2	A32	Regulator, Hydrogen	Cash Acme
2	CRMS0063035A	Orifice	Farmington Eng.
2	ECR4-316	Cross	1/4"
2	SS-400-R-3	Adapter	3/16 to 1/4
2	SS-400-R-5	Adapter	5/16 to 1/4
2	A/R	Tape, PTFE	NPT Sealant
2	A/R	Angle	1 1/2"
2	A/R	Bolt	1/4" - 28
2	A/R	Washers, Lock	1/4"
2	A/R	Nut	1/4"
2	A/R	Insulation	

Table 1: Recovery System List of Parts

Turbocompressor

AT98011 is the turbocompressor assembly drawing. To minimize clearance changes due to thermal expansion, it was decided to make the entire turbocompressor out of the same material. Additionally, the material had to be hydrogen compatible and of sufficient strength to react the rotor centrifugal stresses at the initial design point speed of 1.3 million revolutions per minute (RPM). Titanium was attractive from a weight, cost, and machinability perspective; however, the rotor stresses were marginal. Upon further analysis, it was decided to manufacture the turbocompressor from a Titanium alloy (Ti-6Al-4V) for the non-rotating parts and Ti-6Al-4V (ELI) STA for the rotor.

The ELI designates extra low interstitial and the STA is solution treated and aged. The solution heat treat and aging increases the material strength to provide the required structural integrity while maintaining the coefficient of thermal expansion with the non-rotating parts. Note that the detailed finite element thermal and structural analysis was performed in Phase I and documented in AFAB Technologies, Inc. final report number AT97202-3 dated September 15, 1997.

Accounting for thermal expansion (shrinkage), centrifugal growth, desired and/or reasonable operating clearances, and allowance for desired and/or reasonable manufacturing tolerances, diametrical fits, radial clearances, and axial clearances were calculated and added to the assembly drawing. To eliminate a machine-at-assembly operation, the axial distance from the cover flange to the compressor shroud was sized so that it would provide the intended operating clearance with no shim if the housing was machined to minimum material condition (axially) and the remaining parts were machined to maximum material condition axially. Since this is an unlikely scenario, the resulting interference will be compensated for with the addition of a shim between the cover and main housing to achieve the intended axial clearance between the compressor and its shroud.

Each part within the turbocompressor housing is centered and secured radially with an interference fit. Additionally, the entire stack is seated axially with the cover, which is bolted to the main housing with a four-bolt flange secured with ¼"-28x1"L stainless steel bolts. This joint is sealed with a pressure activated, stainless steel spring energized, Teflon jacketed Furon seal (348-129-01-01). This seal provides exceptional performance when used with highly polished seal glands (typically a 4 – 8 micro-inch surface finish is required for hydrogen service). The supply and discharge ports use standard MS9193 bulkhead fittings with Enerring seals (4800x-x-2-SPA).

The internal parts were designed for assembly into the main housing with either an arbor press (a lead-in chamfer is provided in the main housing) or by heating and chilling. A fully assembled turbocompressor can be disassembled as follows. Remove the turbine exhaust fitting and replace with a bolt to constrain main housing axially. Remove the compressor inlet fitting and replace with lifting eye. Remove four flange bolts and pull cover off. Remove compressor end journal bearing with jacking screws (each bearing contains three threaded holes for jacking screws). Remove rotor. Install lifting eye into threaded thrust bearing sleeve. Pull thrust bearing out. Remove turbine end bearing with jacking screws. Remove housing constraining bolt and press nozzle ring out of main housing with arbor press entering from turbine exhaust.

The structural and thermal analysis of the turbocompressor assembly was completed in Phase I.

Rotor

The rotor (AT98003) was designed in four phases. First, the compressor was designed to meet cycle performance requirements resulting in identification of the compressor geometry, blade coordinates, and rotor speed. Second, the journals were sized to match the bearing performance necessary for rotor dynamic stability. Third, the turbine was sized to provide the work to drive the compressor and overcome bearing and rotor windage losses. Forth, the thrust disk was sized to react the axial loads and achieve thrust balance.

The compressor was initially sized using 2-D CFD analysis. The compressor operating conditions are summarized in Table 2. Table 3 list the impeller geometry. As shown in Table 3, the speed was reduced from 1.3 million RPM to 1.1 million RPM. Additionally, the initial compressor design has 25 full-length blades. The blade coordinates are included on the rotor drawing. The parallel wall diffuser and scroll geometry are summarized on Table 4 and Table 5, respectively. Figure 1 is a 3-D model of the resulting, initial compressor design.

Gas	Hydrogen
Inlet Pressure	4.0 atm
Inlet Temperature	26 K
Outlet Pressure	14.6 atm
Outlet Temperature	56.8 K
Mass Flow Rate	1.8 gm/sec
Gas Power	0.5968 Kw

Table 2: *Compressor Operating Conditions*

Direction of Rotation	Clockwise viewed from inlet
Speed	1.1 million RPM
Number of Blades	25
Inlet Hub Diameter	1.524 mm
Inlet Shroud Diameter	2.54 mm
Inlet Mean Blade Angle	38 degrees
Tip Hub/Shroud Diameter	8.89 mm
Outlet Blade Angle	90 degrees
Inlet Blade Thickness	0.0254 mm
Outlet Blade Height	0.1016 mm
Meridional Passage Length	2.00066 mm
Blade Passage Length	2.5146 mm
Surface Finish	1 micro-M (40 micro-inches)
Inlet Shroud Relative Mn	0.42
Tip Mn (U_2/a_0)	1.1
Rotor to Stator Clearance	0.01 mm

Table 3: Impeller Geometry

Type	Vaneless, Parallel Wall
Width	.1016 mm
Inlet Diameter	9.068 mm
Outlet Diameter	13.97 mm
Surface Finish	.3125 micro-M (12.5 micro-inches)

Table 4: Diffuser Geometry

Outlet Diameter	1.88
Outlet Mn	0.17
Area Variation	Linear with Angle
Outlet Diameter of 8 deg. Cone	2.45 mm
Gas Velocity	60 m/sec
Surface Finish	0.3125 micro-m (12.5 micro-inches)

Table 5: Scroll or Collector Geometry

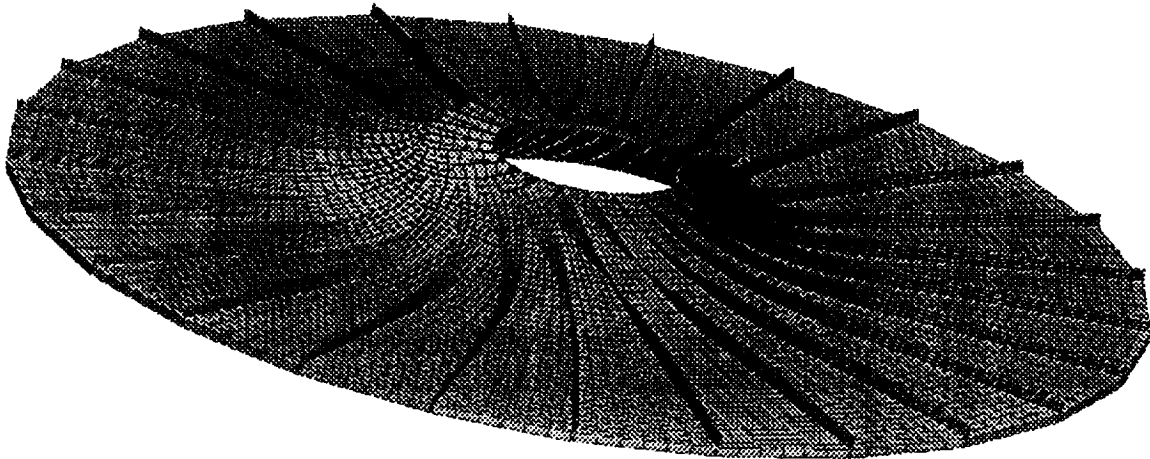


Figure 1: Initial Compressor Geometry

Using this basic design, a range of steady-state operating points were analyzed. The pertinent parameters for off-design compressor performance are: polytropic efficiency, mass flow, exit temperature, and exit pressure. The tip diameter of the compressor establishes the outside diameter of the shaft.

With the initial compressor design completed, the second phase of the rotor design began – journal design. Preliminary bearing designs were completed in Phase I. However, the lower design point speed and final compressor tip diameter enabled the bearing design to be finalized. A 2-D, bulk-flow CFD analysis was performed to identify the stiffness, damping, load capacity, and power loss as a function of speed for the minimum and maximum bearing clearances. With the bearing design completed, the rotor diameter and length have now been established.

As reported in Phase I, the turbine is a radial inflow, 50 percent reaction type developed by Sixsmith at the National Bureau of Standards. Based on the compressor and bearing performance described above, the turbine design requirements were updated as listed in Table 6.

Power Required	800 – 1000 Watt (0.759 – 0.948 BTU/s)
Rotor Speed	1.1 Million RPM
Flowrate	1.14 gram/sec GH2 (0.0025 lbm/sec)
Inlet Pressure	3.5 atm (51.5 psia)
Inlet Temperature	300 K (540 R)
Expansion Ratio	3.2 Total-to-Static
Max. Tip Diameter	8 – 10 mm (0.315 – 0.394 in)
Min. Running Clearance	0.010 mm (0.0004 in)

Table 6: Turbine Design Requirements

A turbine sizing parametric study was conducted based on a total-to-static efficiency of 75 percent and optimum tip speed (U/C_0) of 0.66 (Note: the turbine size varies). A family of curves was generated based on turbine inlet temperature and is shown in Figure 2. The resulting efficiency as a function of turbine size is shown in Figure 3.

Based on this analysis, it was determined that the scaled NBS turbine will not provide the required performance. The linear scale factor to match tip speed produces a flow path with too much annulus area. This is primarily the result in the different operating fluid from the NBS turbine (GHe) to the recovery system turbine (GH₂). The resulting velocities are too low to produce the required high specific work. Table 7 compares the major parameters of the NBS baseline turbine to the recovery system turbine. Figure 4 shows the change in flow path required for the recovery system turbine. The major difference is replacing the inlet vane in the NBS turbine with a volute and extending the NBS turbine blades with an elliptical profile to improve efficiency. The recovery system turbine will then require either supplemental flow rate (as shown in the table) or a higher turbine inlet temperature. To retain the self-contained feature of the recovery system, the ambient heat exchanger will be coupled with the burn stack to provide a higher turbine inlet temperature for the prototype system.

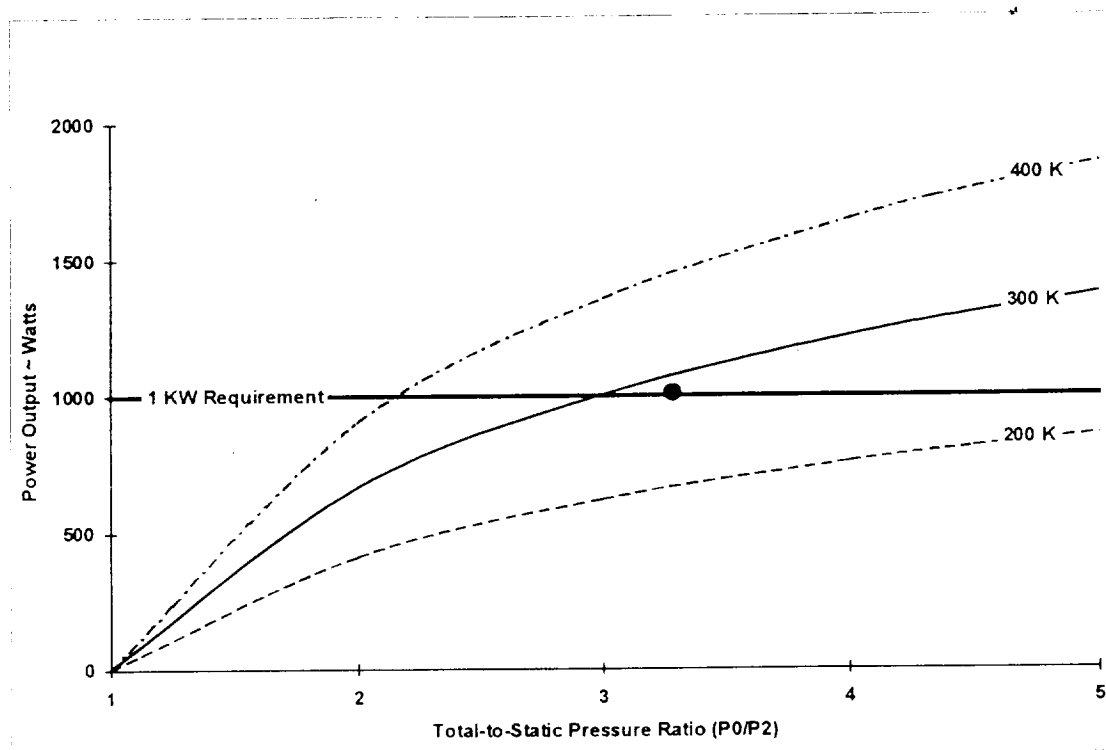


Figure 2: Turbine Sizing Parametric Study

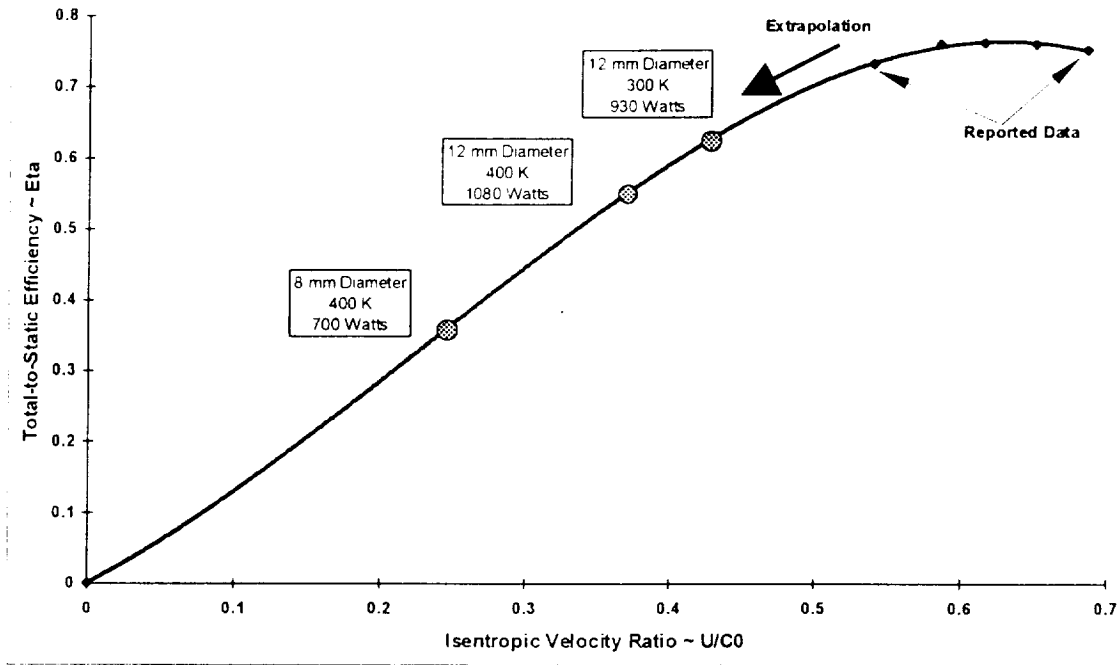


Figure 3: Turbine Efficiency

Parameter	NBS Baseline	Recovery System
<i>Fluid</i>	GHe	GH2
<i>Power</i>	0.569 BTU/sec	0.875 BTU/sec
<i>RPM</i>	600,000	1,100,000
<i>PT0/Ps2</i>	4.5	2.73
<i>U/C0</i>	0.67	0.20
<i>Total-to-Static Efficiency</i>	0.799	0.29
<i>PT-in</i>	81.44 psia	138 psia
<i>TT-in</i>	54 R	540 R
<i>Flowrate</i>	0.0224 lbm/sec	0.0067 lbm/sec
<i>ZR</i>	364.2 BTU/lbm-R	752.7 BTU/lbm-R
<i>Cp</i>	1.268 BTU/lbm-R	3.479 BTU/lbm-R
<i>Gamma</i>	1.698	1.385
<i>Tip Clearance</i>	0.0007 in	0.0007 in

Table 7: Comparison of NBS Baseline Turbine to Recovery System

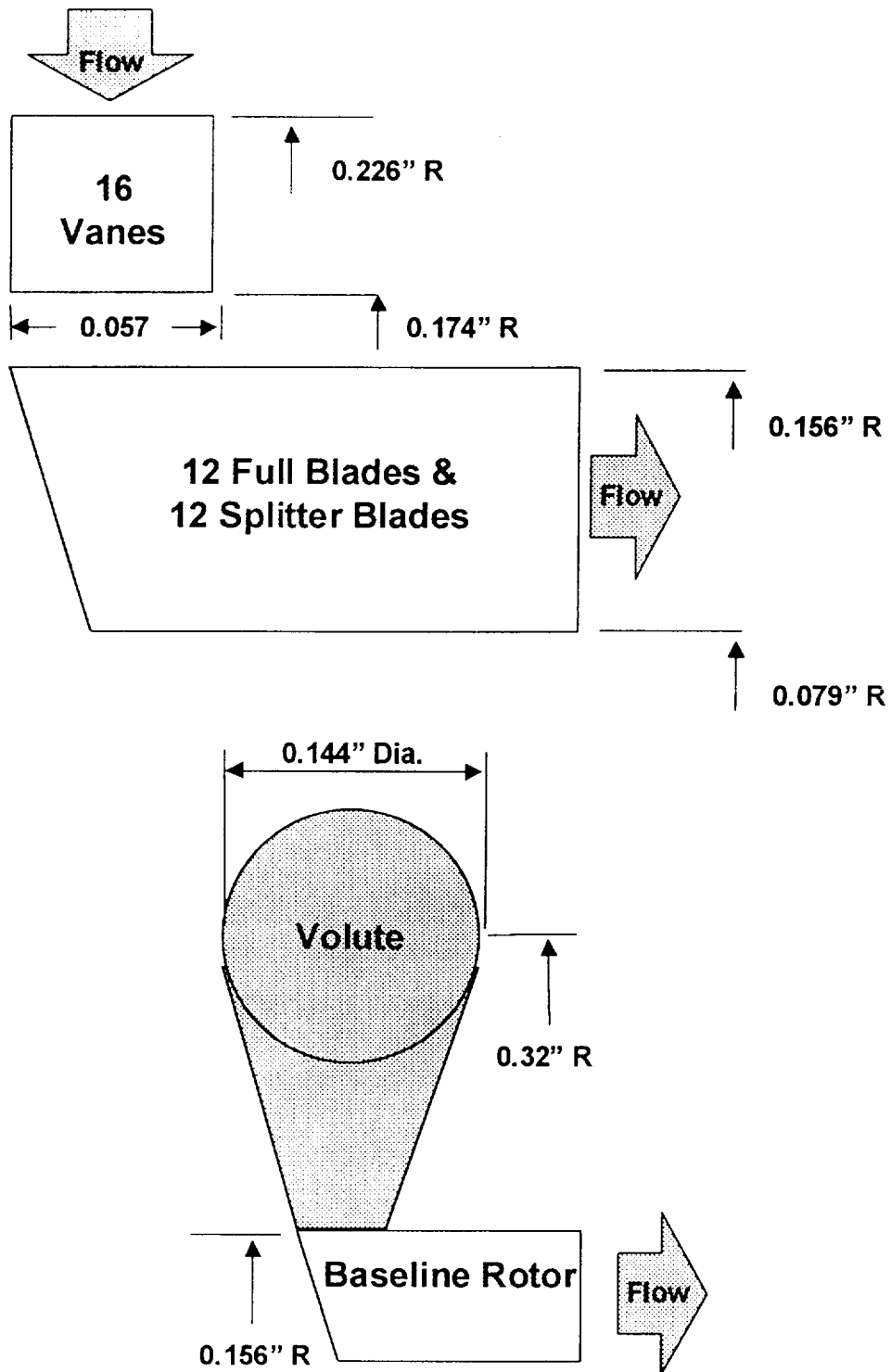


Figure 4: Comparison of NBS Baseline Turbine Flow Path (top) to Recovery System Flow Path (bottom)

With the compressor and turbine designs completed, the axial thrust loads were calculated to size the thrust disk. Figure 5 and Figure 6 show the pressure distribution across the compressor and turbine, respectively. The thrust load for the turbine is -11.9 N and the thrust load for the compressor is 36.76 N for a net thrust imbalance of 24.86 N towards the turbine. This is the maximum thrust load to be reacted by the thrust disk, thus completing the initial design of the rotor.

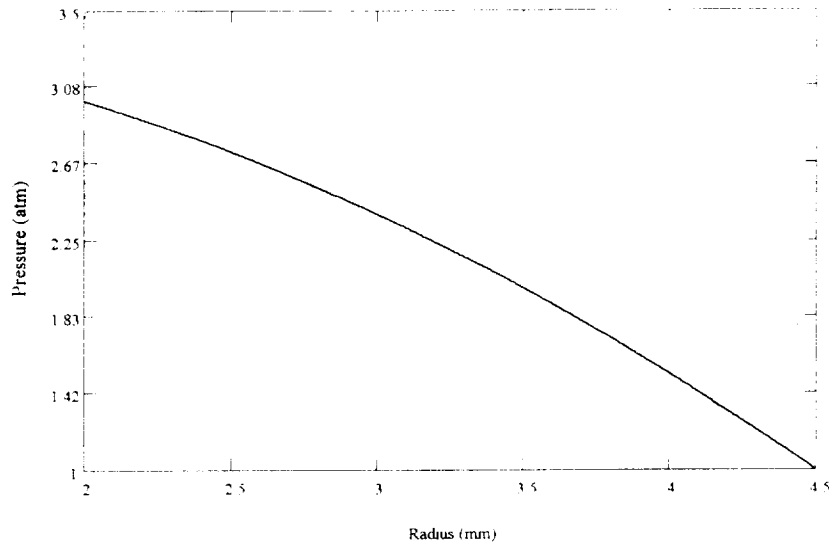


Figure 5: Radial Pressure Distribution Across Compressor

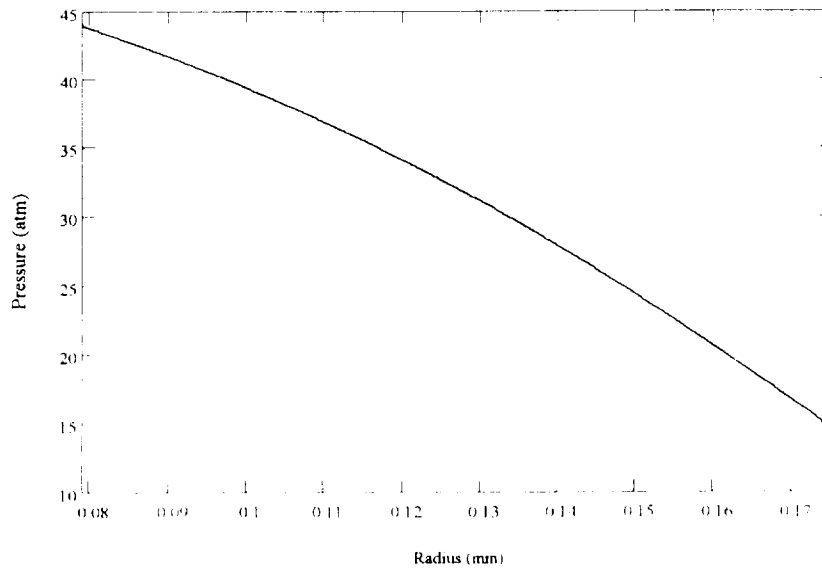


Figure 6: Radial Pressure Distribution Across Turbine

After the initial rotor drawing was completed and manufacturing had begun, the manufacturer asked for relief on the compressor geometry. Specifically, the compressor had a small (insignificant) amount of lean in the blade coordinate table and the table identified a tapered blade. The original geometry specified an inlet blade thickness of 0.0254 mm (0.001 inches) and a thickness of 0.1016 mm (0.004 inches) at the exit. To facilitate manufacturing, the geometry was modified for a uniform thickness blade of 0.1016 mm (0.004 inches). The impact of this increase in blade thickness is a decrease in compressor inlet flow area. To compensate, the number of blades was reduced from 25 to 24 and the inlet hub diameter was decreased from 1.524 mm to 1.5 mm. Since it was the intent of the compressor design to have no lean in the blade (to minimize bending stress) and to have a constant blade thickness, the drawing was revised to incorporate these changes with no impact to predicted performance. This configuration represents the second impeller design.

After numerous attempts to have this geometry manufactured, the supplier again asked for more relief. The electro-discharge machining (EDM) process could not be controlled sufficiently to yield uniform blades. It was felt that a larger diameter sinker (plunge) EDM tool, along with thicker blades, would yield an acceptable impeller. However, the larger tool and thicker blades also creates an interference with the adjacent blade near the inlet where the clearance is only 0.1016 mm. As a result, this interference would burn the adjacent blade off at the inlet.

To improve manufacturability, the impeller was re-designed with thicker blades (0.1778 mm) and the 24 blades were re-designed to be 12 full-length blades and 12 splitters. The use of splitters more than doubled the available tool path at the compressor inlet. Additionally, the use of splitters increased the flow path area allowing the hub diameter to be increased to the original size of 1.524 mm. These changes did not effect the compressor performance at design point; however, it did cause a loss in efficiency at some off-design points. This configuration represents the third compressor design.

Again, the supplier expressed concern with the manufacturability of the third compressor design. At this point, further re-design was not considered necessary as the geometry could be manufactured with either EDM or milling. The majority of the impeller could be machined with a 0.010 inch end-mill on a high-speed spindle (> 20K rpm). Additionally, the inlet could be milled with a 0.008 inch stub end-mill, provided the inlet blade height could be reduced. Therefore, the inlet hub diameter was increased from 1.524 mm to 1.778 mm and the blade thickness was reduced from 0.1778 mm to 0.175 mm to compensate for the reduced flow area on each of the 12 full-length blades and 12 splitters. This represents the fourth and final compressor design (and final rotor design), which is shown in Figure 7. The performance was determined to

be equivalent to the third geometry. The structural and thermal analysis of the rotor was completed in Phase I for operation at 1.3 million RPM (and over-speed capability to 1.45 million RPM), therefore, it was not updated for the lower operating speed of 1.1 million RPM.

A rotor dynamic sensitivity study was conducted by Critical Design Analysis, the consultant for this project. Bearing stiffness, bearing damping, shaft diameter, compressor overhung weight, turbine overhung weight, and thrust disk weight were all varied to study their effect on the rotor dynamic behavior. The consultant's report is included as Appendix B. Additionally, a detailed rotor dynamic analysis was conducted on the final rotor design. The rotor dynamic stability was predicted to be excellent with the first bending mode occurring well above the operating range at 1.5 million rpm and performance relatively insensitive to unbalance. The consultant's report is included as Appendix C.

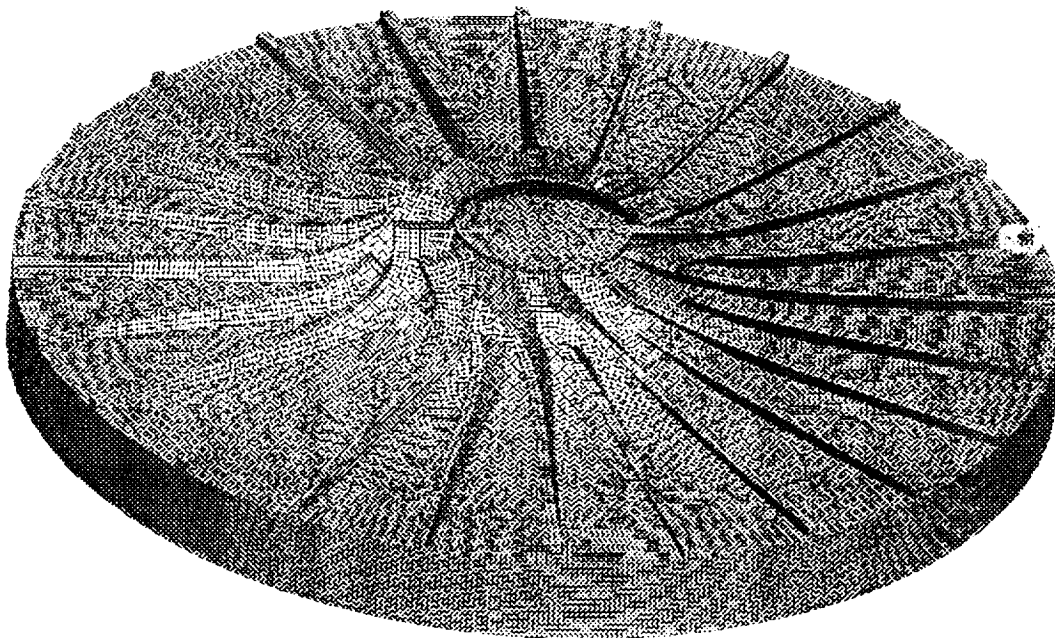


Figure 7: Final Compressor Geometry

Journal Bearings

The initial bearing size analysis was conducted in Phase I. However, this analysis was updated based on the latest geometry and operating conditions of the rotor. A two-dimensional, bulk-flow CFD analysis was performed to identify stiffness, damping, load capacity, and power loss as a function of speed throughout the minimum and maximum bearing operating clearance range. The resulting bearing geometry was identified on drawing AT98004. This type of

bearing was previously designed, analyzed, manufactured, and tested by AFAB Technologies. However, the previous bearings were made from Berylco 25 (a copper beryllium spring material) while the recovery system bearings are Titanium to minimize clearance changes due to thermal expansion.

The tolerances are relatively loose as the pads have adjustment capability. Dowel pins, springs, and set-screws are used to actuate the bearing pads radially inward. A 0.010 inch nominally thick web provides radial travel capability. A 0.032 inch nominally thick web provides radial stiffness while allowing pad rotation for self-stabilization. Three threaded holes are provided for jacking screws to facilitate dis-assembly. During startup and shutdown, when the rotor speed is insufficient to develop a hydrodynamic film stiffness necessary to react the rotor loads, there will be metal-to-metal contact between the bearings and rotor. Therefore, several coatings are identified to address this potential cyclic life issue. Under normal operating conditions, the rotor is supported entirely on a fluid-film.

AT98010 represents an alternate bearing geometry. The change in materials from Berylco 25 to Titanium has resulted in an increase in bearing metal stiffness. As a result, there is a concern that the hydrodynamic forces will be insufficient to take advantage of the self-stabilization design feature and may actually perform as a rigid pad bearing. To address this concern, an alternate bearing geometry was designed to move the actuation mechanism from the hinge point to the trailing edge of the bearing. This enables adjustment capability of the rigid pad bearing, if necessary. The remainder of the bearing design is identical.

Housing

The main housing has a single counter bore to hold the bearings and volutes, as the axial length of the deepest snap is approximately 1 ½ inches. The bore diameter is the most tightly controlled dimension as it centers all the parts. It has a 20 degree lead-in chamfer at the opening to allow parts to be installed with an arbor press.

There are three major ports in the main housing: compressor discharge, turbine inlet (2), and turbine discharge. The compressor discharge is a single port to match the scroll exiting from the parallel wall diffuser. The turbine supply has two ports located 180 degrees apart, which feed into the turbine volute supply annulus. Two ports are used to prevent the formation of a circumferential pressure gradient at the inlet of the volute. A large, single port is located on the centerline for the turbine exhaust. The through hole diameter of this port was increased beyond standard size to provide access to the turbine volute for disassembly.

Additionally, there are three secondary ports: journal bearing adjustment holes (6), instrumentation holes (2), and a thrust bearing supply line. Three holes are located at each journal bearing to provide access to the pad actuation screws. Two instrumentation holes are included (-02 version only) for a proximity probe and pressure and temperature sensors. Due to the thin wall necessary to provide thermal isolation between the turbine and compressor, there is insufficient wall thickness to allow a threaded boss for the thrust bearing supply. Therefore, an 0.080 deep spot face was added to permit welding of a ¼" diameter titanium tube.

Cover

The cover, AT98006, is two parts mated into an inseparable assembly. It includes the compressor inlet port, parallel wall diffuser, volute, and compressor shroud. The inlet port is extended axially so that a length in excess of 4 diameters ($L > 4d$) is available upstream of the compressor. The parallel wall diffuser clearance is set when the volute is mated to the cover. The volute has a square cross-section instead of the round cross-section used in the analysis. The square cross-section allows it to be machined with an end-mill and has the same hydraulic radius as the round cross-section for no impact on performance. The compressor shroud profile matches the compressor blade profile. A shim installed outboard of the seal groove between the cover and housing sets the compressor clearance.

Turbine Volute

The turbine nozzle ring, AT98007, is also two parts mated into an inseparable assembly. Again, the circular cross-sections have been replaced with square for ease of manufacture. The inner and outer diameters of the of the volute are tightly controlled to provide the proper turbine clearance and housing interference fit, respectively.

Thrust Bearing

Initially, a spiral groove thrust bearing (SGTB) was sized to react the net axial rotor load discussed in the rotor design section. The spiral groove thrust bearing design was optimized based on CFD trade studies conducted by Broman (1991) resulting in the bearing geometry summarized in Table 8. Its performance is summarized in Figure 8 and Figure 9.

Number of Grooves	16
Ratio of Inner Radius to Outer Radius	0.8
Groove Angle	11
Ratio of Groove Depth to Operating Clearance	3.2
Inner Radius	4.7 mm
Groove Depth	0.635 mm

Table 8: Spiral Groove Thrust Bearing Geometry

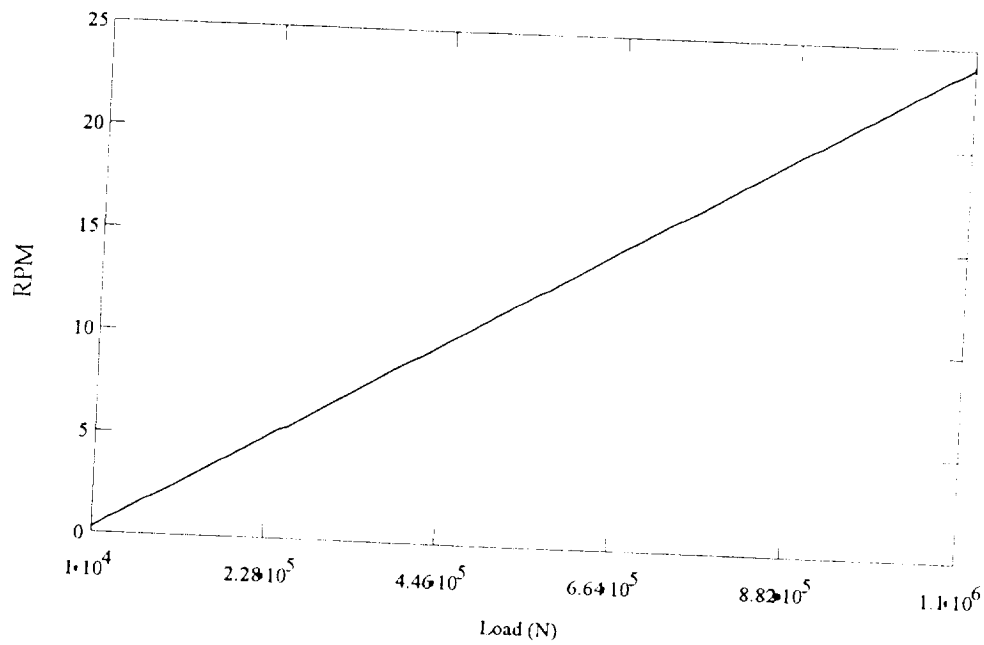


Figure 8: Load Capacity of SGTB at Nominal Operating Clearance of 0.28 mm

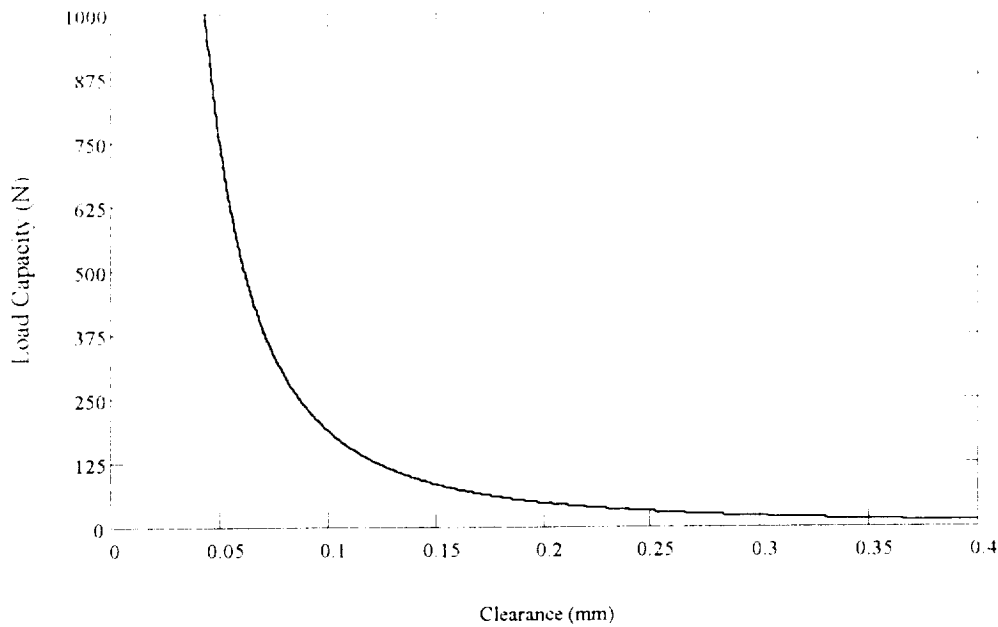


Figure 9: Load Capacity vs. Operating Clearance at 1.1 million RPM

However, the size of this bearing is near structural limits. Therefore, the SGTB concept was replaced with a hydrostatic thrust bearing. The hydrostatic thrust bearing takes advantage of the high-pressure discharge flow from the compressor enabling a smaller area to react the same load. This corresponds to a smaller thrust disk on the rotor for lower stresses as well as elimination of the spiral groove pattern for reduced manufacturing costs. The hydrostatic thrust bearing was sized using a 2-D bulk-flow code. Because of the shallow pockets required to avoid pneumatic hammer instability, a single annulus was used in place of individual pockets. The final thrust bearing geometry is summarized in Table 9.

Number of Orifice Supplies	8
Orifice Size	0.00825 inches
Inner Diameter	0.352 inches
Inner Annulus Diameter	0.400 inches
Diameter of Orifice Location	0.45 inches
Outer Annulus Diameter	0.50 inches
Annulus Depth	0.00021 inches

Table 9: Hydrostatic Thrust Bearing Geometry

The thrust bearing (AT98008) reflects this geometry with additional design features. The bearing is supplied by an annulus, which receives flow from the single ¼ inch tube welded to the outside of the housing. The annulus distributes

the flow into the eight 0.079 inch feeder lines which intersect the 8 orifice lines. There is no break-edge at the inner diameter of the thrust bearing to maximize performance. The 3/4 inch threads in the support allow dis-assembly of the thrust bearing. An instrumented configuration (-02) has a 0.188 diameter radial through hole for instrumentation access.

Separator

Every effort was made to find an off-the-shelf gas/liquid separator. However, an extensive search did not locate a suitable separator with the performance and operating range necessary for the recovery system. The residence time to condense the droplets was not sufficient. Therefore, a custom designed separator was pursued. Several concepts were evaluated. Measuring performance of a gas/liquid separator is difficult without sophisticated instrumentation (densitometer, which are notoriously inaccurate) to measure the quality (fluid loading of the gas phase) of the upstream and downstream flow. Therefore, qualitative testing was pursued to further evaluate the leading concept. A full-scale Plexiglas separator model was built and tested (see Figure 10).

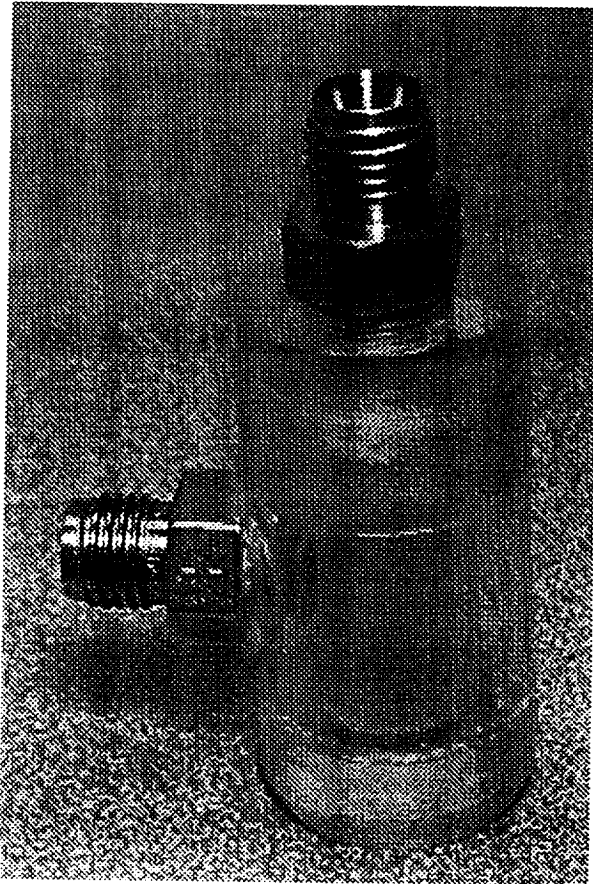


Figure 10: Plexiglas Model Separator

The Plexiglas separator allowed the fluid generation of the separator to be visually tested, and provided invaluable design validation data. The flow is accelerated circumferentially as it enters along the outer wall and is accelerated as it enters the inner wall. As the velocity increases, the local pressure and temperature decrease and the heavier liquid is forced outward where it condenses against the inner wall and collects via gravity feed to the bottom. The separator operation is shown schematically in Figure 11.

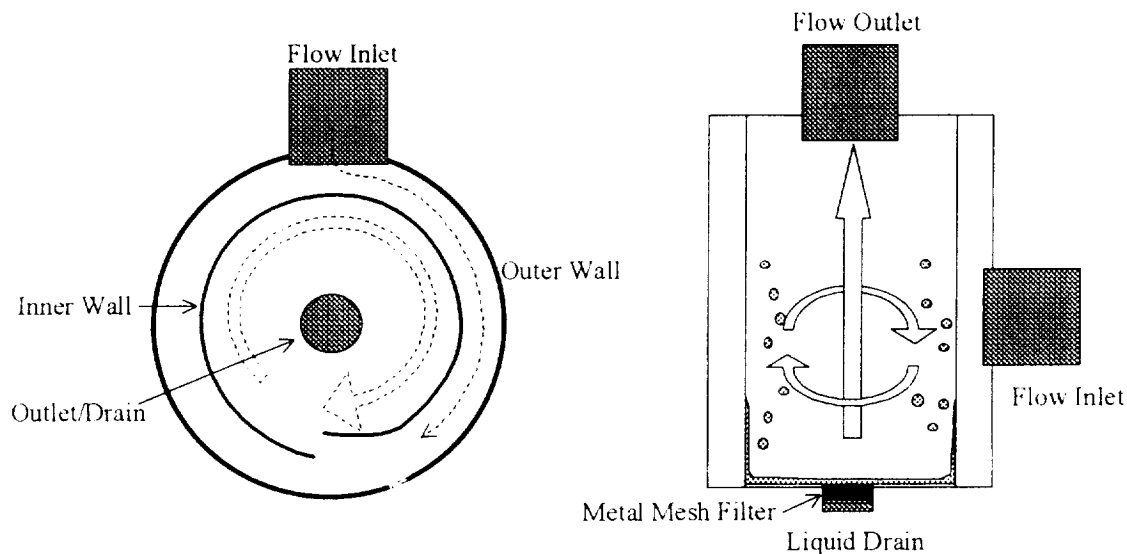


Figure 11: Separator Operation

The results of the Plexiglas model facilitated the design of the stainless-steel separator identified on AT98009. The final separator is an all metal (passivated stainless steel), welded assembly. Like the hydrostatic thrust bearing supply line on the housing, $\frac{1}{4}$ " tubing ports are welded in place for easy installation with compression fittings.

Heat Exchanger

The hydrogen-hydrogen heat exchanger was sized for parallel, counter flow resulting in a minimum of 791 W transfer. All stainless steel, tube-in-tube, counter-flow hydrogen-hydrogen heat exchangers (part number 413) were purchased from Exergy, Inc., a specialist in miniature heat exchangers. The inner tube is $\frac{1}{4}$ " with 0.035 inch thick walls and the outer tube is $\frac{1}{2}$ " with 0.035 inch thick walls. The inner tube is rated for 4,500 psia operation and the outer tube is rated for 2,000 psia service. The pressure drop in water for the inner tube is 50 psid at 1 gpm. The pressure drop in water for the outer tube is 25 psid at 3 gpm. The supplied fittings are pipe thread (NPT); therefore, adapters

sealed with Teflon tape are used to convert the ports for mating with ¼" tube nuts. The heat exchanger includes two 5/16"-18 mounting holes and bolts.

J-T Valve

Several orifice configurations were evaluated for use a Joule-Thompson Valve including Bendix bleed orifices, sharp-edged orifices, and converging-diverging nozzles. Cv expansion restrictors from Farmington Engineering were selected for use as the J-T valve. They are part number CRMS00630xxA, where the xx represents the calibrated orifice size in mils (thousandths of an inch). These are calibrated, single piece orifices. The design point hydraulic diameter for the J-T valve is 0.030 inches. Therefore, six orifice sizes were procured and tested, which ranged from 0.025 inches to 0.035 inches. The orifice is installed in a standard ¼" tube fitting (union) by drilling a 0.156 inch counter bore in one side of the union 0.170 inches deep.

Tubing

The recovery system components are connected with stainless steel seamless tubing. AISI 316 stainless steel ¼" tubing with 0.035 inch thick walls is used throughout. All tubing is field routed and cut to fit. All connections are made with industry standard compression fittings.

Fittings

A variety of industry standard (either Parker or SwageLok) adapters, unions, tees, crosses, and fittings are used to connect the various components.

Frame

The recovery system is mounted within a metal frame formed by 1 ½ inch slotted angle and secured with ¼ - 28 bolts, lock washers, and nuts. The rectangle formed by the outer perimeter of the angle is filled with insulation. The turbine supply and exhaust ports situated to protrude outside of the insulated area.

Final Analysis

A flow model was created to conduct the steady-state and transient performance analysis and is shown below in Figure 12. The results from the steady-state, design-point analysis are summarized in Table 10.

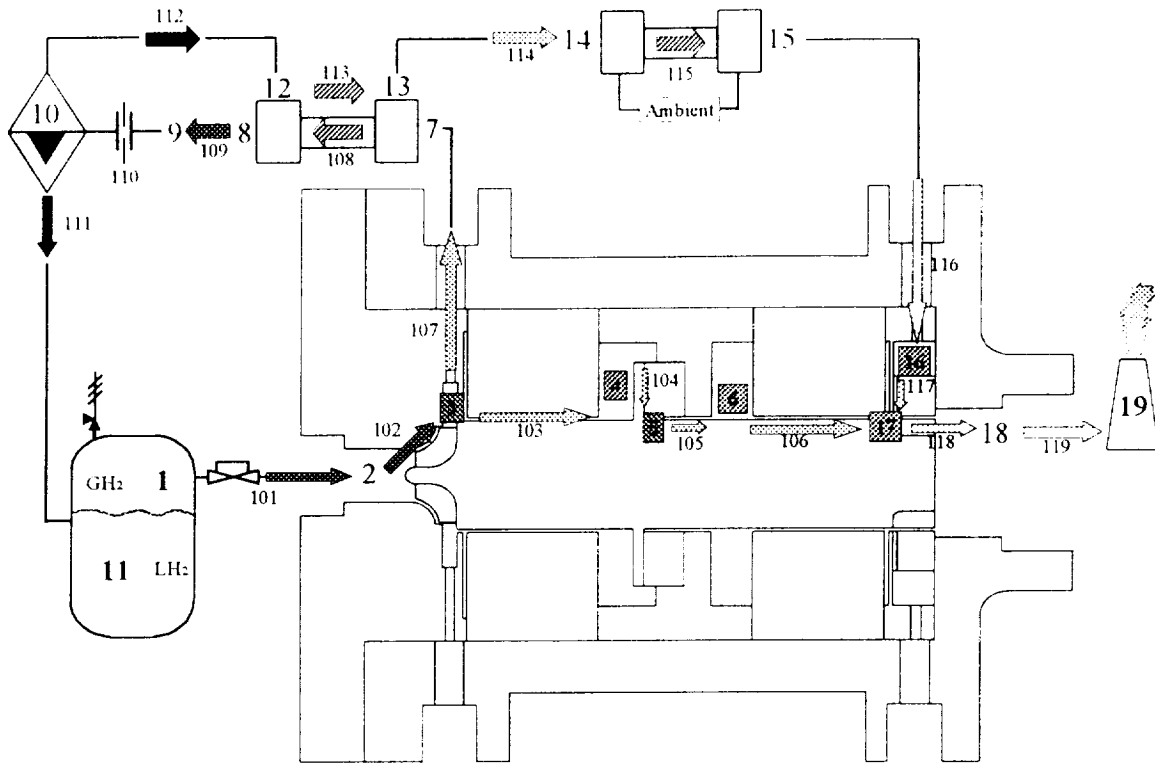


Figure 12: Liquid Hydrogen Boil-Off Recovery System Flow Model

BOUNDARY NODES

NODE	P(PSI)	T(F)	RHO	AREAN(IN ²)
3	214	-357.4	0.425	0
11	58.8	-413	3.9337	0
19	15	-100	0.0078	0

SOLUTION

INTERNAL NODES

NODE	P(PSI)	PT(PSI)	T(F)	Z	RHO	QUALITY
4	213.9944	213.9976	-357.3994	0.9256	0.425	0
5	213.9842	213.9874	-357.3999	0.9256	0.425	0
6	213.9724	213.9755	-358.4516	0.9228	0.4307	0
7	213.4991	213.7808	-357.4206	0.9258	0.4241	0
8	212.4321	212.7145	-398.3398	0.3812	1.7091	0
9	211.7316	211.9171	-398.469	0.3697	1.7605	0
10	59.0023	86.4716	-412.7254	0.5452	0.4338	0.687
12	54.5441	55.7241	-413.4317	0.5544	0.4004	0.6905
13	46.8711	48.1499	-334.4433	0.9926	0.0709	0
14	34.2414	36.346	-336.5278	0.9943	0.0526	0
15	17.2116	20.0495	-26.9939	1.0015	0.0075	0
16	16.7329	16.8127	-27.024	1.0015	0.0073	0
17	16.2406	23.6461	-69.4122	1.0015	0.0078	0
18	15.6321	15.7335	-69.4634	1.0015	0.0075	0

BRANCH	K (LBF-SEC^2/ (LBM-FT)^2)	DP (PSI)	FLOWRATE (LBM/SEC)	VELOCITY (FT/SEC)	Re	M
107	4.60E+06	0.501	0.004	78.4	2.06E+05	3.59E-02
103	4.70E+06	5.59E-03	0.0004	8.28	2.18E+04	3.79E-03
104	3.20E+06	1.02E-02	0.0004	8.28	2.18E+04	3.79E-03
105	4.70E+06	1.19E-02	0.0004	8.28	2.18E+04	3.79E-03
106	1.50E+11	198	0.0004	397	1.53E+05	0.182
108	4.60E+06	1.07	0.004	78.6	2.06E+05	3.59E-02
109	3.00E+06	0.701	0.004	31.7	2.38E+05	5.50E-03
110	9.00E+08	153	0.004	380	8.19E+05	6.24E-02
111	6.30E+06	0.202	0.0012	37.9	6.34E+04	2.26E-02
112	4.10E+07	4.46	0.0027	159	1.92E+05	9.45E-02
113	1.00E+08	7.67	0.0027	172	1.90E+05	0.105
114	1.60E+08	12.6	0.0027	524	1.64E+05	0.234
115	2.20E+08	17	0.0027	707	1.67E+05	0.319
116	6.20E+06	0.479	0.0027	315	1.78E+04	8.25E-02
117	6.40E+06	0.492	0.0027	324	1.78E+04	8.49E-02
118	6.00E+06	0.609	0.0031	347	2.20E+04	9.61E-02
119	6.20E+06	0.632	0.0031	361	2.20E+04	9.99E-02

Table 10: Steady-State, Design-Point Results from Flow Model

A sensitivity analysis was performed for the cycle. The sensitive variable in the cycle is the temperature entering the JT valve. This temperature directly controls the amount of liquid produced by the system. Figure 13 shows the results of the temperature sensitivity study. Please note that the y-axis scale is percent of goal, which is 35 percent. Therefore, 50 percent of goal represents 50 percent of 35 percent, or 17.5 percent total liquid yield. As you can see from the figure, one degree (from 34 to 35 K), represents a drop in liquid production from 100 percent of goal to 38 percent. Another increase of one degree (from 35 to 36 K) further reduces liquid production from 38 percent of goal to 10 percent.

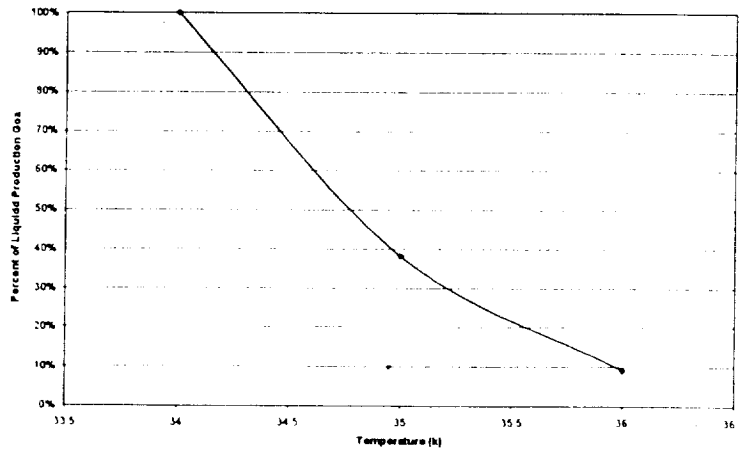


Figure 13: Sensitivity of Liquid Production to JT Valve Inlet Temperature

The graph underscores that the heat exchanger effectiveness will ultimately control the amount of liquid produced by the system. Therefore, the cycle was re-evaluated to determine how the desired J-T inlet temperature can be achieved more reliably, thus mitigating the temperature sensitivity risk and making the overall system more robust.

Several alternate configurations were considered. The most robust system utilizes a second heat exchanger cooled with bypass boil-off. The inclusion of a second heat exchanger increases the robustness of the recovery system by diverting gaseous hydrogen flow at 4.0 atmospheres and 26 Kelvin directly from the boil-off and into the heat exchanger cooling tube, thus bypassing the compressor inlet. This diverted, or bypass, flow is then expanded isenthalpically through an orifice to approximately 1.1 atmospheres and 22 Kelvin. The bypass flow then enters the heat exchanger to aid in cooling the gaseous hydrogen exiting the compressor. This configuration is shown schematically in Figure 14 and the revised flow model is shown in Figure 15.

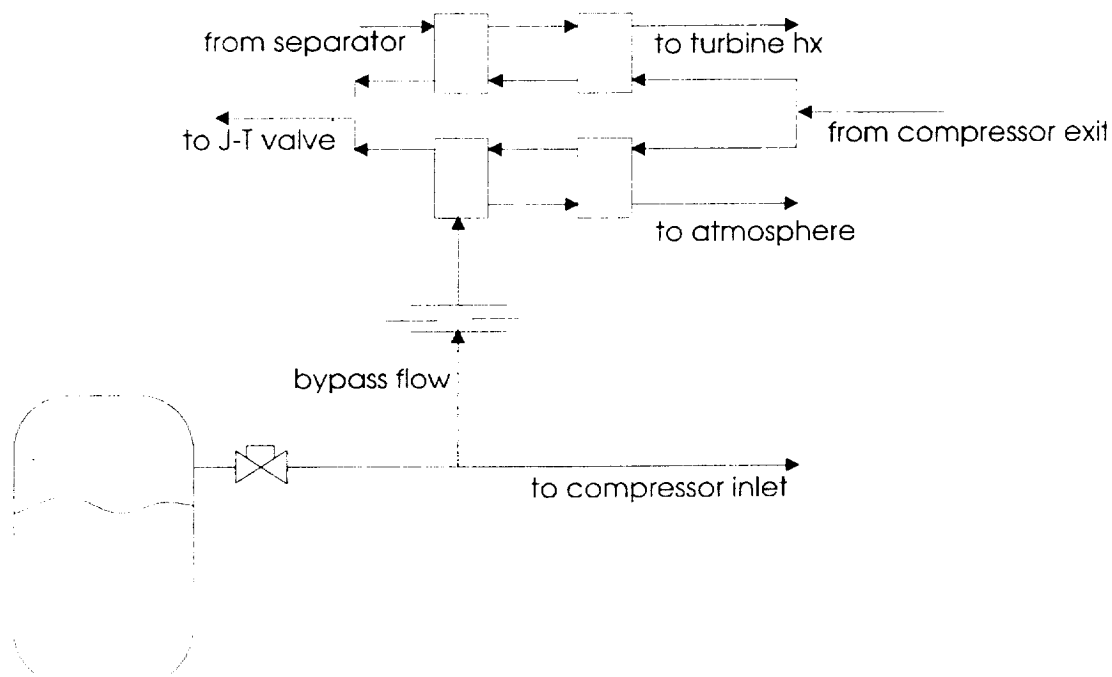


Figure 14: Schematic of Bypass Flow Configuration

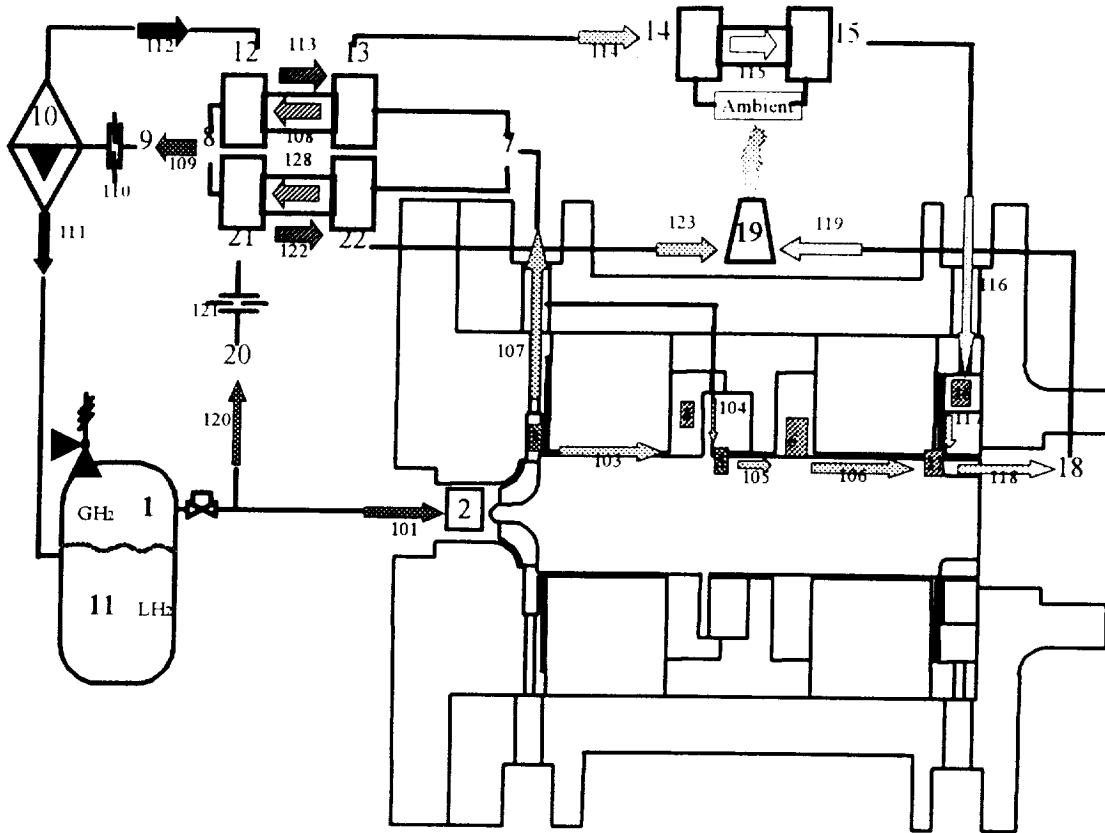


Figure 15: Flow Model of Bypass Flow Configuration

An off-design analysis was conducted. The pertinent parameters for off-design compressor performance are: polytropic efficiency, mass flow, exit temperature, and exit pressure. These parameters were evaluated and are presented in Figures 16 through 19.

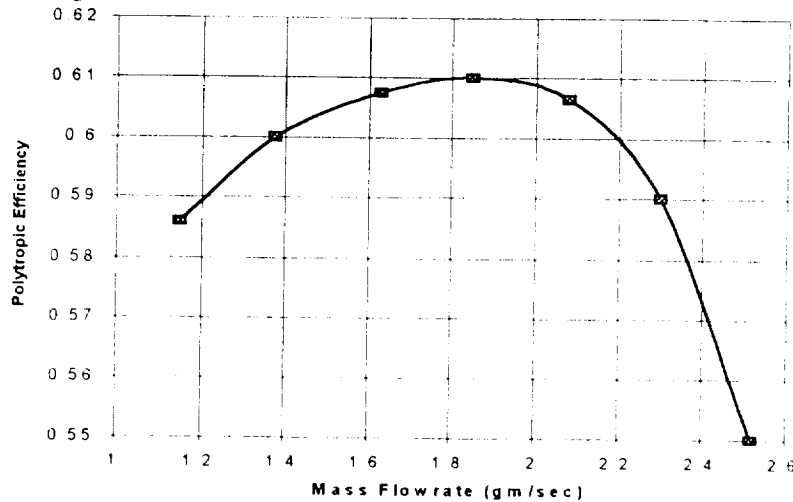


Figure 16: Stage Performance of Baseline Hydrogen Compressor

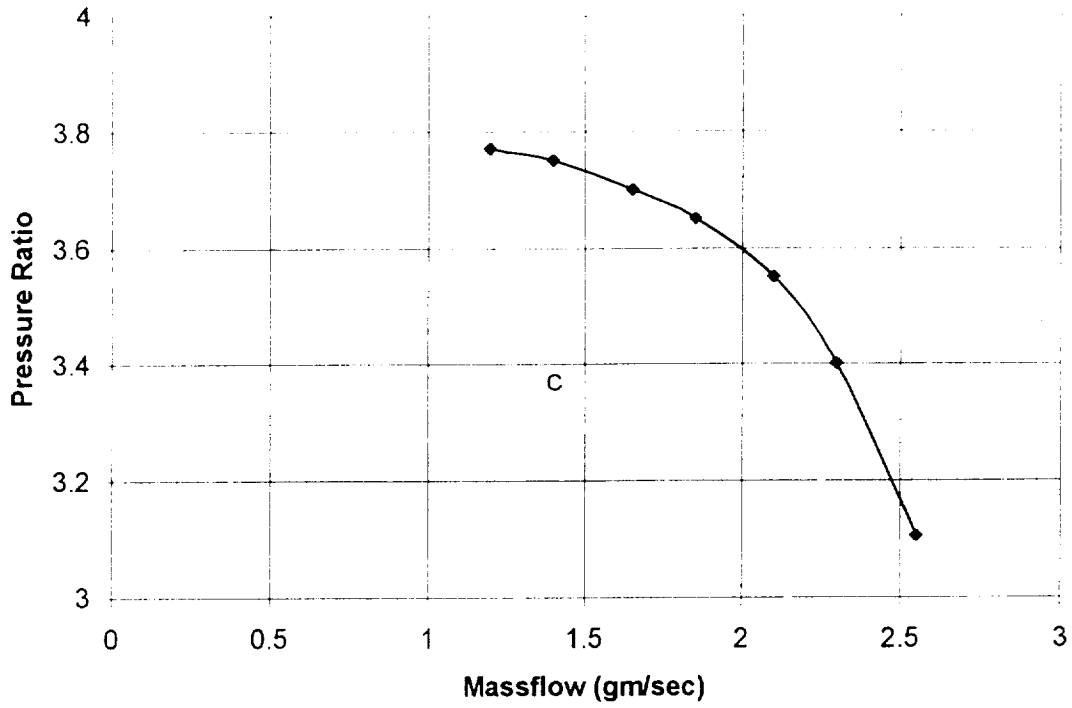


Figure 17: Flow Rate vs. Pressure Ratio of Baseline Compressor

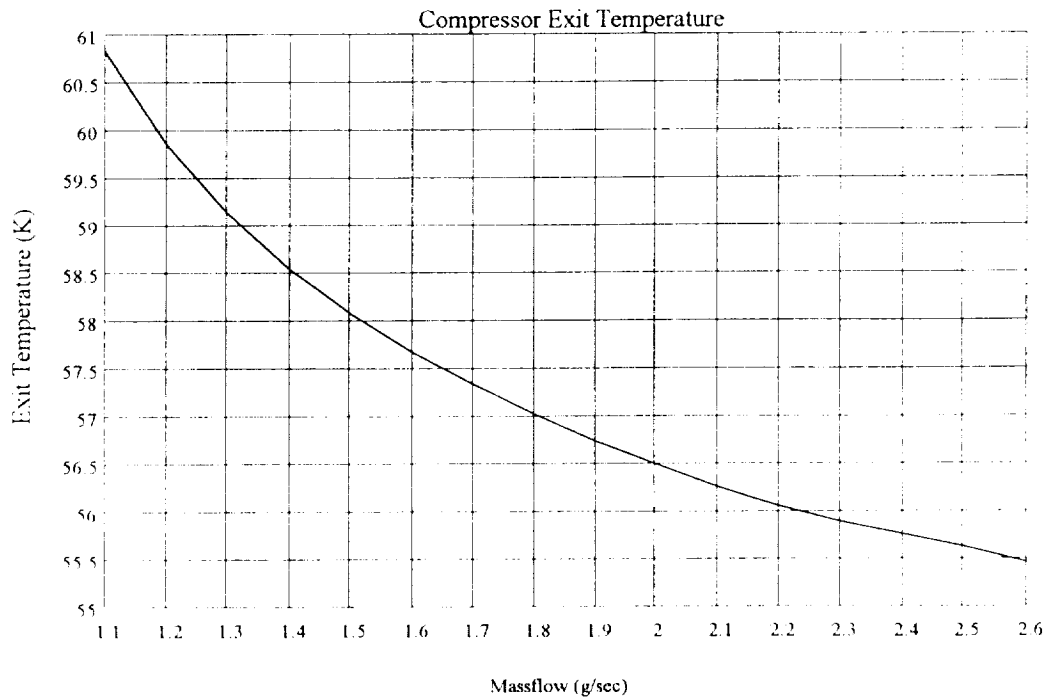


Figure 18: Compressor Exit Temperature as a Function of Mass Flow

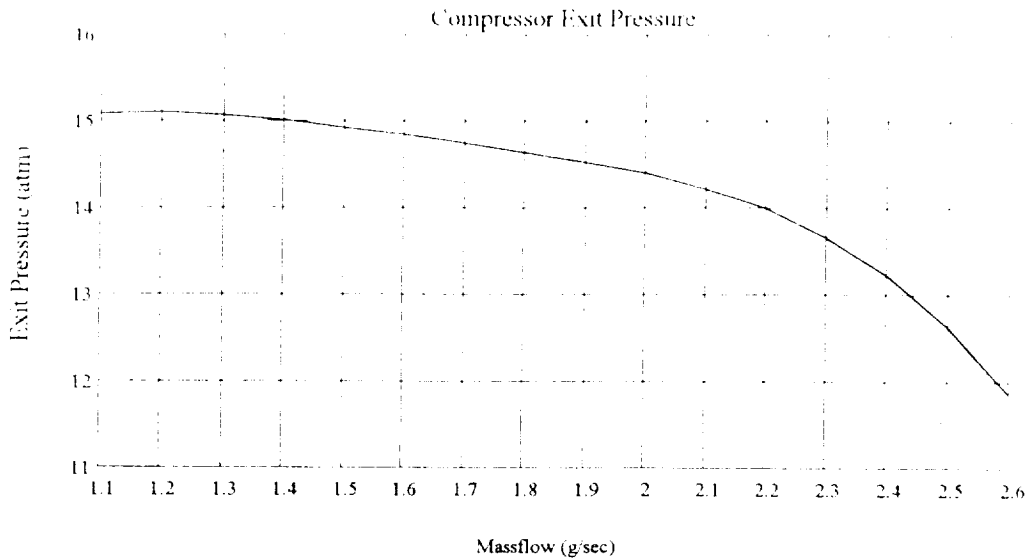


Figure 19: *Compressor Exit Pressure as a Function of Mass Flow*

The flow model was run for several transient and quasi steady-state points to simulate start-up, shut-down, and over-speed conditions. The critical period for the turbocompressor is during startup. A successful start involves accelerating the shaft as quickly as possible to a speed at which the thrust bearing and tilting –pad bearings capacities exceed the operating loads. The impulsive startup force will be provided by the pressure ratio across the turbine. As the temperature feeding the turbine rises, at a fixed pressure ratio, the output power will increase and shaft will turn faster. As speed increases, the power requirements of the compressor, bearings, and windage increase with speed squared. As a result, the system is self-regulating for operating speed.

Hardware Procurement

Upon initial completion of the drawings, drawing packages were sent to three precision machine shops for quotes. A purchase order was placed with Dynamic Engineering, Inc., as they were the low bidder. With the exception of the compressor blade geometry, very few manufacturing issues were identified. The few issues that were identified involved drawing interpretation or clarification and the addition of missing dimensions.

With the exception of the rotor, most hardware was delivered on schedule or within a few months of the promised delivery date, although some hardware was delivered incomplete or not at all in accordance with the revised purchase order. The numerous re-designs of the compressor to facilitate manufacture delayed hardware availability by over a year. The design cycle for each of the four compressor designs took approximately three months including design, analysis, drawing changes, and machining attempts.

After the forth and final compressor design, DEI was still unable to machine the rotor or find a subcontractor willing to machine it. Despite the inability of a precision machine shop with an excellent reputation to produce the part, AFAB took receipt of the hardware "as-is" and began investigating alternate suppliers.

The final rotor design was then sent to ten precision machine shops. Two shops with extensive turbomachinery experience quoted the job, NREC and Turbocam. NREC, partnered with Mikino, was selected as the most capable supplier for this part size (and they were also the lower bidder). NREC completed the rotors within a couple months of schedule, but still beyond the originally scheduled completion date for the 24-month contract. Therefore, a 4-month no-cost contract extension was requested and approved. The only manufacturing issue with the rotor was the recessed radius on each side of the thrust-bearing disk was replaced with a conventional radius.

The Phase II proposal estimated that low volume production costs of the turbocompressor would be around \$10,000 with a total liquid hydrogen boil-off recovery system unit cost of around \$40,000. The prototype turbocompressors were delivered at approximately \$12,000 each with low volume production costs estimated at just less than \$10,000. However, the prototype systems were delivered at approximately \$20,000 each (hardware and assembly). The final production configuration system is now estimated at less than \$30,000 each (fully assembled and tested), approximately 25 percent less than initially estimated.

Component Tests

Component testing includes both sub-components and components. The sub-components are the bearings and the Joule-Thompson valve. The components are comprised of the turbocompressor, heat exchanger, and separator. A data acquisition system consisting of 12 thermocouples, 4 pressure transducers and a high frequency, AC coupled proximity probe was assembled. The system runs on a Pentium II 350 running Windows and LabVIEW software. Temperature measurements are resolved to 0.1 degree F and pressure measurements to 0.05 psi. The AC coupled high frequency data is recorded at 400 KHz. A summary of the data acquisition is provided in Table 11 below. All instrumentation is fully calibrated and traceable to the National Institute for Standards and Testing (NIST).

Manufacturer	Description
Omega	Type "E" (Chromal Constantine) Thermocouples
Kaman	KD 2300-0.5SU Proximity Probe System
Validyne	DP-10 Welded SS Transducer
Validyne	P2 Transducer
Validyne	CD280 Carrier Demodulator (2 Channel)
National Instruments	PCI-MIO-16EX I/O Board
National Instruments	PCI-MIO-16E1 I/O Board
National Instruments	LabVIEW Software

Table 11: Data Acquisition System

Stiffness tests were conducted on the bearings as a function of web thickness. The web thickness was measured on the minimum and maximum thickness bearings and several thickness' distributed throughout this range. Load and deflection measurements were made to calculate the sprint constant as a function of web thickness.

Five orifice sizes, which will be used as the Joule-Thompson valve, were flow tested at design point and off-design in air, helium, and hydrogen. Pressure and temperature sensors were placed upstream and downstream of the orifice along with a flow meter. The data was used to calculate the flow parameter and JT factor of the orifice.

Several turbocompressor builds were assembled and tested. Rotating tests of the turbocompressors were attempted in air and helium. Compressor inlet flow rate, pressure, and temperature were measured along with discharge pressure and temperature. Turbine inlet pressure and temperature, along with flow rate, were also measured. The data was to be used to calculate the compressor and turbine efficiencies.

Heat exchanger flow tests were conducted at design point and off-design in air, helium, and hydrogen. Inlet and discharge pressure and temperature, as well as flow rate, were measured for each of the parallel, counter-flow streams. The data was used to calculate the heat exchanger efficiency at design and off-design conditions.

Finally, qualitative tests were conducted on a Plexiglas model separator and flow tests were conducted on a stainless steel separator in air, helium, and hydrogen. The separator was tested at design and off-design conditions.

System Tests

Based on the results of the component testing, the optimum recovery system components were assembled into a liquid hydrogen boil-off recovery system and tests were conducted in air, helium and hydrogen (less turbocompressor). Tests were conducted at design point and off-design operating conditions.

Prototype Tests

The final configuration resulting from the system tests was assembled into a prototype recovery system without instrumentation. This system was tested in helium prior to delivery to Stennis Space Center.

Results Obtained

Provided below are the results obtained for the work performed identified in the previous section.

Detail Design

To validate the integrity of the compressor design, a 3-D heat transfer analysis was conducted. The results of this analysis are presented in Figure 20. The change in performance from the baseline compressor to the final compressor (with splitters) is shown in Figures 21 and 22.

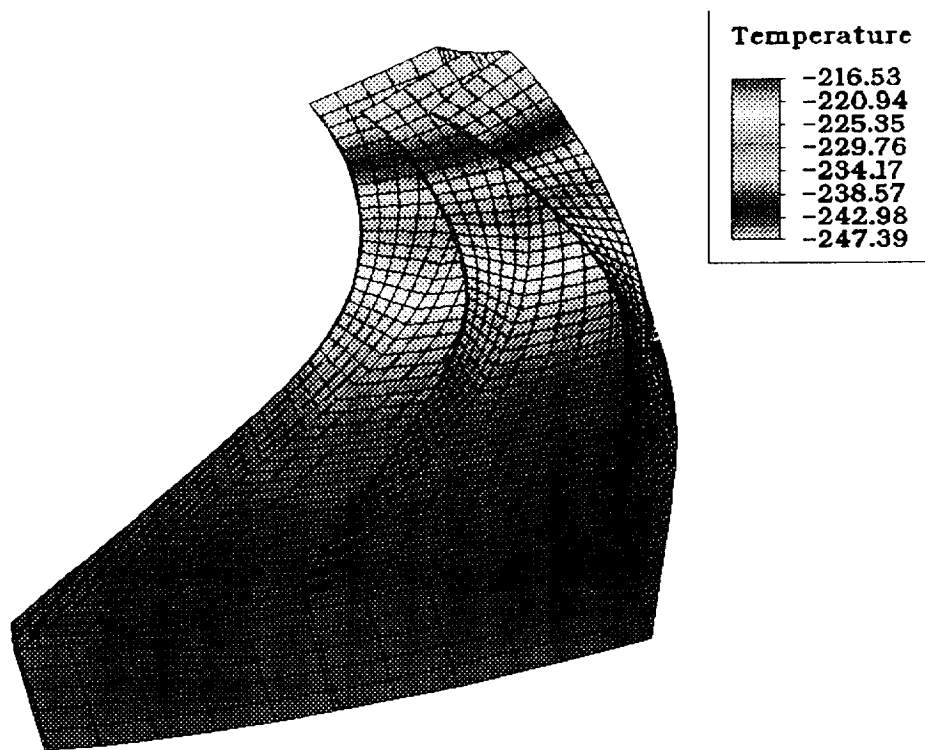


Figure 20: Thermal Contour Plot (degrees F) of Compressor Blade

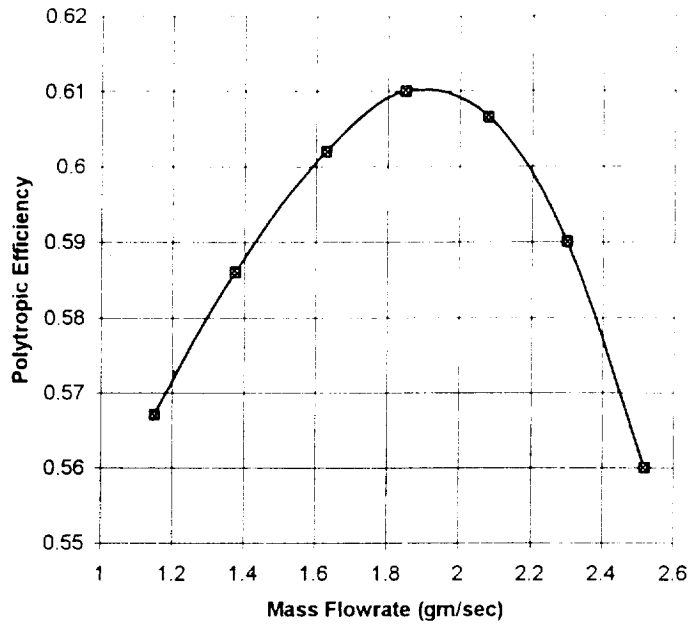


Figure 21: Stage Performance of Hydrogen Compressor

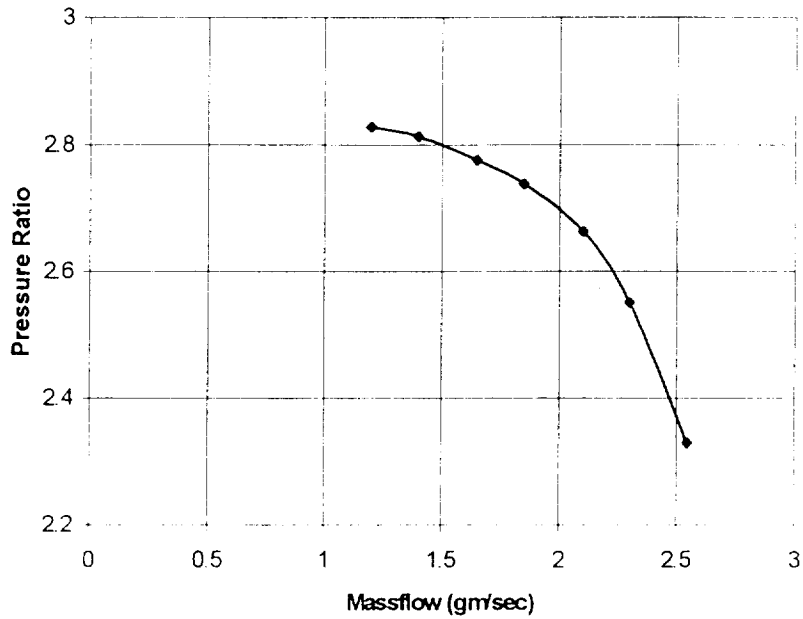


Figure 22: Flow Rate vs. Pressure Performance

The final turbine design resulted in the following recommendations for the production turbine:

- Vane Ring
 - Provide highly-swirled discharge flow at near sonic speed
 - Exhibit low trailing edge (TE) thickness (<10 percent TE blockage)
 - Have smooth surface finish
- Radial-Inflow Turbine Wheel
 - Radial star zero-cambered "inducer" blades
 - Axial-turbine-like cambered exducer to provide increased reaction
 - Low trailing edge thickness (<10 percent TE blockage)
 - Have smooth surface finish
 - Tail cone to minimize dump loss and maximize efficiency
- Exhaust Diffuser
 - Produce low rotor discharge pressure for maximum expansion ratio
 - Maximum practical length and an equivalent cone angle of $2\text{-}\theta$ (6 degrees)

These results are presented graphically in Figure 23. Note that the star and exducer can be manufactured as separate pieces and later mechanically connected or bonded together. The operating conditions and performance for the production turbine are shown in Table 12.

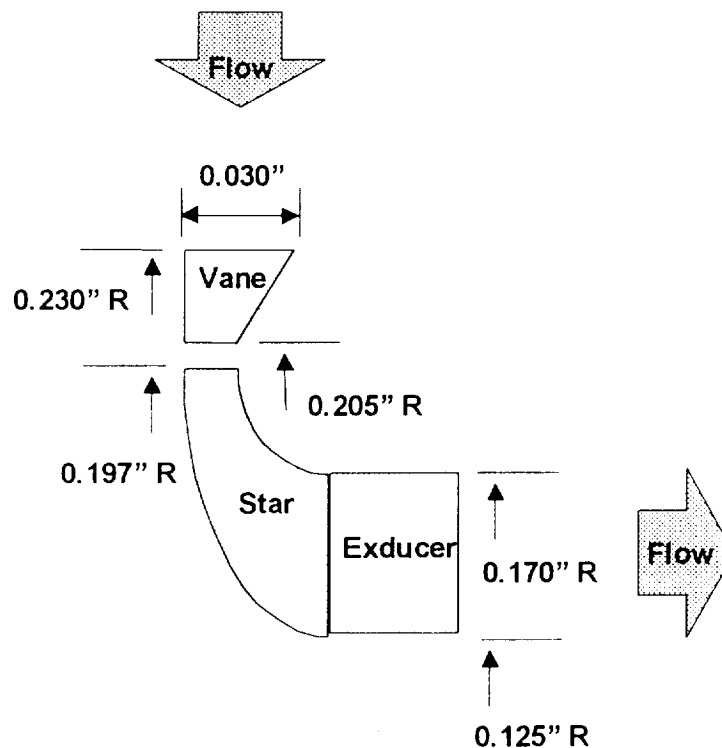


Figure 23: Production Turbine Geometry

Fluid	GH2
Power	0.759 BTU/sec (800 W)
RPM	1,100,000
PT0/Ps2	2.90
U/C0	0.48
Total-to-Static Efficiency	0.63
PT-in	51.45 psia (3.50 atm)
TT-in	540 R (300 K)
Flow Rate	0.0025 lbm/sec (0.38 cmm)
ZR	752.7 BTU/lbm-R
Cp	3.479 BTU/lbm-R
Gamma	1.385
Tip Clearance	0.0004 inches

Table 12: Production Turbine Performance and Operating Conditions

Performance of the journal bearings was re-calculated based on the final design and operating conditions. The resulting performance is shown in Figure 24 through Figure 28.

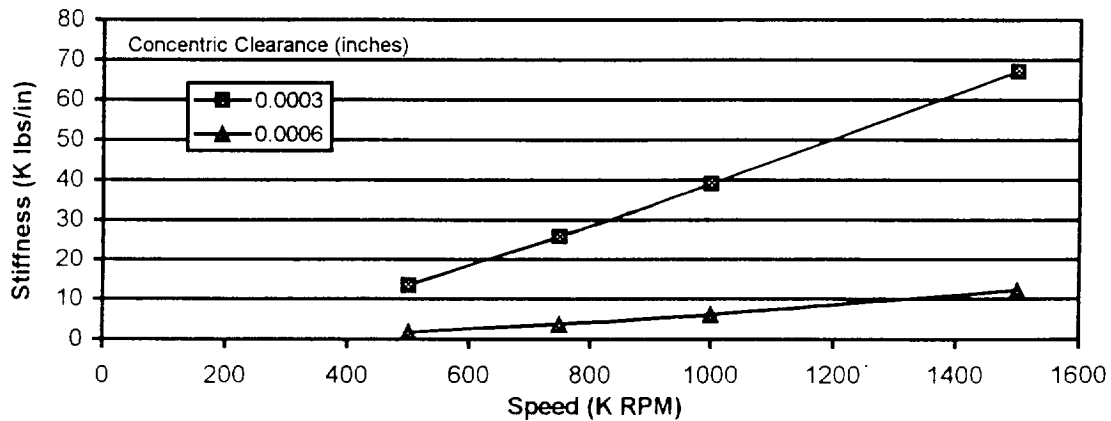


Figure 24: Journal Bearing Stiffness vs. Speed and Clearance

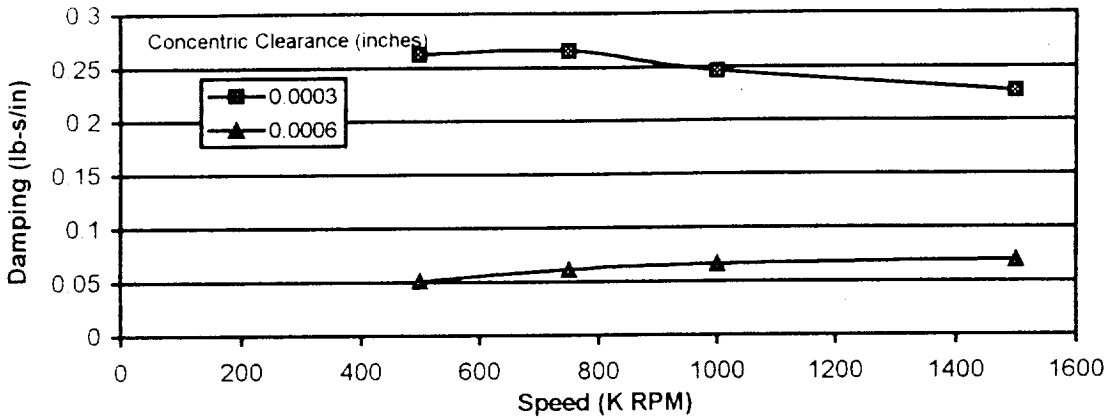


Figure 25: Journal Bearing Damping vs. Speed and Clearance

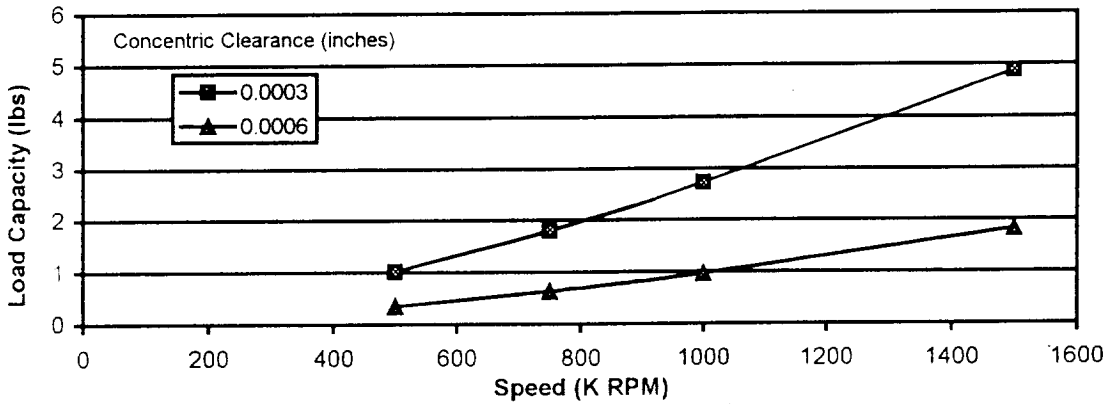


Figure 26: Journal Bearing Load Capacity vs. Speed and Clearance

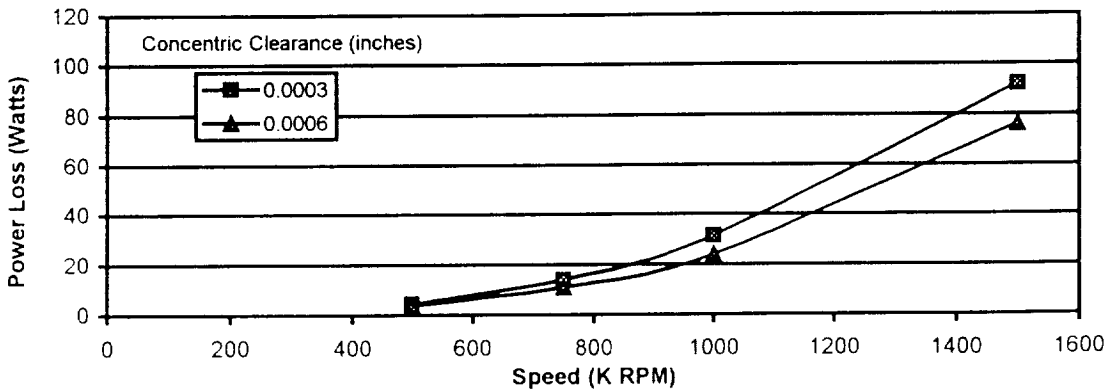


Figure 27: Power Loss vs. Speed and Clearance (Compressor-End Bearing)

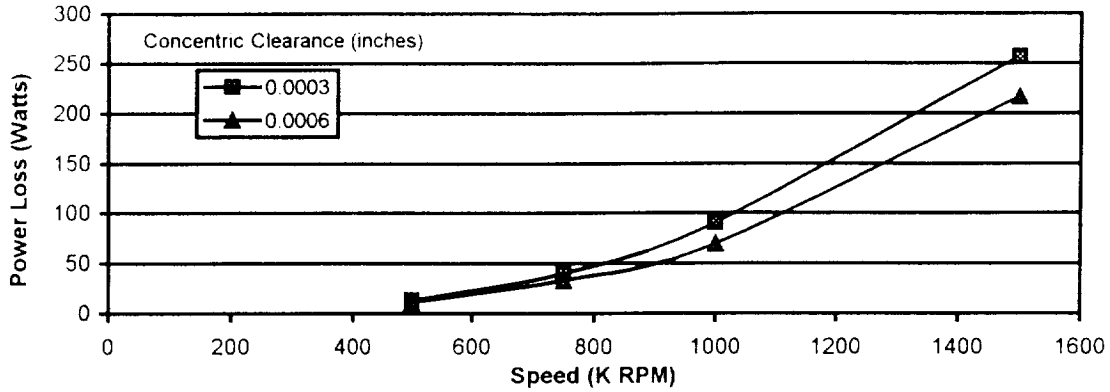


Figure 28: Power Loss vs. Speed and Clearance (Turbine-End Journal Bearing)

Final Analysis

As a result of sensitivity cycle analysis performed, the final cycle includes the use of a bypass heat exchanger to increase the robustness of the system. As the bypass flow increases, the flow through the compressor decreases. Therefore, the compressor efficiency and pressure ratio change according to Figure 29 and Figure 30.

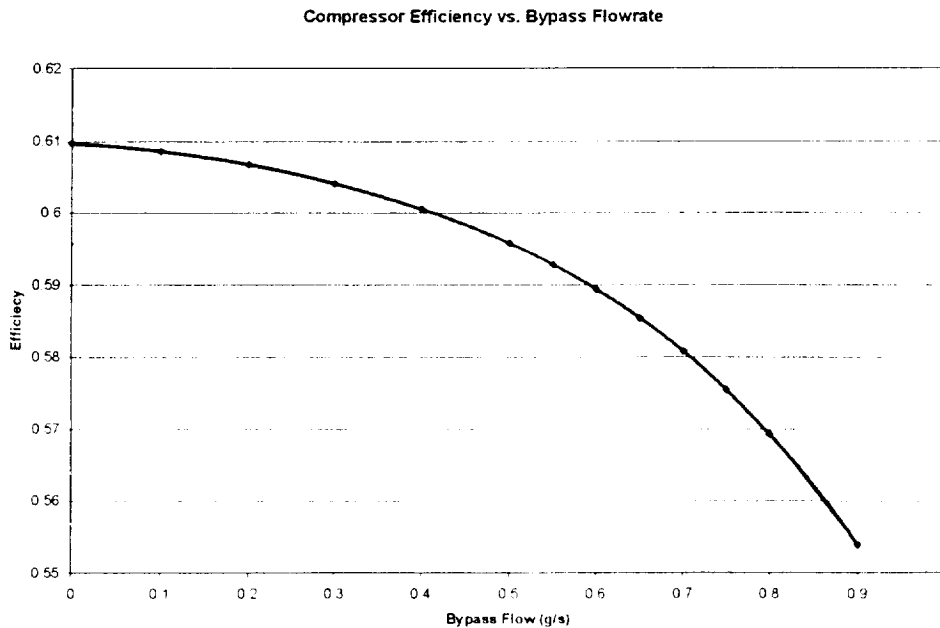


Figure 29: Compressor Efficiency vs. Bypass Flow

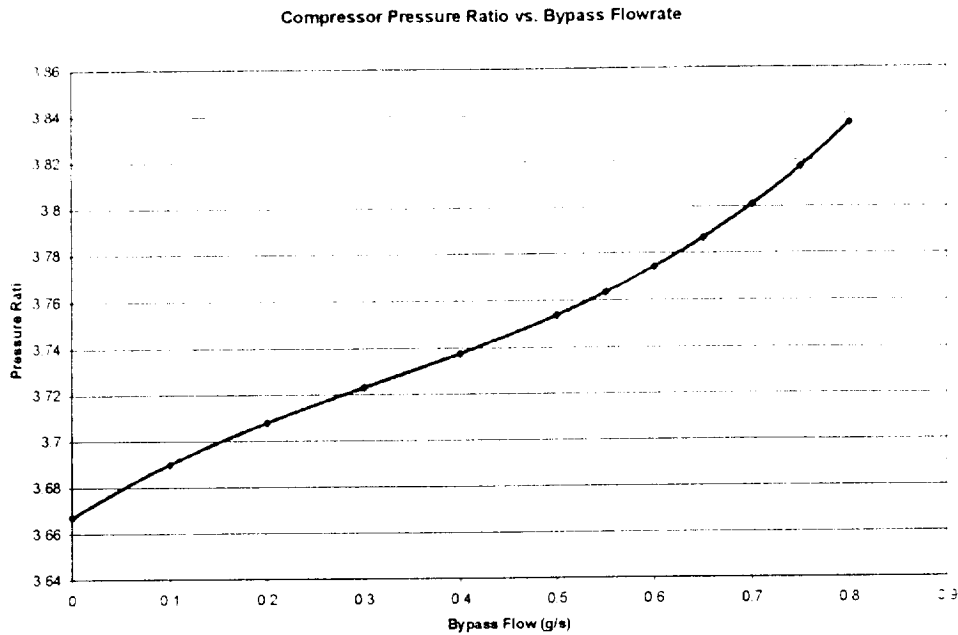


Figure 30: Compressor Pressure Ratio vs. Bypass Flow

As the efficiency of the compressor decreases, the compressor exit temperature increases by the relation:

$$T_{\text{exit}} = T_{\text{inlet}} \times \text{PR}^{(\gamma-1)/(\gamma \text{ec})}$$

where:

T_{exit} is the compressor exit temperature,
 T_{inlet} is the compressor inlet temperature,
 PR is the compressor pressure ratio,
 γ is the ratio of specific heats, and
 ec is the compressor efficiency.

The percent yield of the recovery system is equal to the mass flow of the liquid recovered divided by the mass flow of gaseous hydrogen leaving the tank.

$$Y = (m_{\text{compressor}} - m_{\text{separator gas}}) / m_{\text{tank}} = (1 - (h_{\text{JT}} - h_f) / (h_g - h_f)) \times (m_{\text{compressor}} / m_{\text{tank}})$$

where:

Y is the percent liquid yield,
 $m_{\text{compressor}}$ is the mass flow through the compressor,
 $m_{\text{separator gas}}$ is the mass flow of gas leaving the separator,
 m_{tank} is the mass flow leaving the tank,
 h_{JT} is the enthalpy of the gas entering the JT valve,
 h_f is the enthalpy of liquid hydrogen at 4 atmospheres, and
 h_g is the enthalpy of gaseous hydrogen at 4 atmospheres.

The enthalpy of the gaseous hydrogen entering the Joule-Thompson valve depends upon the enthalpy change possible through the heat exchanger and is governed by the relation:

$$h_{JT} = \frac{m_{\text{bypass}} (h_{b2} - h_{b1}) - m_{\text{compressor}} h_{\text{comp}} - m_{\text{compressor}} \left(\frac{h_f}{h_g} - h_f \right) (h_{s1} - h_{s2})}{m_{\text{compressor}} \left(\frac{h_{s1} - h_{s2}}{h_g - h_f} - 1 \right)}$$

where:

- m_{bypass} is the mass flow diverted from the compressor inlet,
- h_{b1} is the enthalpy of the bypass flow as it enters the heat exchanger,
- h_{b2} is the enthalpy of the bypass flow as it exits the heat exchanger,
- h_{s1} is the enthalpy of the gas leaving the separator as it enters the heat exchanger, and
- h_{s2} is the enthalpy of the gas leaving the separator as it exits the heat exchanger.

The enthalpies of the cooling gas streams exiting the heat exchanger depend upon the effectiveness of the heat exchanger and the maximum heat transfer possible through the heat exchanger. The maximum heat transfer possible for each stream of the heat exchanger would occur if the temperature of the cooling stream could be raised to the temperature of the hot stream entering the heat exchanger. Therefore, the enthalpies of the cooling gas streams exiting the heat exchanger are given by:

$$h_{b2} = (1-E) \times h_{b1} + E \times h_{b2\text{max}}$$

and

$$h_{s2} = (1-E) \times h_{s1} + E \times h_{s2\text{max}}$$

where:

- E is the overall heat exchanger effectiveness,
- $h_{b2\text{max}}$ is the enthalpy of the bypass cooling flow exiting the heat exchanger raised to the temperature of the gas leaving the compressor, and
- $h_{s2\text{max}}$ is the enthalpy of the separator cooling flow exiting the heat exchanger raised to the temperature of the gas leaving the compressor.

Figure 31 plots the relationship between the amount of mass flow diverted from the compressor to the overall liquid yield of the system.

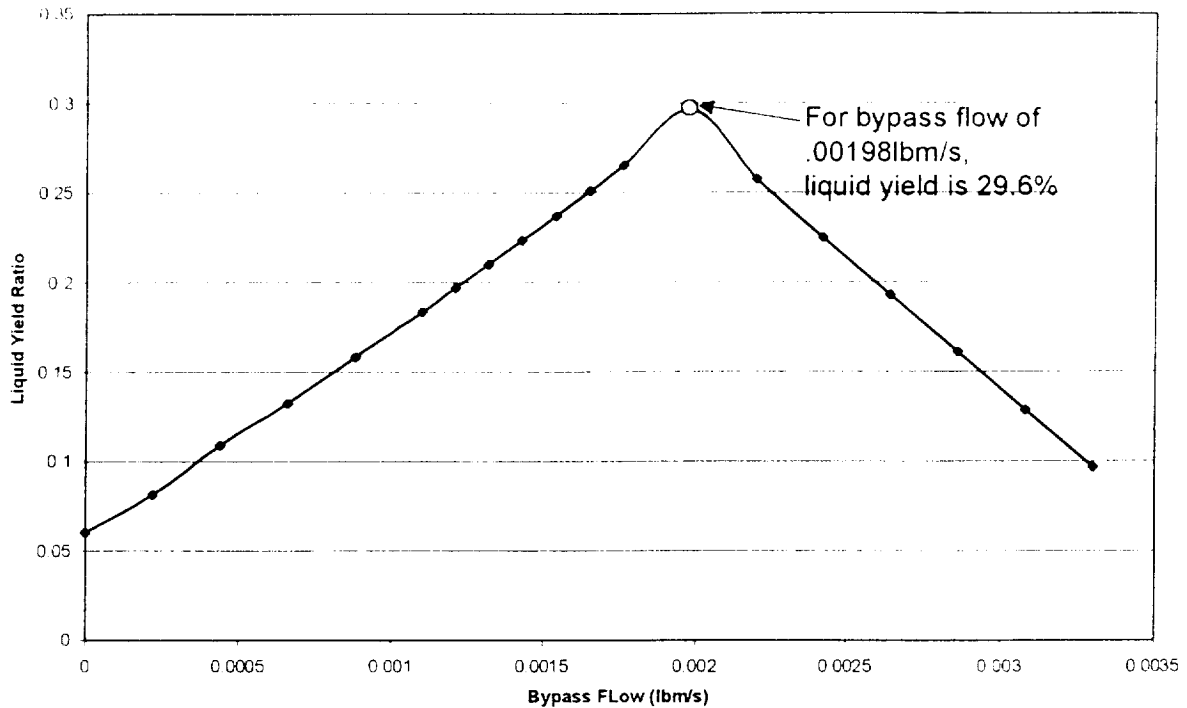


Figure 31: *Liquid Yield vs. Bypass Flow*

As shown in Figure 31, the ratio of liquid yield mass flow to boil-off mass flow increases with bypass heat exchanger flow rate until the gas approaches vapor saturation temperature at the heat exchanger exit. Beyond this point (0.00198 lbm/sec), liquid yield decreases.

In order to calculate the lengths and diameters of the heat exchanger tubing, each heat exchanger was divided into five sections. This sectioning was necessary because of the significant change in C_p of the hydrogen as it is heated or cooled at such low temperatures (Figure 32 and Figure 33).

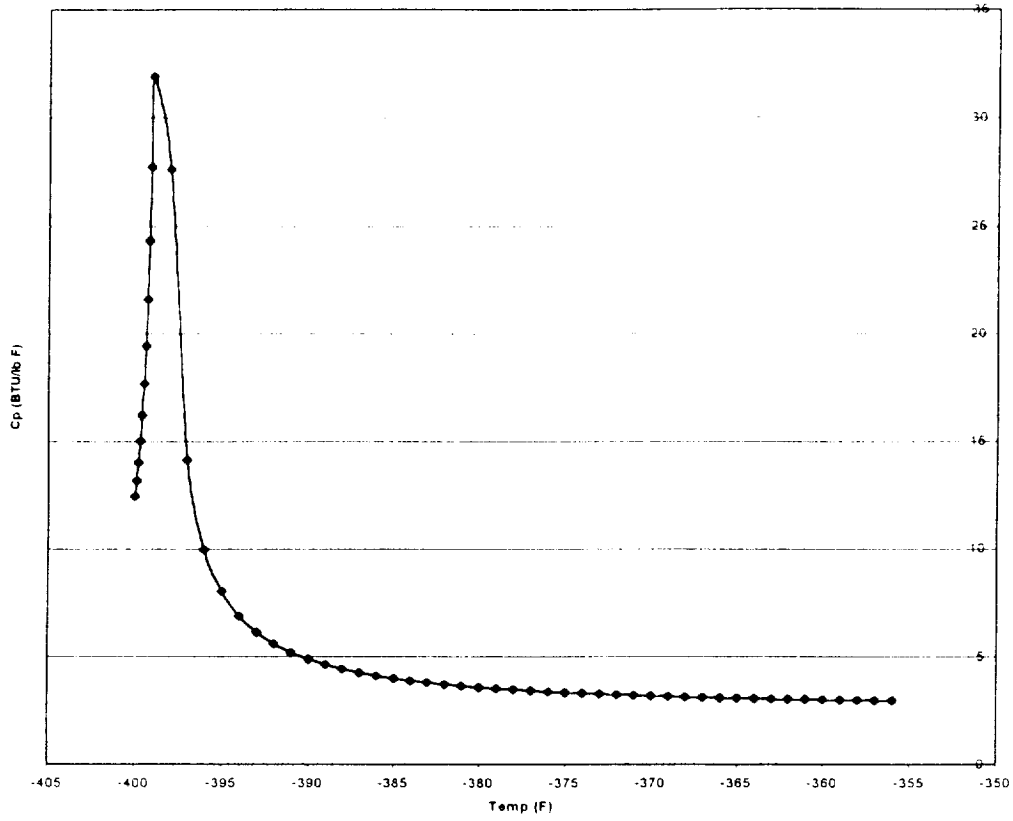


Figure 32: Cp vs. Temperature for H₂ at 14.7 psi

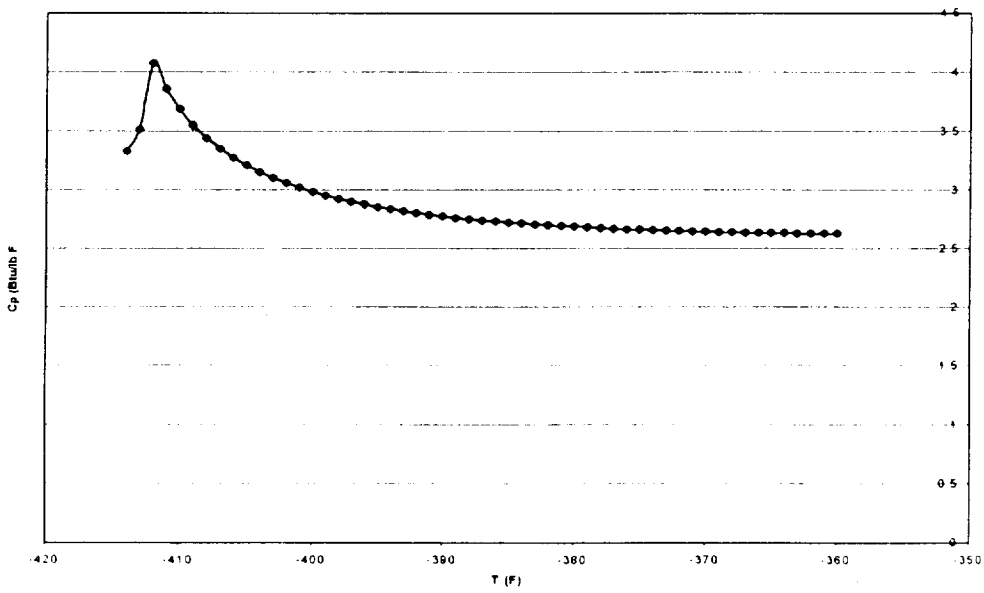


Figure 33: Cp vs. Temperature for H₂ at 4.1 atmospheres

The results for the length of the heat exchangers using 1/8" inner tubing for the high pressure flow and 3/16" outer tubing for the low pressure flow are plotted in Figure 34.

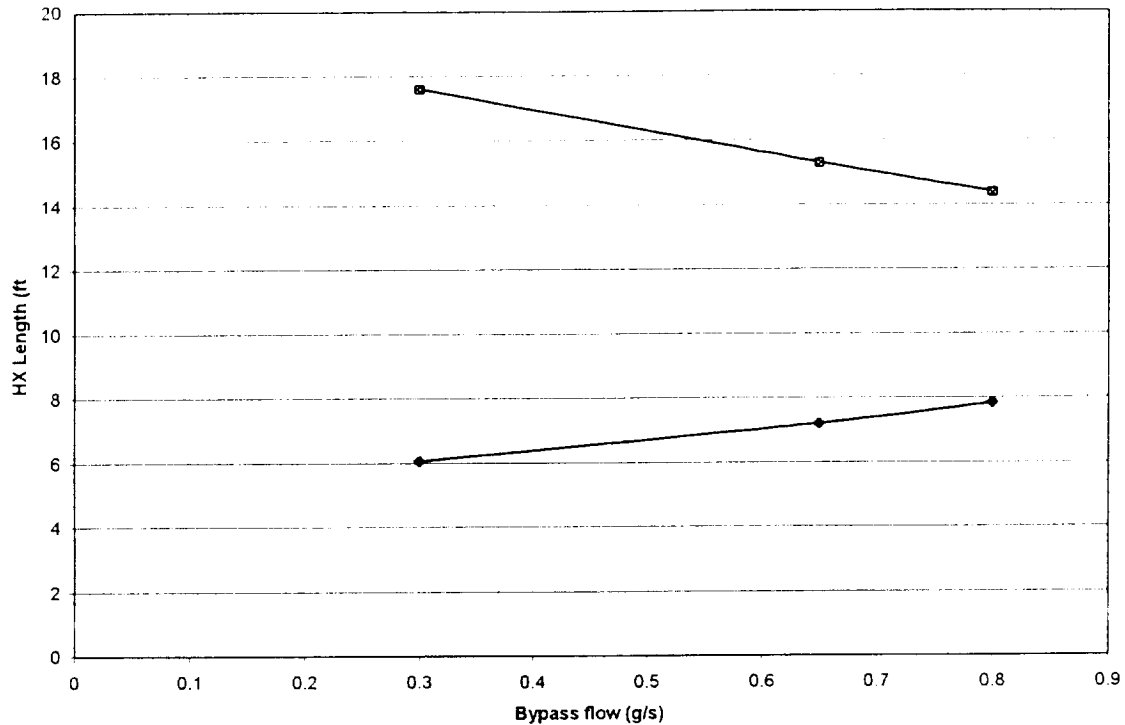


Figure 34: Heat Exchanger Length vs. Bypass Flow

Series 1 in the plot corresponds to the length of the bypass flow heat exchanger, while series 2 corresponds to the length of the separator gas flow heat exchanger. The length of the bypass exchanger varies from 6 to 8 feet and the length of the separator gas exchanger varies from approximately 14 to 18 feet. The OTS heat exchanger is 20 ft long and uses a larger tube, than the analysis indicates is necessary. Both of these factors should work to improve performance.

Hardware Procurement

The results of the hardware procurement are the acquired parts, which are shown in the following figures. In general, all parts were received to print. However, several non-conformances were noted on the assembly log. The assembly layout shows a sufficiently large diameter at the turbine exhaust port through hole in the main housing to facilitate removal of the turbine nozzle ring (volute). However, the detail print did not specify the correct through hole diameter (the through hole in the main housing was smaller than the through

hole in the nozzle ring) thus preventing removal of the nozzle ring for disassembly. Unfortunately, this was not discovered until after the first build. The remaining housings were re-worked at AFAB to the intended dimension. Additionally, the rotor did not have a recessed radius on each side of the thrust disk. Instead, it had a conventional radius. To prevent an interference, a break edge was added to the thrust bearing.

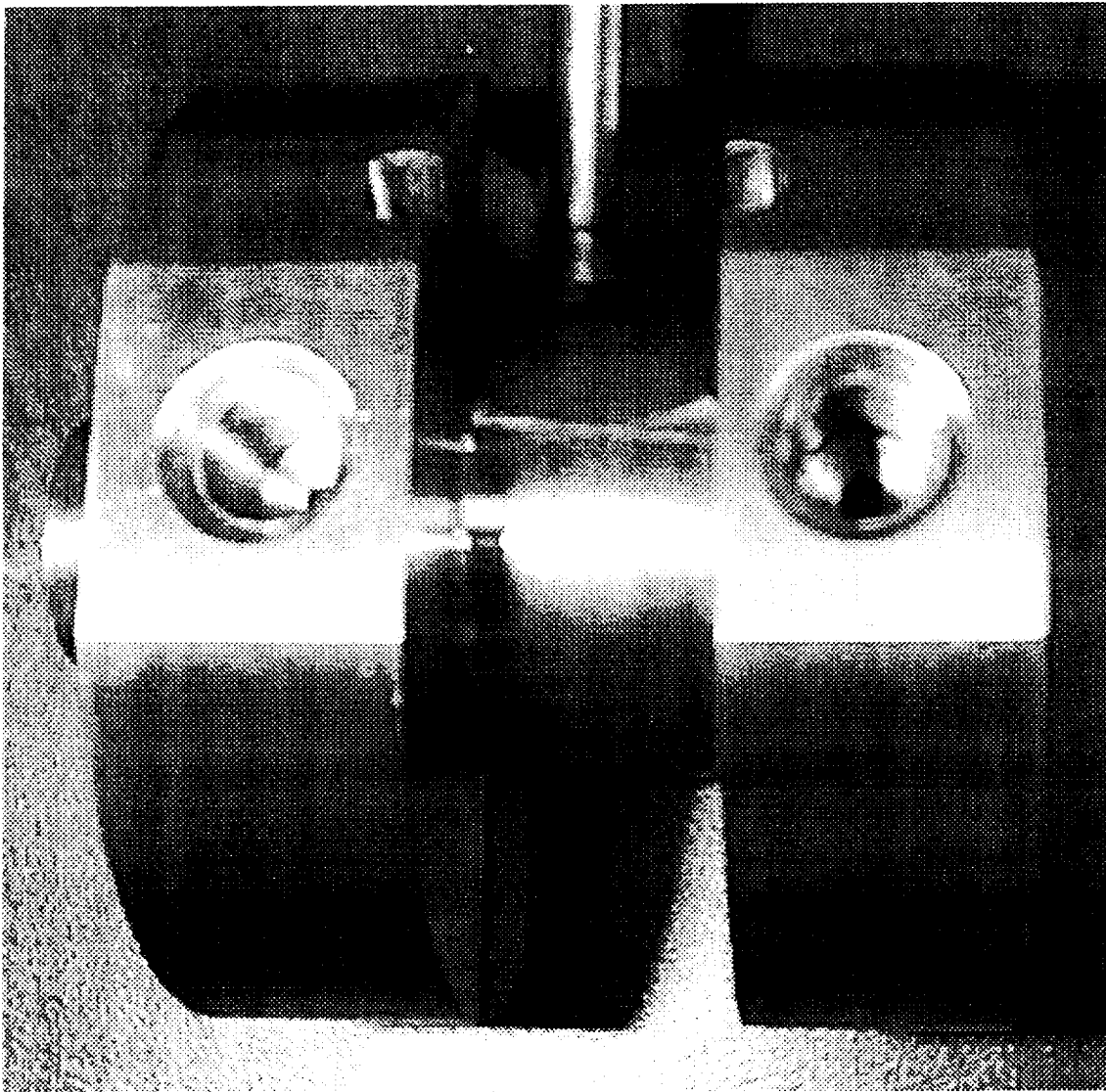


Figure 35: Turbocompressor Housing

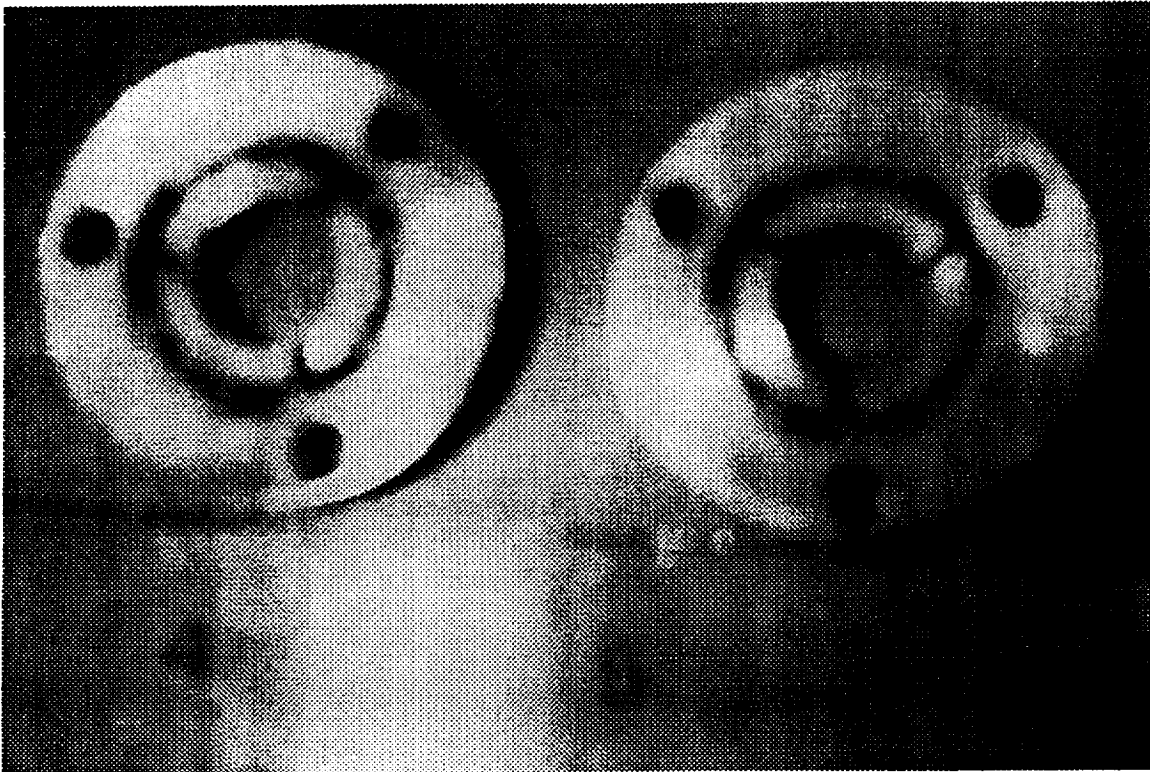


Figure 36: Journal Bearings

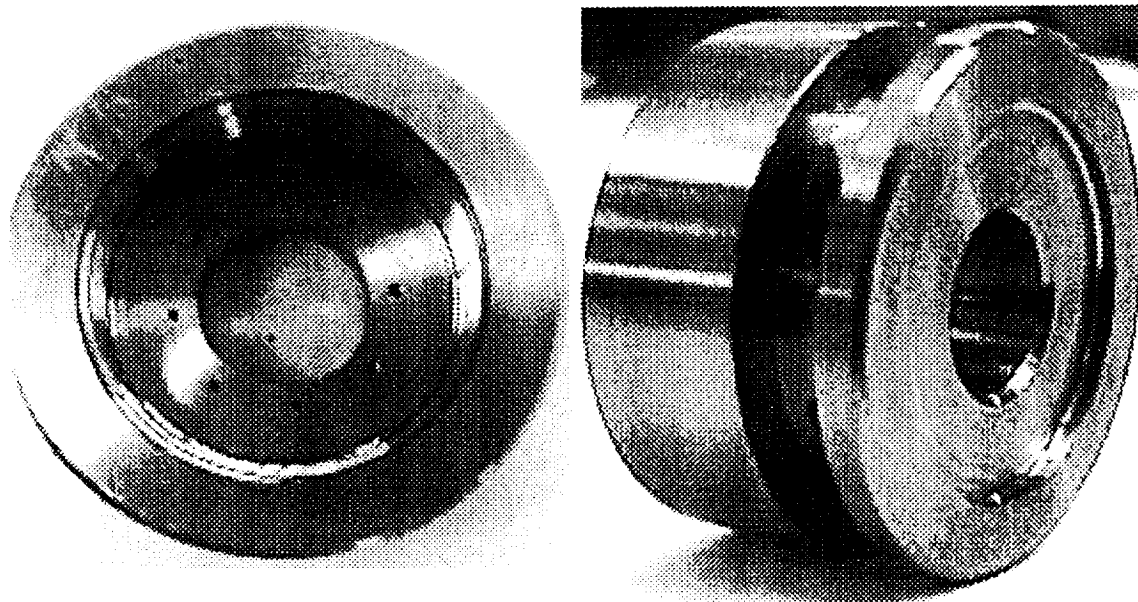


Figure 37: Thrust Bearing

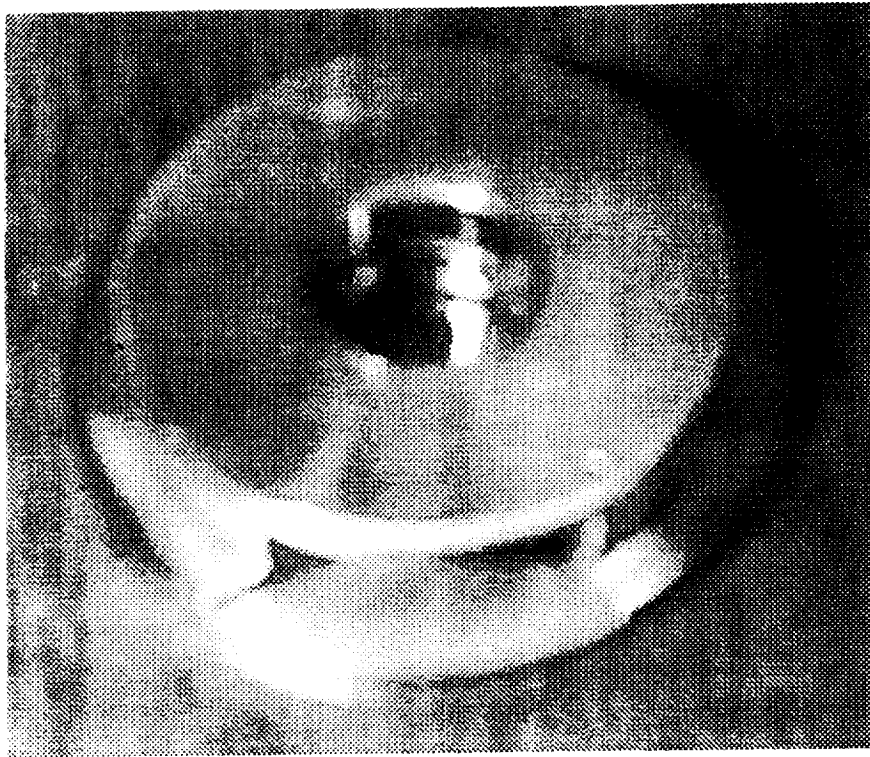


Figure 38: Turbine Nozzle Ring (Volute)

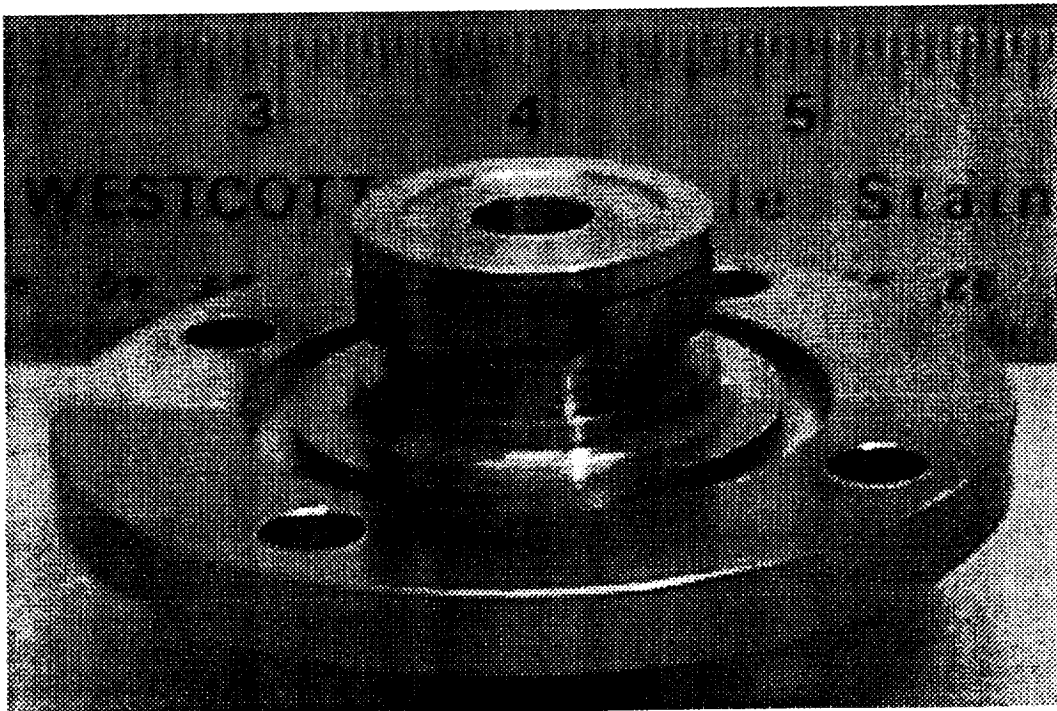


Figure 39: Cover

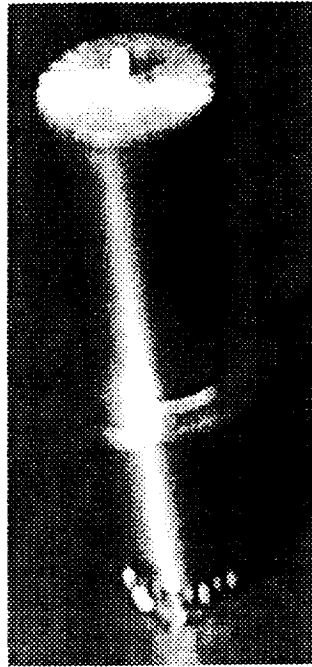


Figure 40: Rotor

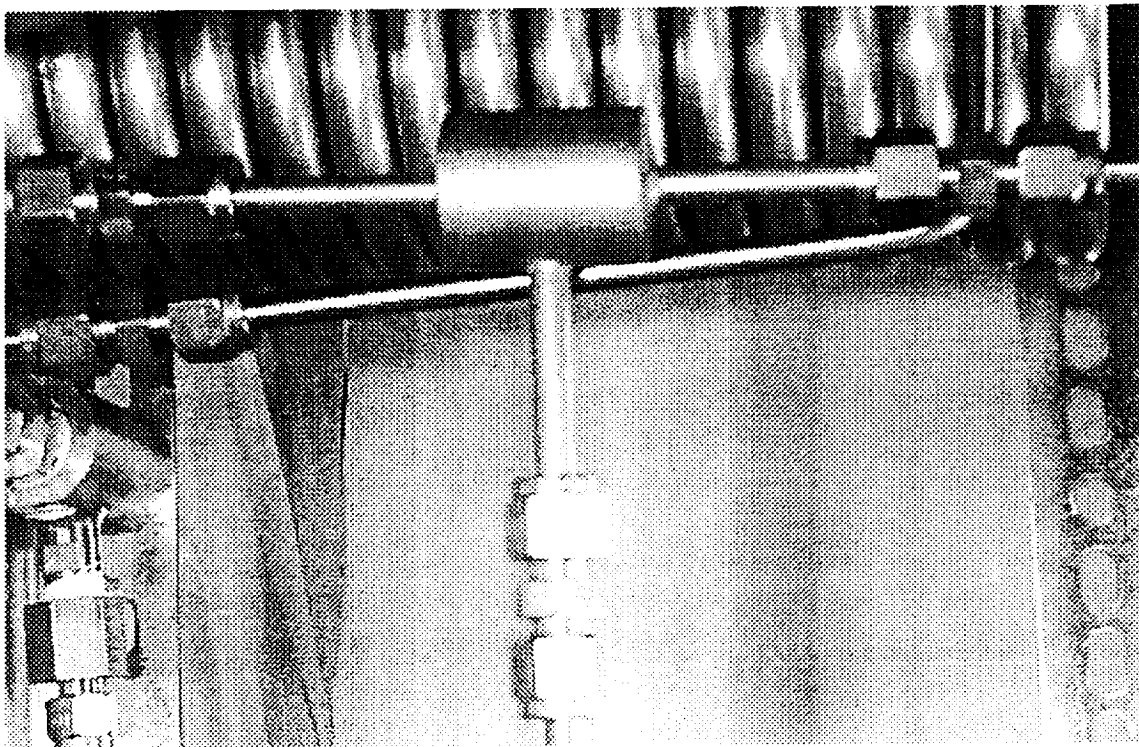


Figure 41: Separator (near), Heat Exchanger (far), and JT (in union)

Component Tests

The PC-Based, LabVIEW data acquisition system was setup to interface with the input/output cards. A test control panel was created to display the acquired data and activate data logging. A sample screen is shown in Figure 42. All the instrumentation came with calibration sheets providing traceability to the National Institute for Standards and Testing (NIST). Additionally, the calibrations were verified by AFAB Technologies to ensure proper operation with the data acquisition system. A sample calibration curve for the pressure transducers is shown in Figure 43.

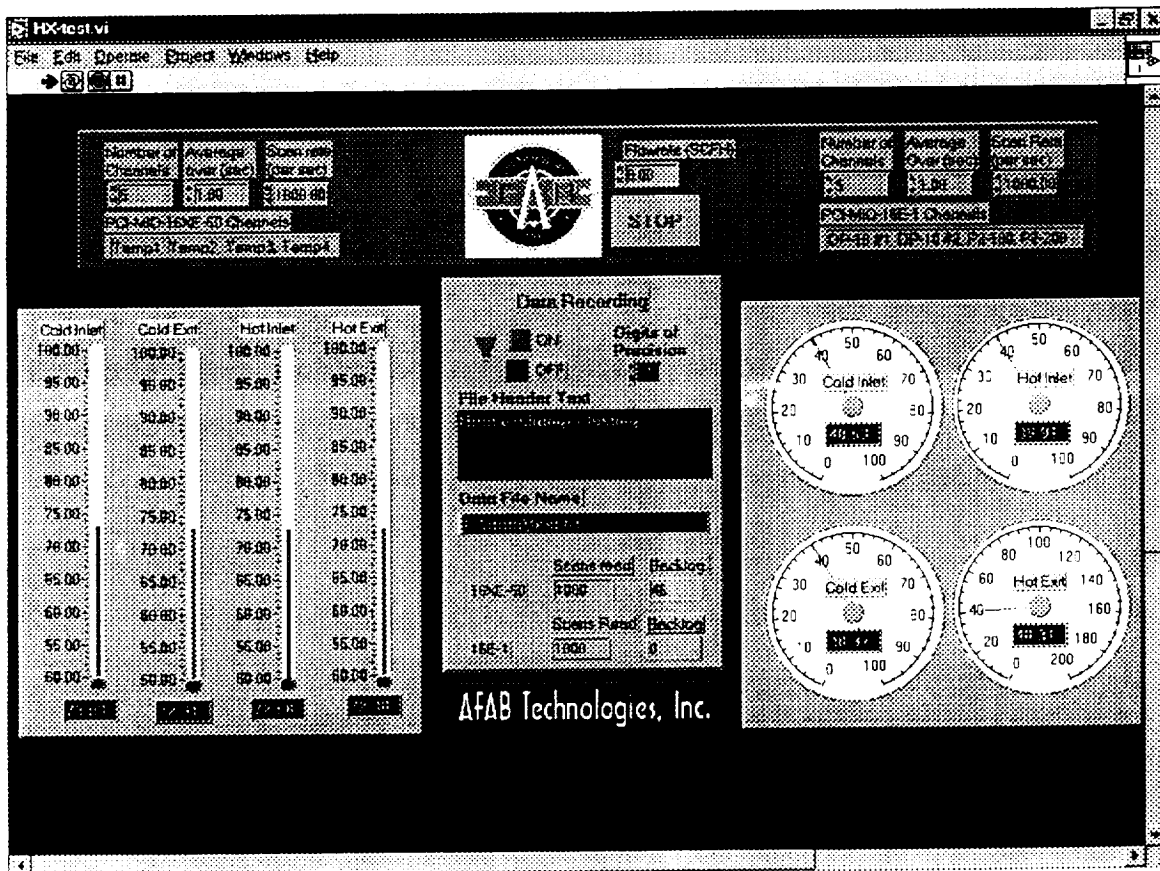


Figure 42: Sample Data Acquisition Screen

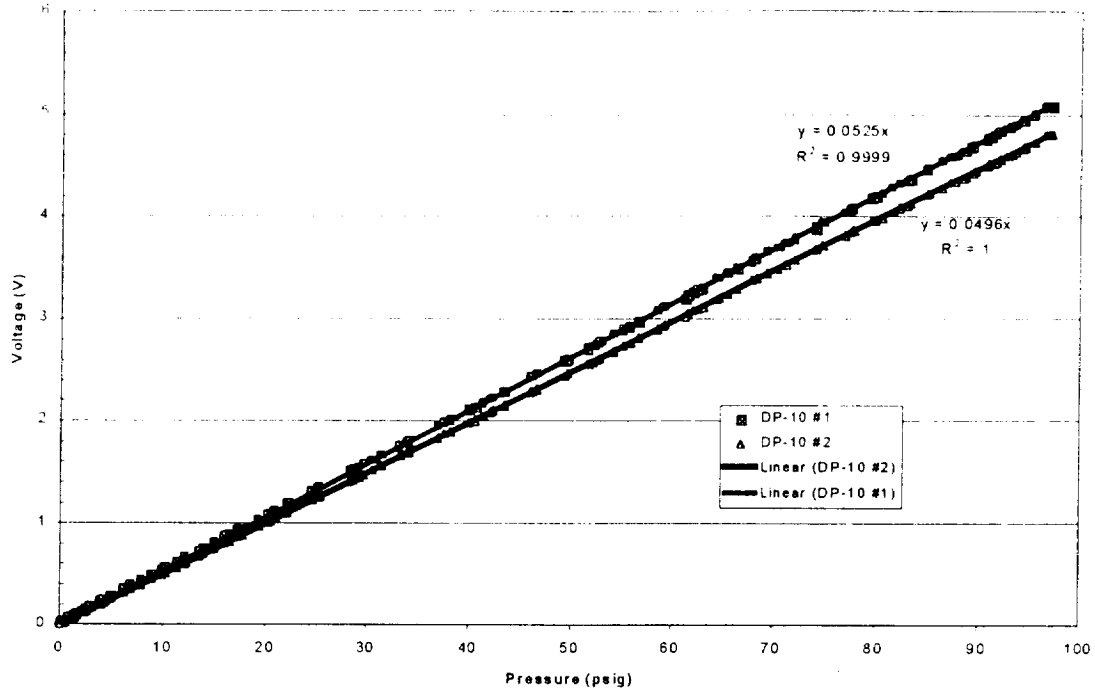


Figure 43: Sample Pressure Transducer Calibration Curve

The journal bearing spring rates were measured as a function of web thickness. The highly non-linear spring rate is theorized to be the result of the complex web geometry and possible influence from the EDM re-cast layer formed during manufacturing (Figure 44).

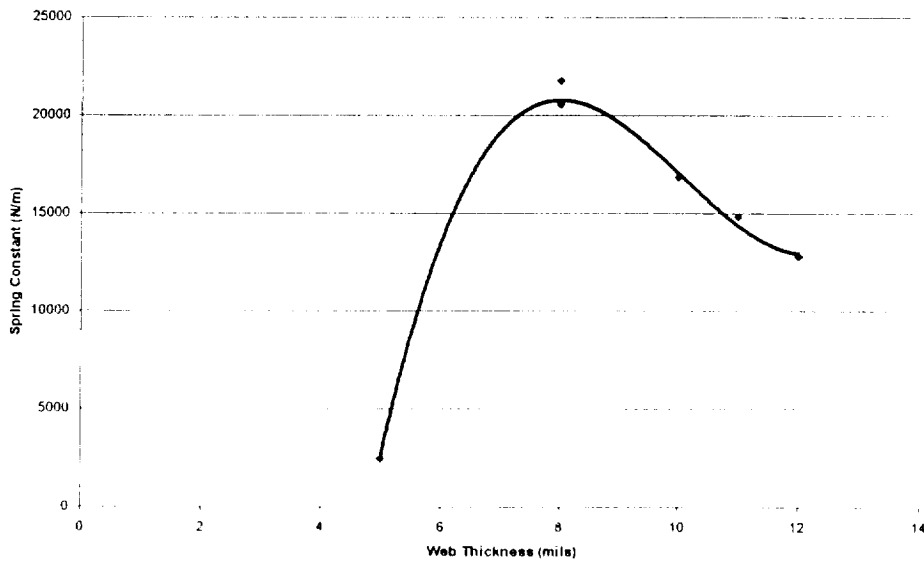


Figure 44: Journal Bearing Web Springrate

The orifices were tested for use as both the bypass flow control and the J-T valve. Various office sizes were tested to ensure a bypass flowrate of 0.00198 lbm/sec at a pressure ratio of 4. The results are shown in Figure 45 through Figure 49. This testing determined that a 0.035 inch diameter orifice provides the desired flow rate required to maximize liquid yield.

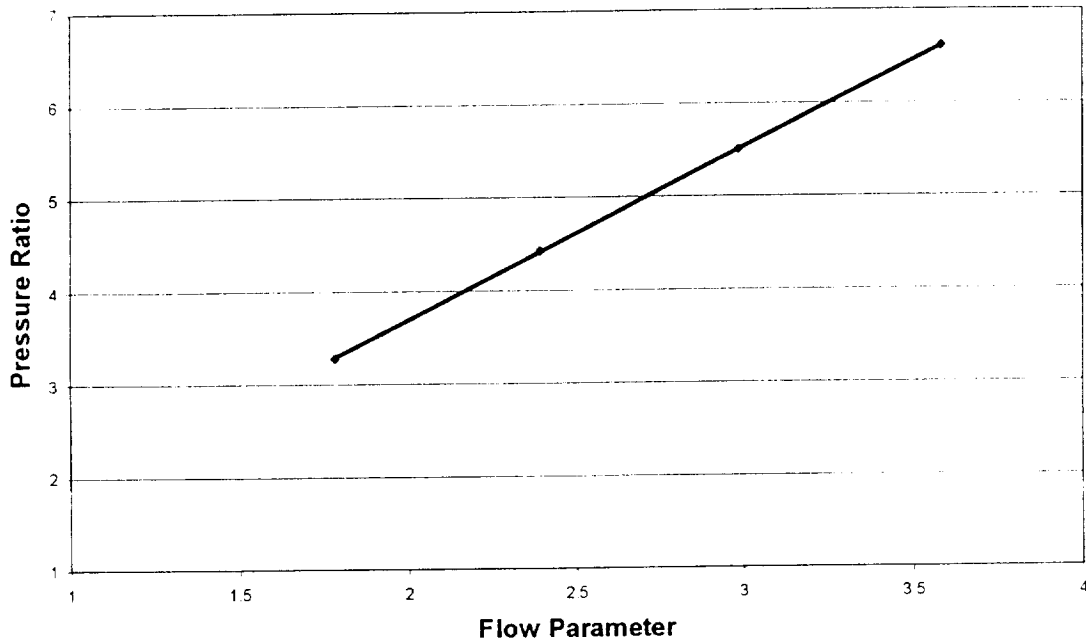


Figure 45: 0.026 inch Diameter Orifice

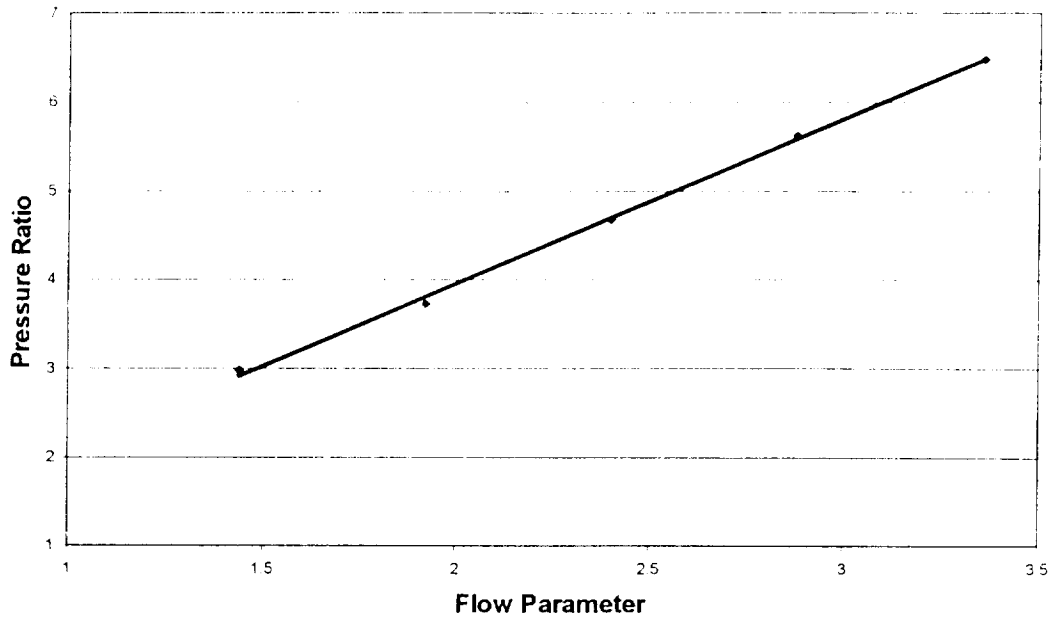


Figure 46: 0.029 inch Diameter Orifice

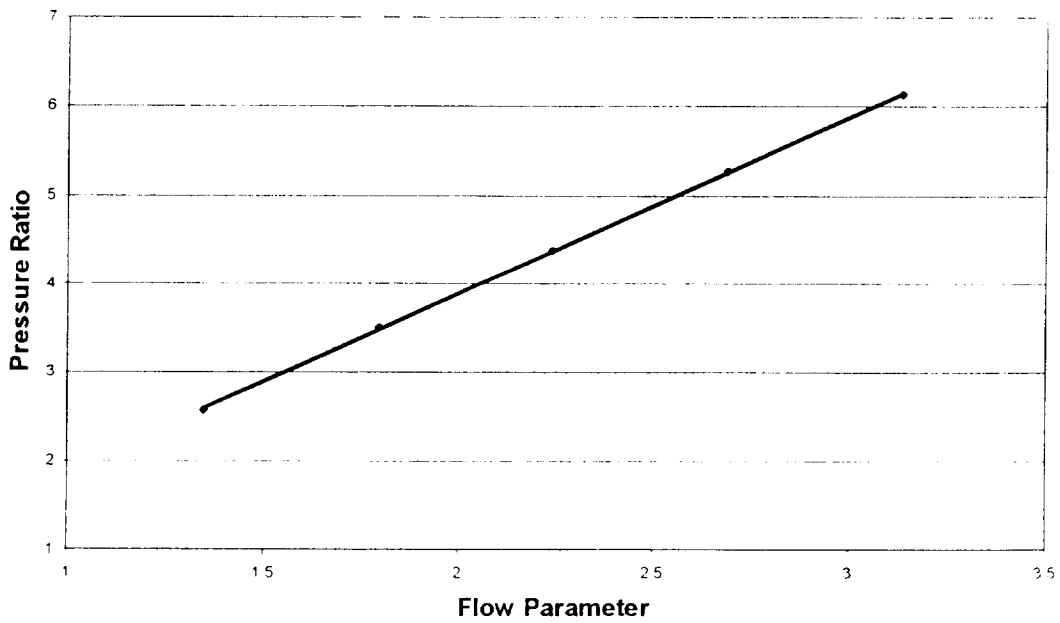


Figure 47: 0.030 inch Diameter Orifice

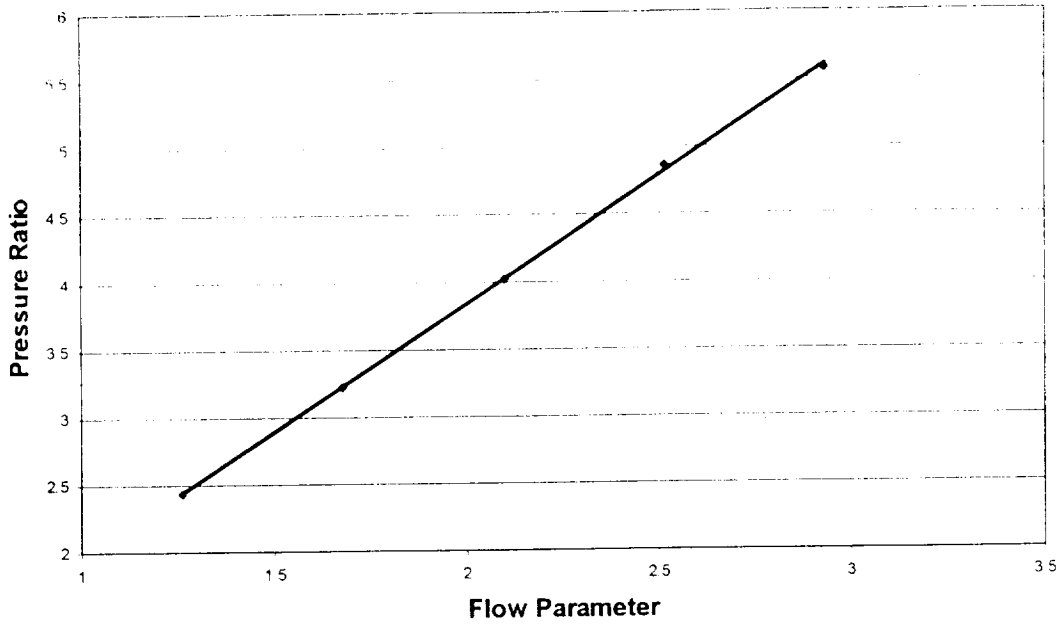


Figure 48: 0.031 inch Diameter Orifice

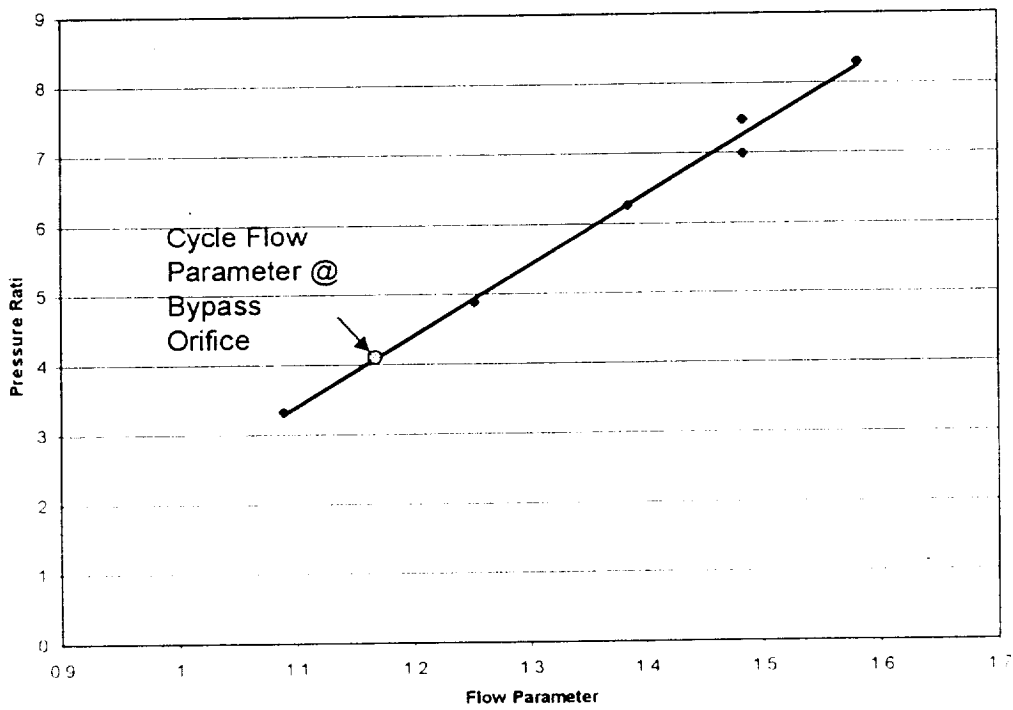


Figure 49: 0.035 inch Diameter Orifice

The JT orifice was tested at varying flow rates, pressures, and temperatures to evaluate its performance. The results are plotted in Figure 50.

$$\text{JT Factor} = h_{\text{downstream}}/h_{\text{upstream}}$$

Where:

$h_{\text{downstream}}$ is the enthalpy of the gas downstream of the JT valve, and
and h_{upstream} is the enthalpy of the gas upstream of the JT valve.

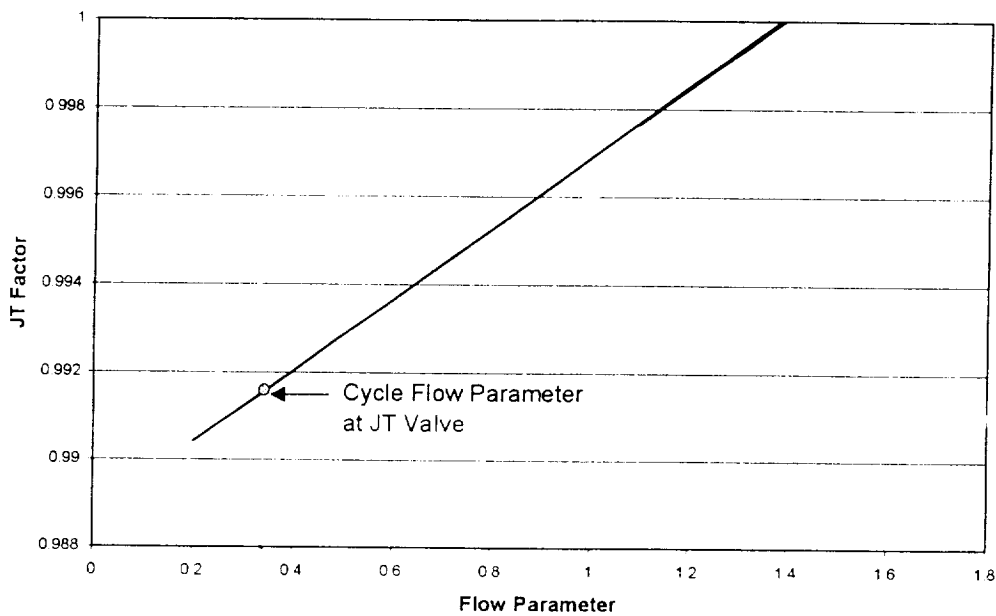


Figure 50: J-T Factor vs. Flow Parameter for 0.035 inch Orifice

The heat exchangers were tested at different temperatures, pressures, and flow rates to determine the effectiveness of each. The results are shown in Figure 51. The resulting effectiveness for the expected conditions at the compressor discharge is 0.9975.

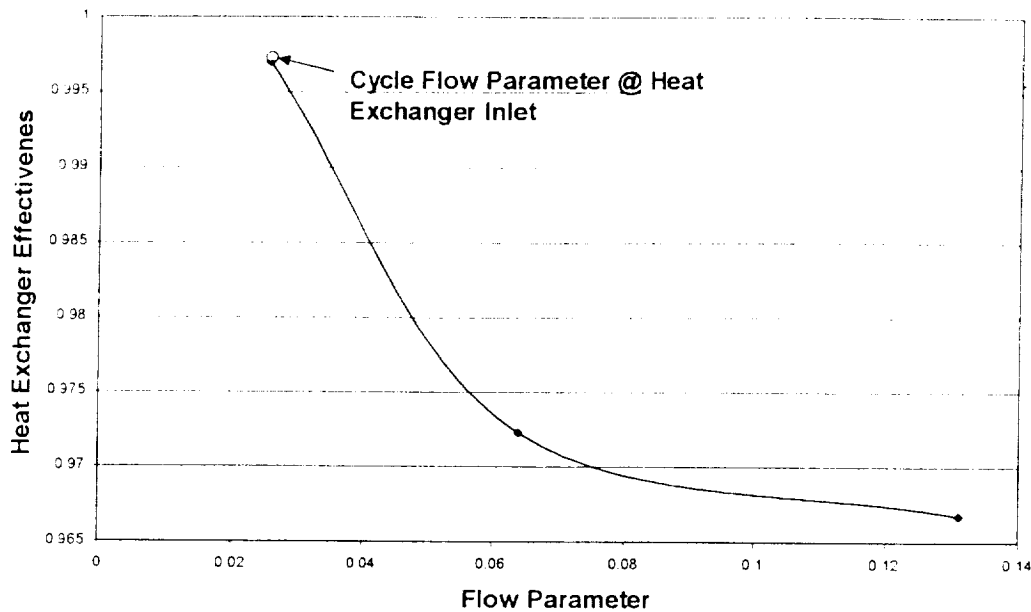


Figure 51: Heat Exchanger Efficiency vs. Flow Parameter

System Tests

Several system configurations were built and tested. The major differences from build-to-build were the turbocompressor fits and clearances, and the J-T and bypass orifice sizes. Numerous issues were encountered during turbocompressor assembly.

The turbine nozzle ring (volute) could not be successfully installed in the housing with an arbor press. While the part was being pressed in, it would deflect in an oil can manner causing the inboard half of the volute to fall to the bottom of the housing. Although it could be re-seated, there was no way to ensure the circumferential orientation was correct. Therefore, the part was installed after it was chilled in liquid nitrogen and the housing was heated with a heat gun. By heating and chilling, the part installed properly without issue.

As each part was installed, axial dimensions were measured to ensure it was completely seated prior to installation of the subsequent part. This process continued with the addition of the turbine-end journal bearing, thrust bearing, and rotor. Once the rotor was installed, a critical dimension was taken from the back of the thrust disk to the top of the housing to calculate the shim necessary to set the compressor shroud clearance (see Figure 52). After this process, the compressor-end journal bearing was installed, followed by the cover.

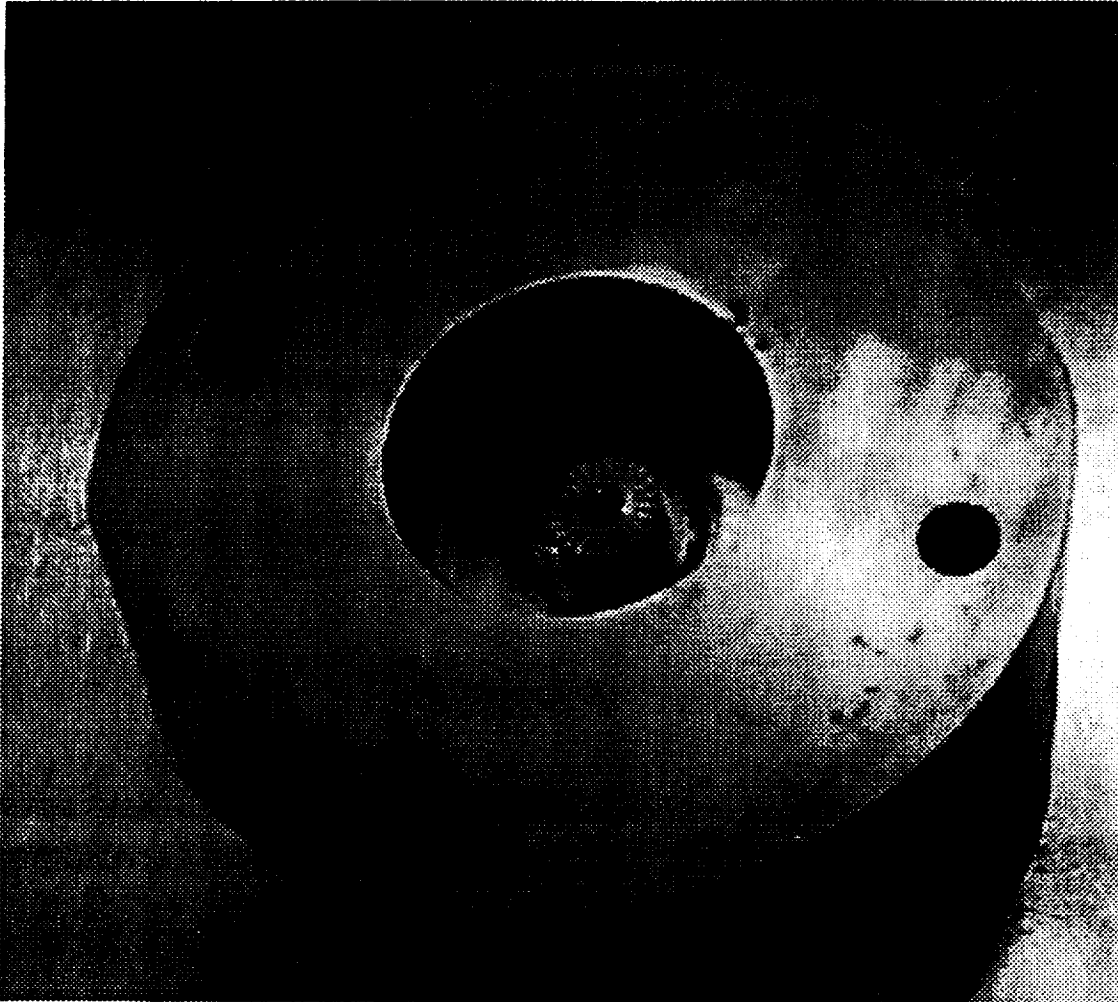


Figure 52: *Turbocompressor Rotor Stack*

The initial build was tested in air and the rotor locked-up immediately. The turbocompressor was then disassembled where two additional observations were noted. First, the disassembly thread on the thrust bearing needs to be changed to a standard size (from 0.75 inches – 28 to 0.75 inches – 16). Second, the disassembly threads on the journal bearing (for jacking screws) need to be changed to a standard size (from #8-36 to #8-32). Although the ultra-fine threads are desirable for disassembly, they are difficult to acquire.

Witness marks on the rotor indicated it was bound radially at the turbine nozzle ring. A review of the design showed a potential radial interference due to insufficient feature control of the relative concentricities for the mating parts. The tolerance stack-up for concentricity provided the opportunity to more than exceed the desired build and operating clearances. To address this issue with the hardware we had, each part was inspected and selected based on its fit with the mating part. Virtually every part selected was honed and polished to

optimize its fit and clearance to the extent possible. The remaining turbocompressor builds used this process for hardware selection and were built to the previously described build process. Unfortunately, the polishing could not overcome the concentricity tolerance issue. Each test resulted in immediate rotor seizure (although the remaining rotors seized in the journal bearings rather than the turbine volute). Turbocompressors were tested both by themselves and as part of the system tests. A system test setup is shown in Figure 53. The yellow rectangles are Type "E" (chromal constantine) thermocouples and the cylinders are pressure transducers.

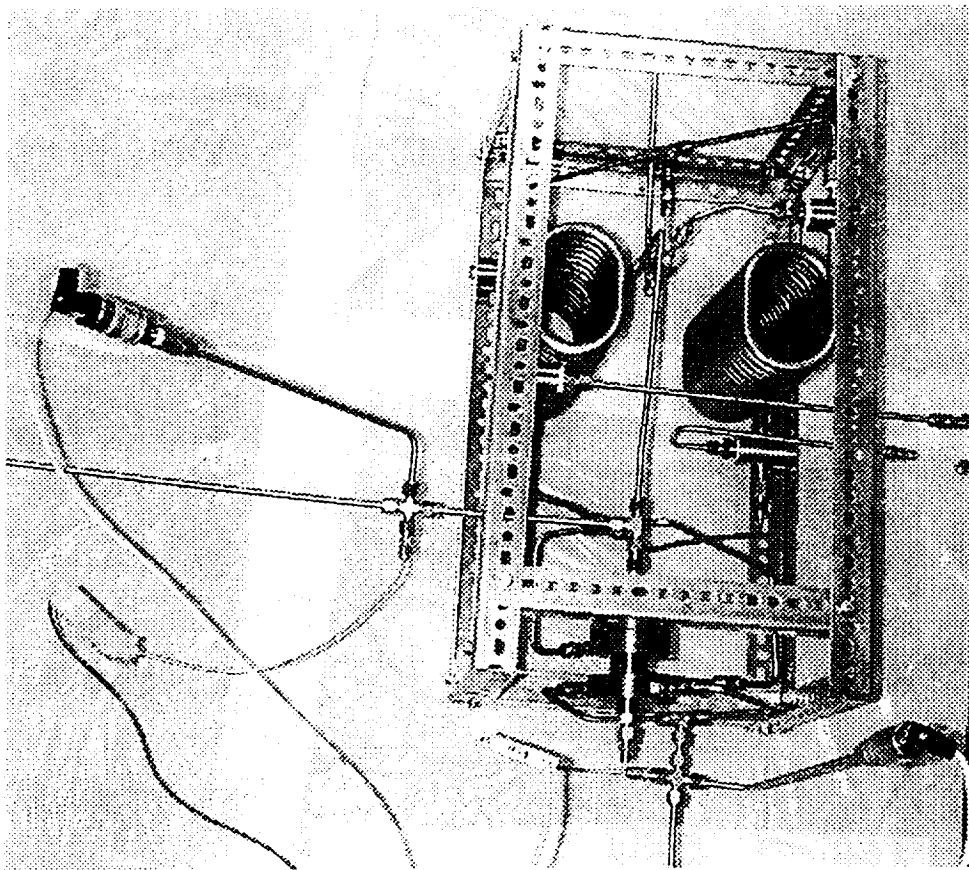


Figure 53: System Test Setup

Figure 54 shows the effect of heat exchanger effectiveness on the liquid yield of the system. The measured heat exchanger effectiveness results in a liquid yield of slightly more than 31.2 percent. However, because the JT factor of the orifice is less than one, the liquid yield of the system is lowered to 31 percent as shown in Figure 55.

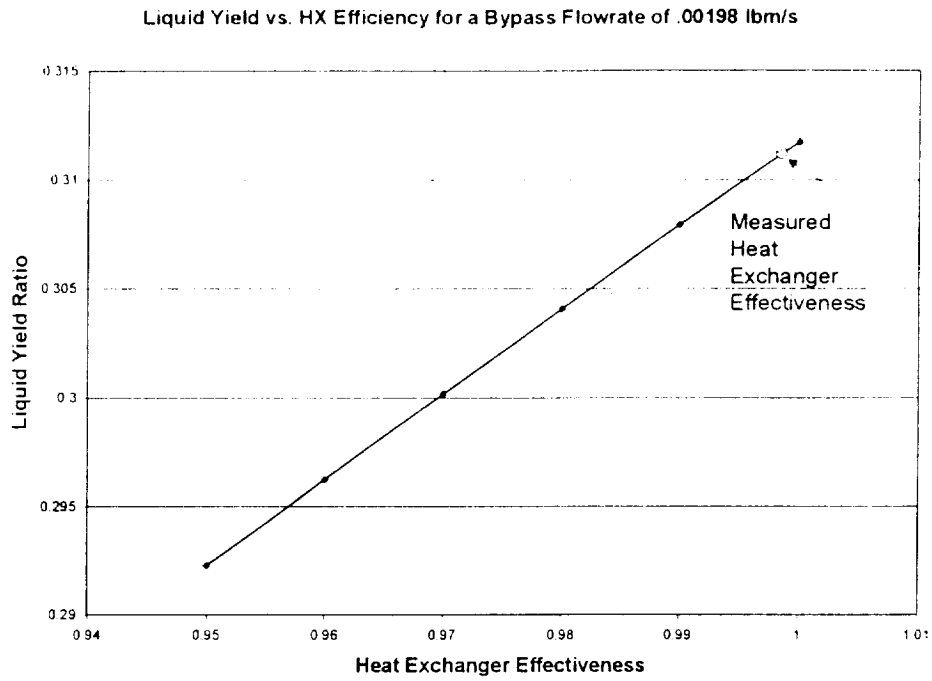


Figure 54: Liquid Yield vs. Heat Exchanger Efficiency

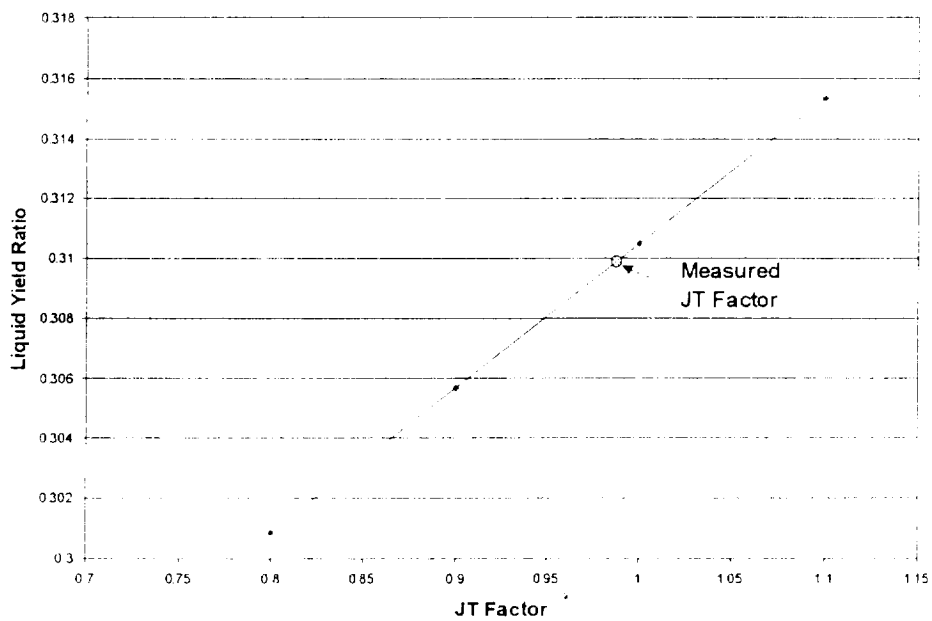


Figure 55: Liquid Yield vs. JT Factor

Prototype Tests

The test results from the system testing were used to finalize the orifice sizes for the bypass flow control and Joule-Thompson valve. A final build of the turbocompressor was attempted and the prototype system (same as the system test configuration without instrumentation) was assembled. The prototype was tested in helium and again, the rotor locked-up immediately. Therefore, the prototype was not insulated, thus allowing immediate access to the turbocompressor for subsequent re-work. The prototype, along with the remaining hardware, was packaged and sent to Stennis Space Center (see Figure 56).

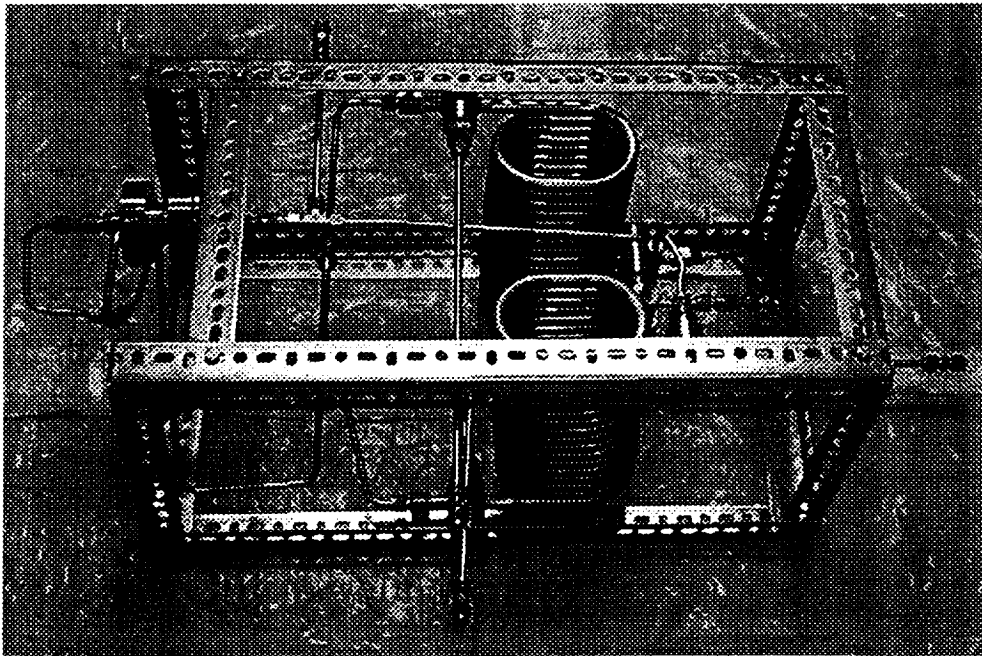


Figure 56: *Prototype System*

Technical Merit and Feasibility Assessment

The liquid hydrogen boil-off recovery system has significant technical merit. It is based on a modified Linde-Hampson cycle used previously to liquefy gases. Sub-component, component, and system level tests indicate 31 percent of the boil-off from a liquid hydrogen storage tank can be re-liquified.

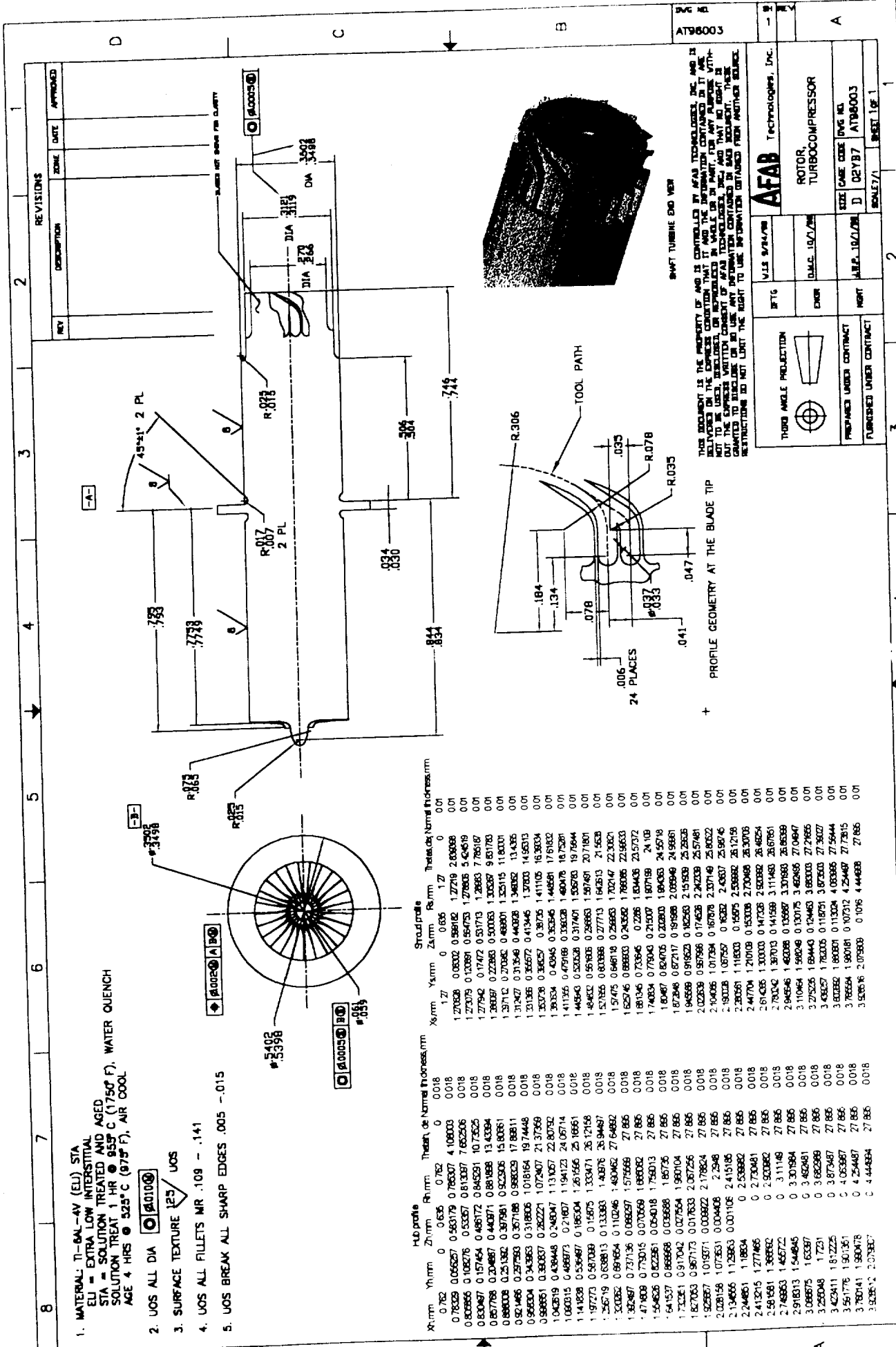
Two technical challenges were discovered as a result of the program: manufacturability of the compressor blades, and a rotor-to-stator clearance problem in the turbocompressor as a result of a concentricity tolerance stack-up. The compressor blade producibility challenge was overcome during the project and the rotors were successfully fabricated. The rotor-to-stator clearance/concentricity issue can be resolved by re-designing the parts to be line-bored in the housing, thus eliminating the tolerance stack-up.

However, if the technical challenges with the turbocompressor cannot be overcome, the turbocompressor can be replaced with an alternate means of compression. When it appeared the rotors could not be manufactured due to the compressor blade geometry, AFAB Technologies identified an electrically driven, cryogenic piston compressor which could be substituted into the system: Fluitron model AI-15-NL. This pump is roughly equivalent in cost and performance of the turbocompressor and thus will not impact the performance of the liquid hydrogen boil-off recovery system.

In low volume production, the system can be fabricated, assembled, tested, and delivered for less than \$30K per unit. A single 22,000 gallon low pressure liquid hydrogen storage tank loses \$20,000 per month due to boil-off. The liquid hydrogen boil-off recovery system would save \$7,000 per month based on a volumetric efficiency of 35 percent. Therefore, the system would pay for itself in approximately five months of service.

Appendix A

A-Size Detail Drawings



REV	DESCRIPTION	DATE	APPROVED

1. MATERIAL: Ti-6Al-4V (EU) STA
 EU = EXTRA LOW INTERSTITIAL
 STA = SOLUTION TREATED AND AGED
 SOLUTION TREAT 1 HR @ 855° C (1750° F), WATER QUENCH
 AGE 4 HRS @ 525° C (975° F), AIR COOL

2. UOS ALL DIA ϕ 0.0100

3. SURFACE TEXTURE $\sqrt{R_a}$ UOS

4. UOS ALL FILLETS MR .109 - .141

5. UOS BREAK ALL SHARP EDGES .005 - .015

Hub Profile		Shaft Profile		Throat de Normal Progress (mm)		Transition de Normal Progress (mm)	
Xr (mm)	Yr (mm)	Zr (mm)	Rr (mm)	Xs (mm)	Ys (mm)	Zs (mm)	Rs (mm)
0.762	0.0626	0.0636	0	1.7	0.036	1.27	0.0000
0.7629	0.06267	0.06367	0.0000	1.7008	0.0361	1.2719	0.0006
0.80965	0.10576	0.56379	0.76507	1.7038	0.03612	1.2729	0.0009
0.80967	0.10576	0.56387	0.81337	1.7079	0.03619	1.2763	0.0019
0.87078	0.20487	0.44371	0.48572	1.7292	0.03713	1.2853	0.0019
0.88708	0.23487	0.39781	0.88168	1.7692	0.03803	1.3037	0.0019
0.88708	0.23487	0.39781	0.92306	1.8110	0.03890	1.3215	0.0019
0.82146	0.25793	0.36708	0.98329	1.8547	0.03968	1.3385	0.0019
0.86604	0.34363	0.31806	1.01854	1.9000	0.04036	1.3546	0.0019
0.96851	0.50037	0.26229	1.07207	1.9468	0.04094	1.3698	0.0019
1.04219	0.63948	0.24094	1.13057	1.9950	0.04143	1.3841	0.0019
1.08015	0.69877	0.19604	1.19423	2.0446	0.04183	1.3975	0.0019
1.14828	0.83687	0.16204	1.26156	2.0954	0.04214	1.4100	0.0019
1.19773	0.87089	0.15875	1.33471	2.1474	0.04236	1.4216	0.0019
1.26519	0.89813	0.13380	1.42376	2.2004	0.04249	1.4322	0.0019
1.30382	0.89164	0.10246	1.49242	2.2544	0.04253	1.4419	0.0019
1.35287	0.757136	0.08627	1.57668	2.3092	0.04248	1.4507	0.0019
1.47809	0.73015	0.07059	1.68002	2.3648	0.04234	1.4586	0.0019
1.54626	0.62261	0.054018	1.79313	2.4211	0.04201	1.4657	0.0019
1.64137	0.66668	0.03668	1.90736	2.4781	0.04149	1.4720	0.0019
1.73261	0.91702	0.027654	1.99104	2.5356	0.04078	1.4766	0.0019
1.82703	0.87173	0.017633	2.07256	2.5934	0.04000	1.4795	0.0019
1.92567	1.01571	0.00822	2.17824	2.6514	0.03916	1.4808	0.0019
2.028156	1.07363	0.00408	2.298	2.7094	0.03828	1.4805	0.0019
2.13465	1.12663	0.001106	2.419136	2.7674	0.03735	1.4787	0.0019
2.24461	1.1834	0	2.53862	2.8254	0.03638	1.4754	0.0019
2.35815	1.24466	0	2.73041	2.8834	0.03528	1.4706	0.0019
2.47591	1.30992	0	2.92062	2.9414	0.03405	1.4643	0.0019
2.59781	1.37872	0	3.11148	2.9994	0.03269	1.4565	0.0019
2.72381	1.45095	0	3.30184	3.0574	0.03120	1.4472	0.0019
2.85381	1.52645	0	3.49261	3.1154	0.02959	1.4364	0.0019
2.98781	1.60515	0	3.68378	3.1734	0.02786	1.4241	0.0019
3.12581	1.68725	0	3.87535	3.2314	0.02601	1.4103	0.0019
3.26781	1.77275	0	4.06842	3.2894	0.02404	1.3950	0.0019
3.41381	1.86165	0	4.26399	3.3474	0.02196	1.3782	0.0019
3.56381	1.95395	0	4.46216	3.4054	0.01977	1.3600	0.0019
3.71781	2.04975	0	4.66293	3.4634	0.01747	1.3404	0.0019
3.87581	2.14905	0	4.86630	3.5214	0.01506	1.3194	0.0019
4.03781	2.25185	0	5.07227	3.5794	0.01254	1.2970	0.0019
4.20381	2.35815	0	5.28074	3.6374	0.00991	1.2732	0.0019
4.37381	2.46795	0	5.49171	3.6954	0.00717	1.2480	0.0019
4.54781	2.58125	0	5.70518	3.7534	0.00432	1.2214	0.0019
4.72581	2.69805	0	5.92115	3.8114	0.00136	1.1934	0.0019
4.90781	2.81935	0	6.13962	3.8694	0.00030	1.1640	0.0019
5.09381	2.94515	0	6.36059	3.9274	0.00024	1.1332	0.0019
5.28381	3.07545	0	6.58406	3.9854	0.00018	1.1010	0.0019
5.47781	3.21025	0	6.81003	4.0434	0.00012	1.0674	0.0019
5.67581	3.34955	0	7.03850	4.1014	0.00006	1.0324	0.0019
5.87781	3.49335	0	7.26947	4.1594	0.00000	0.9960	0.0019
6.08381	3.64165	0	7.50294	4.2174	0.00000	0.9582	0.0019
6.29381	3.79445	0	7.73891	4.2754	0.00000	0.9190	0.0019
6.50781	3.95175	0	7.97738	4.3334	0.00000	0.8784	0.0019
6.72581	4.11355	0	8.21835	4.3914	0.00000	0.8364	0.0019
6.94781	4.27985	0	8.46182	4.4494	0.00000	0.7930	0.0019
7.17381	4.45065	0	8.70779	4.5074	0.00000	0.7482	0.0019
7.40381	4.62595	0	8.95626	4.5654	0.00000	0.7020	0.0019
7.63781	4.80575	0	9.20723	4.6234	0.00000	0.6544	0.0019
7.87581	4.98995	0	9.46070	4.6814	0.00000	0.6054	0.0019
8.11781	5.17855	0	9.71667	4.7394	0.00000	0.5550	0.0019
8.36381	5.37155	0	9.97514	4.7974	0.00000	0.5032	0.0019
8.61381	5.56895	0	10.23611	4.8554	0.00000	0.4500	0.0019
8.86781	5.77075	0	10.49958	4.9134	0.00000	0.3954	0.0019
9.12581	5.97695	0	10.76555	4.9714	0.00000	0.3394	0.0019
9.38781	6.18755	0	11.03402	5.0294	0.00000	0.2820	0.0019
9.65381	6.40255	0	11.30599	5.0874	0.00000	0.2232	0.0019
9.92381	6.62195	0	11.58146	5.1454	0.00000	0.1630	0.0019
10.19781	6.84575	0	11.86043	5.2034	0.00000	0.1014	0.0019
10.47581	7.07395	0	12.14290	5.2614	0.00000	0.0384	0.0019
10.75781	7.30655	0	12.42887	5.3194	0.00000	0.0000	0.0019
11.04381	7.54355	0	12.71734	5.3774	0.00000	0.0000	0.0019
11.33381	7.78495	0	13.00931	5.4354	0.00000	0.0000	0.0019
11.62781	8.03075	0	13.30478	5.4934	0.00000	0.0000	0.0019
11.92581	8.28095	0	13.60375	5.5514	0.00000	0.0000	0.0019
12.22781	8.53555	0	13.90622	5.6094	0.00000	0.0000	0.0019
12.53381	8.79455	0	14.21219	5.6674	0.00000	0.0000	0.0019
12.84381	9.05795	0	14.52166	5.7254	0.00000	0.0000	0.0019
13.15781	9.32575	0	14.83463	5.7834	0.00000	0.0000	0.0019
13.47581	9.59795	0	15.15110	5.8414	0.00000	0.0000	0.0019
13.79781	9.87455	0	15.47107	5.8994	0.00000	0.0000	0.0019
14.12381	10.15555	0	15.79454	5.9574	0.00000	0.0000	0.0019
14.45381	10.44095	0	16.12151	6.0154	0.00000	0.0000	0.0019
14.78781	10.73075	0	16.45198	6.0734	0.00000	0.0000	0.0019
15.12581	11.02495	0	16.78595	6.1314	0.00000	0.0000	0.0019
15.46781	11.32355	0	17.12242	6.1894	0.00000	0.0000	0.0019
15.81381	11.62655	0	17.46239	6.2474	0.00000	0.0000	0.0019
16.16381	11.93395	0	17.80486	6.3054	0.00000	0.0000	0.0019
16.51781	12.24575	0	18.15083	6.3634	0.00000	0.0000	0.0019
16.87581	12.56195	0	18.50030	6.4214	0.00000	0.0000	0.0019
17.23781	12.88255	0	18.85327	6.4794	0.00000	0.0000	0.0019
17.60381	13.20755	0	19.20974	6.5374	0.00000	0.0000	0.0019
17.97381	13.53695	0	19.56971	6.5954	0.00000	0.0000	0.0019
18.34781	13.87075	0	19.93318	6.6534	0.00000	0.0000	0.0019
18.72581	14.20895	0	20.30015	6.7114	0.00000	0.0000	0.0019
19.10781	14.55155	0	20.67062	6.7694	0.00000	0.0000	0.0019
19.49381	14.89855	0	21.04459	6.8274	0.00000	0.0000	0.0019
19.88381	15.25095	0	21.42206	6.8854	0.00000	0.0000	0.0019
20.27781	15.60875	0	21.80303	6.9434	0.00000	0.0000	0.0019
20.67581	15.97195	0	22.18750	7.0014	0.00000	0.0000	0.0019
21.07781	16.34055	0	22.57547	7.0594	0.00000	0.0000	0.0019
21.48381	16.71455	0	22.96694	7.1174	0.00000	0.0000	0.0019
21.89381	17.09395	0	23.36191	7.1754	0.00000	0.0000	0.0019
22.30781	17.47875	0	23.76038	7.2334	0.00000	0.0000	0.0019
22.72581	17.86895	0	24.16235	7.2914	0.00000	0.0000	0.0019
23.14781	18.26455	0	24.56782	7.3494	0.00000	0.0000	0.0019
23.57381	18.66555	0	24.97679	7.4074	0.00000	0.0000	0.0019
24.00381	19.07195	0	25.38926	7.4654	0.00000	0.0000	0.0019
24.43781	19.48375	0	25.80523	7.5234	0.00000	0.0000	0.0019
24.87581	19.90095	0	26.22470	7.5814	0.00000	0.0000	0.0019
25.31781	20.32355	0	26.64767	7.6394	0.00000	0.0000	0.0019
25.76381	20.75155	0	27.07414	7.6974	0.00000	0.0000	0.0019
26.21381	21.18495	0	27.50211	7.7554	0.00000	0.0000	0.0019
26.66781	21.62375	0	27.93258	7.8134	0.00000	0.0000	0.0019
27.12581	22.06795	0	28.36555	7.8714	0.00000	0.0000	0.0019
27.58781	22.51755	0	28.80102	7.9294	0.00000	0.0000	0.0019
28.05381	22.97255	0	29.23899	7.9874	0.00000	0.0000	0.0019
28.52381	23.43295	0	29.68046	8.0454	0.00000	0.0000	0.0019
29.00781	23.89875	0	30.12543	8.1034	0.00000	0.0000	0.0019
29.49581	24.36995	0	30.57390	8.1614	0.00000	0.0000	0.0019
29.98781	24.84655	0	31.02587	8.2194	0.00000	0.0000	0.0019
30.48381	25.32855	0	31.48134	8.2774	0.00000	0.0000	0.0019
30.98381	25.81595	0	31.94031	8.3354	0.00000	0.0000	0.0019
31.48781	26.30875	0	32.40278	8.3934	0.00000	0.0000	0.0019
31.99581	26.80695	0	32.86875	8.4514	0.00000	0.0000	0.0019
32.50781	27.31055	0	33.33822	8.5094	0.00000	0.0000	0.0019
33.023							

1. MATERIAL: 71-8AL-4V WROUGHT TITANIUM ALLOY

2. UOS ALL DIA $\text{O} \text{ } \phi .010 \text{ } \text{B}$

3. SURFACE TEXTURE $125 \sqrt{\text{UOS}}$

4. UOS ALL FILLETS MR .005 - .015

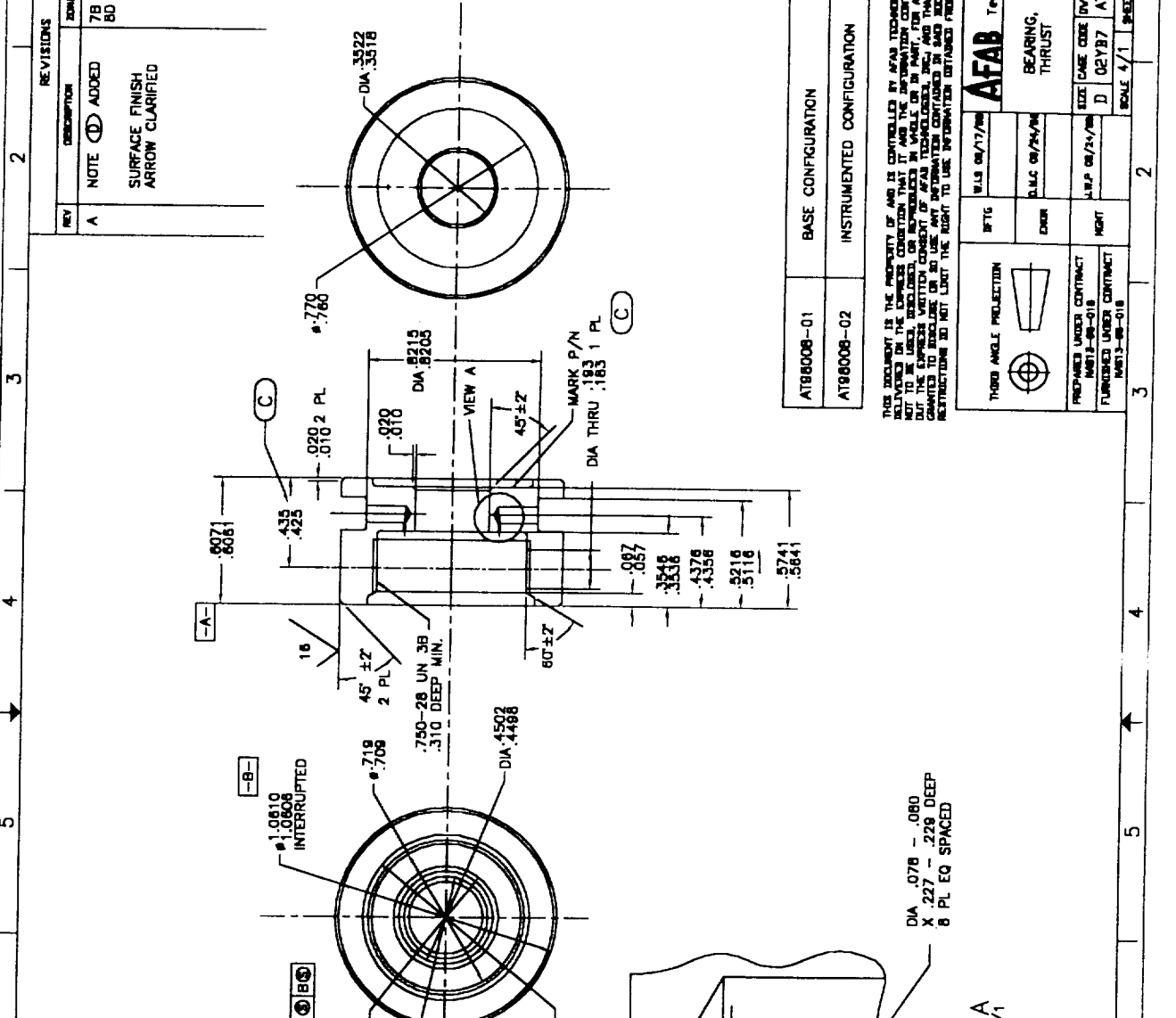
5. UOS BREAK ALL SHARP EDGES .005 - .015

6. ALL DIA $\text{I} \text{ } .002 \text{ } \text{A}$

7. C INSTRUMENTED CONFIGURATION ONLY

8. D EDM PERMITTED. RECAST LAYER REMOVAL NOT REQUIRED. IF EDM NOT FEASIBLE, 1/64 IN. DRILL W/ ELECTROLESS NICKEL PLATING TO CLOSE HOLE DOWN TO PRINT. AMS 2404 OR AMS 2424.

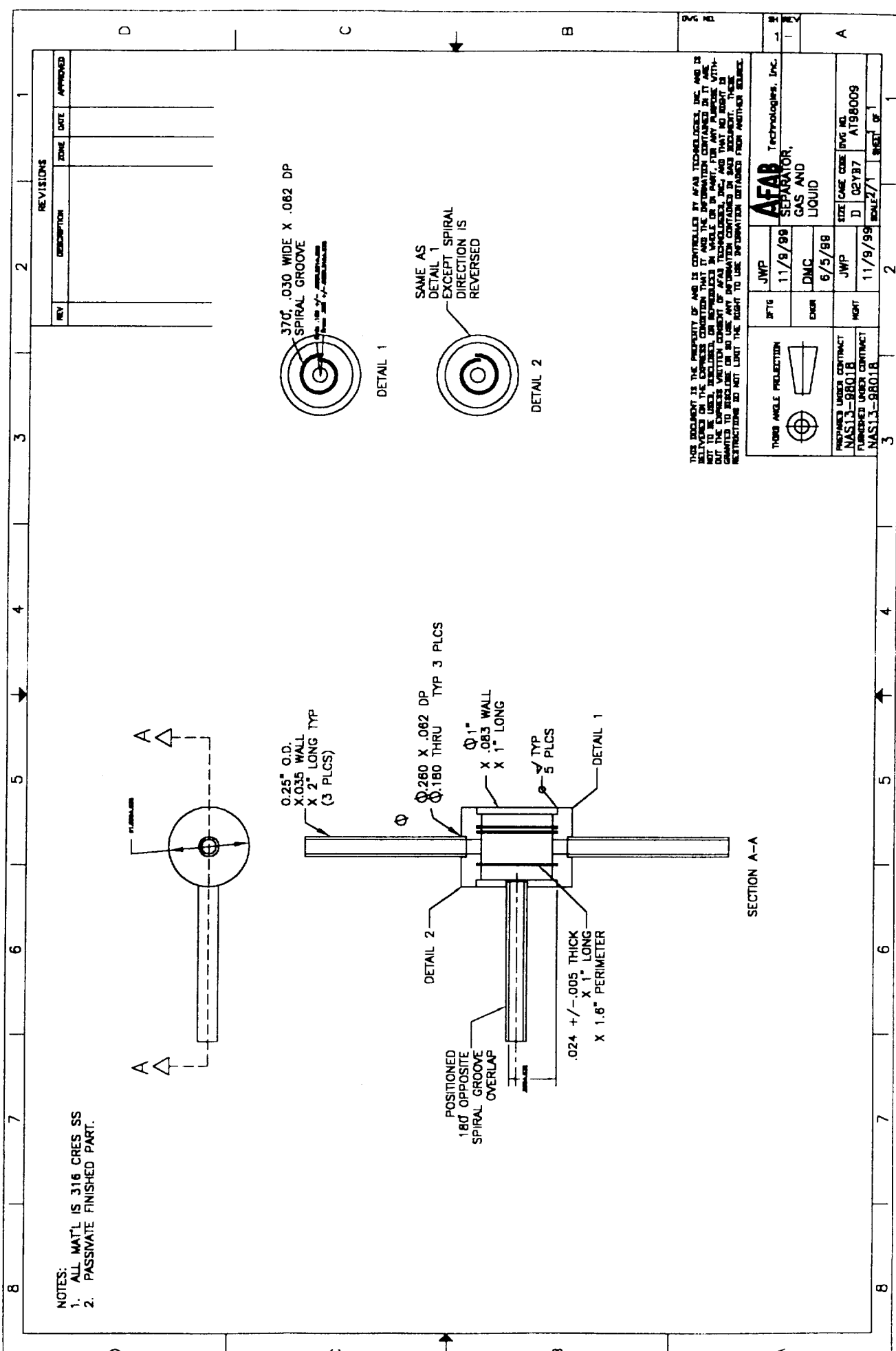
REV	DESCRIPTION	ZONE	DATE	APPROVED
A	NOTE C ADDED SURFACE FINISH ARROW CLARIFIED	7B 8D	1/11/88	JWP



AT88008-01	BASE CONFIGURATION
AT88008-02	INSTRUMENTED CONFIGURATION

THIS DOCUMENT IS THE PROPERTY OF AND IS CONTROLLED BY AFAB TECHNOLOGIES, INC. AND IS BELONGS TO THE USER UNDER THE CONDITION THAT IT AND THE INFORMATION CONTAINED HEREIN NOT BE LOANED, REPRODUCED, OR INCORPORATED IN WHOLE OR IN PART, FOR ANY PURPOSES WITHOUT THE WRITTEN PERMISSION OF AFAB TECHNOLOGIES, INC. AND THAT NO RIGHT IS GRANTED TO INCLUDE OR REPRODUCE IN ANY MANNER IN THIS DOCUMENT. THESE RESTRICTIONS DO NOT LIMIT THE RIGHT TO USE INFORMATION DERIVED FROM OTHER SOURCE.

THIRD ANGLE PROJECTION	DATE 08/17/88	AFAB Technologies, Inc.
BTIG	DATE 08/24/88	BEARING, THRUST
ENGR	DATE 08/24/88	
PREPARED UNDER CONTRACT	DATE 08/24/88	AFAB
FURNISHED UNDER CONTRACT	DATE 02/18/87	DWG NO. AT88008
MS13-88-018		SCALE 4/1
MS13-88-018		SHEET 1 OF 1



NOTES:
 1. ALL MAT'L IS 316 CRES SS
 2. PASSIVATE FINISHED PART.

REVISIONS			
REV	DESCRIPTION	ZONE	DATE

370° .030 WIDE X .062 DP
 SPIRAL GROOVE
 DETAIL 1

SAME AS
 DETAIL 1
 EXCEPT SPIRAL
 DIRECTION IS
 REVERSED
 DETAIL 2

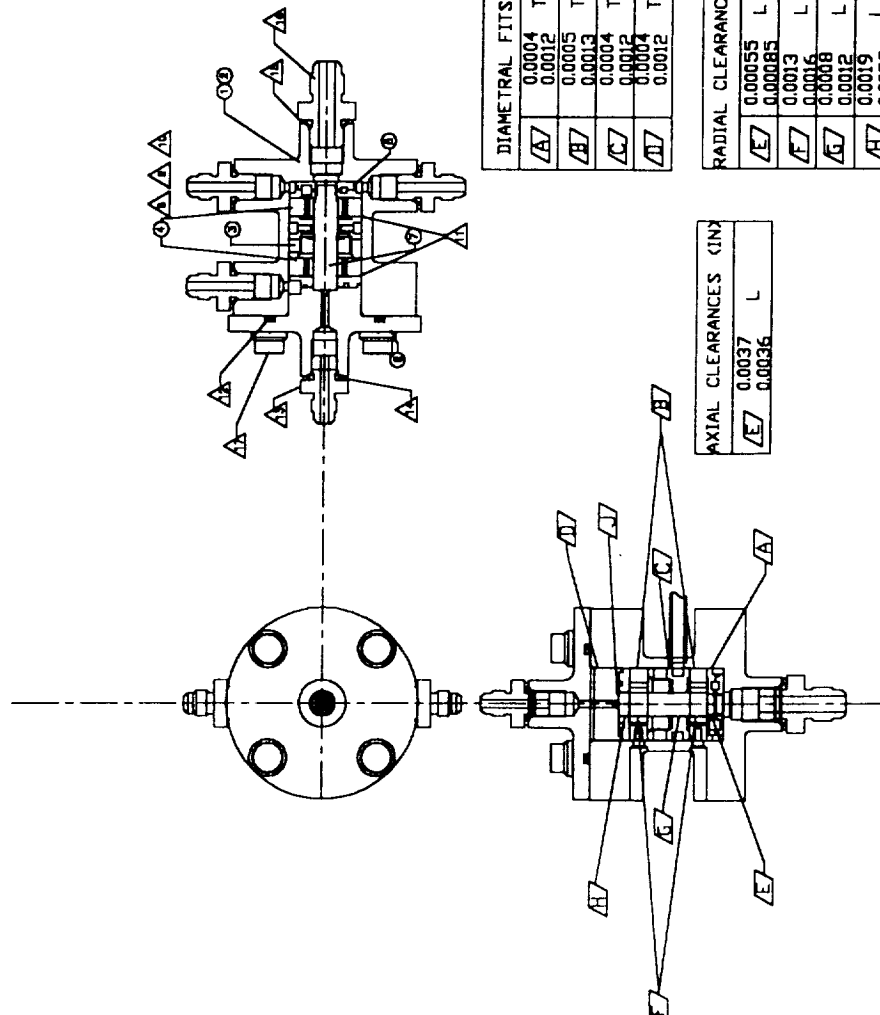
THIS DOCUMENT IS THE PROPERTY OF AND IS CONTROLLED BY AFAB TECHNOLOGIES, INC. AND IS
 BELIEVED ON THE EXPRESS CONDITION THAT IT AND THE INFORMATION CONTAINED IN IT ARE
 UNCLASSIFIED AND NOT SUBJECT TO EXPORT CONTROL RESTRICTIONS. IT IS HEREBY GRANTED
 OUT OF THE EXPRESS WRITTEN CONSENT OF AFAB TECHNOLOGIES, INC. THAT ANY INFORMATION
 CONTAINED HEREIN IS UNCLASSIFIED AND NOT SUBJECT TO EXPORT CONTROL RESTRICTIONS.
 RESTRICTIONS DO NOT LIMIT THE RIGHT TO USE INFORMATION OBTAINED FROM ANOTHER SOURCE.

 THREE ANGLE PROJECTION	 PART	JWP 11/8/99	AFAB Technologies, Inc. SEPARATOR, GAS AND LIQUID
 PREPARED UNDER CONTRACT NAS13-98018	 DRAWING	DMC 6/5/98	SIZE CASE CODE (DWG. NO.) D 02Y87 A198009
 FURNISHED UNDER CONTRACT NAS13-98018	 PART	JWP 11/9/99	SCALE 2/1 SHEET OF 1

SECTION A-A

8 7 6 5 4 3 2 1

NOTES:
 1. BEARING CLEARANCE TO BE ADJUSTED W/ ITEM 10 AT ASSY AND TUNED DURING ACCEPTANCE TESTING.
 2. SHIM AS REQ'D WITH 11 TO ACHIEVE AXIAL CLEARANCES AND K.
 3. TRIM BALANCE A/R DURING ACCEPTANCE TESTING.
 4. LAP MATING SURFACE SEAL GLANDS A/R.
 5. CLEAN ALL DETAIL PARTS AND SUB-ASSYS FOR HYDROGEN SERVICE.
 6. TORQUE PROGRESSIVELY TO 150 IN.-LB. IN OPPOSING PATTERN OF 25 IN.-LB. INCREMENTS.



DIAMETRAL FITS (IN)	
A/	0.0004 T
B/	0.0012 T
C/	0.0005 T
D/	0.0013 T
E/	0.0004 T
F/	0.0012 T
G/	0.0004 T
H/	0.0012 T

RADIAL CLEARANCES (IN)	
E/	0.00055 L
F/	0.00085 L
G/	0.0013 L
H/	0.0016 L
I/	0.0008 L
J/	0.0012 L
K/	0.0019 L
L/	0.0023 L

AXIAL CLEARANCES (IN)	
E/	0.0037 L
F/	0.0036 L

REVISIONS			
REV	DESCRIPTION	ZONE	DATE

UNIT/ ASSY	QTY	END. NO.	ZONE	PART NO.	DESCRIPTION	NOTES
1	1	1		AT98011	ASSY, CRYOGENIC TURBOCOMPRESSOR	5
1	1	2		AT98005	HOUSING, MAIN	5
1	1	3		AT98008	BEARING, THRUST	5
2	4	4		AT98004	BEARING, TILTING-PAD	1.5
1	5	5		AT98007	RING, TURBINE NOZZLE	5
1	1	6		AT98006	COVER, TURBOCOMPRESSOR	2.5
1	7	7		AT98003	ROTOR	3.5
6	6	8		D12-1	PIN, DOWEL	5
6	9	9		SPR8-1	SPRING	5
6	10	10		SC2-51	SCREW, SET	1.5
TBD	11	11			SHIM STOCK	2.5
4	4	12		MS9193-03	FACE SEAL, SPRING ENERGIZED	4
4	4	13		MS9193-03	THREADED BOSS	4.5
4	4	14		78007-15-2-SPA	SEAL, ENERRING	5
1	15	15		78007-15-2-SPA	SEAL, ENERRING	5
1	16	16		MS9193-03	THREADED BOSS	4.5
4	17	17		6757782	BOLT (.25-28 x 1")	5.6

THIS DOCUMENT IS THE PROPERTY OF AFAB AND IS LOANED TO YOU BY AFAB TECHNOLOGIES, INC. AND IS NOT TO BE USED, REPRODUCED OR TRANSMITTED IN ANY MANNER WITHOUT THE EXPRESS WRITTEN CONSENT OF AFAB TECHNOLOGIES, INC. AND THAT NO PART IS TO BE REPRODUCED OR TRANSMITTED IN ANY MANNER WITHOUT THE EXPRESS WRITTEN CONSENT OF AFAB TECHNOLOGIES, INC. THESE REPRODUCTIONS DO NOT LIMIT THE RIGHT TO USE INFORMATION CONTAINED HEREIN FOR ANY OTHER PURPOSE.

THIRD ANGLE PROJECTION

PREPARED UNDER CONTRACT NAS13-98018
 FURNISHED UNDER CONTRACT NAS13-98018

JVP 2/20/00
 DMC 2/20/00
 JVP 2/20/00
 DMC 2/20/00

AFAB Technologies, Inc.
 ASSY, TURBOCOMPRESSOR, LHBORS

SIZE CASE CODE DVG NO.
 D 02YB7 AT98011

SCALE 1/1 SHEET OF 1

Appendix B

Consultant's Report – Sensitivity Study

Rotordynamic Sensitivity Study

To analyze the effects of design changes or prediction errors in the dynamic characteristics of components, a sensitivity study was performed. The following parameters were varied to study their effect on the rotordynamic behavior of the rotor:

- 1) Bearing stiffness
- 2) Bearing damping
- 3) Shaft diameter
- 4) Compressor overhung weight
- 5) Turbine overhung weight
- 6) Thrust disk weight

7) Bearing Span

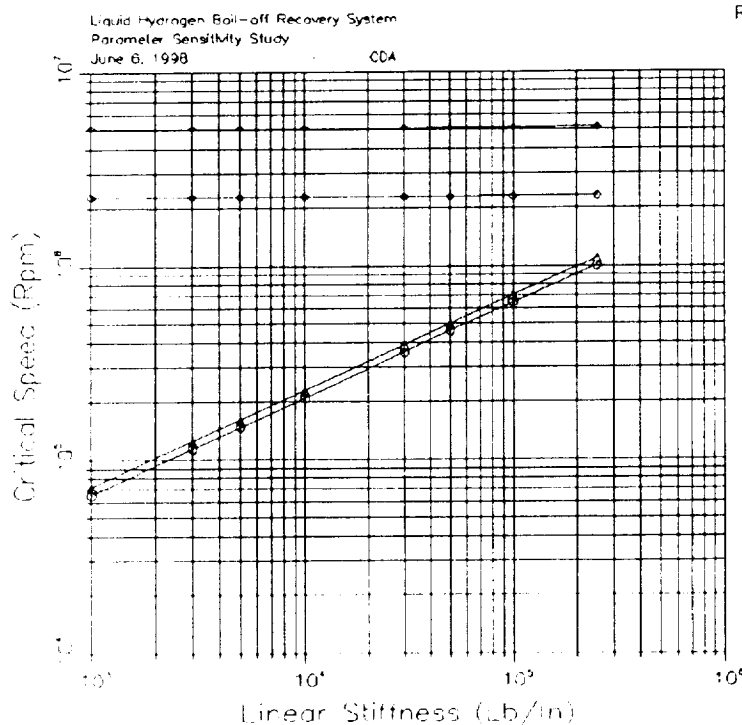
To analyze the effects on the rotor behavior of the design parameters, the undamped critical speeds are used to demonstrate changes in the frequency of the modes. It is desirable to maintain a separation margin between the operating speed range and the location of the critical speeds. The baseline design from Phase I provided separation margins in excess of 50% (20% is deemed marginal.) The response of the rotor to unbalance will be used to quantify the effects of changes in the bearing coefficients. The results of the study are summarized below.

Baseline

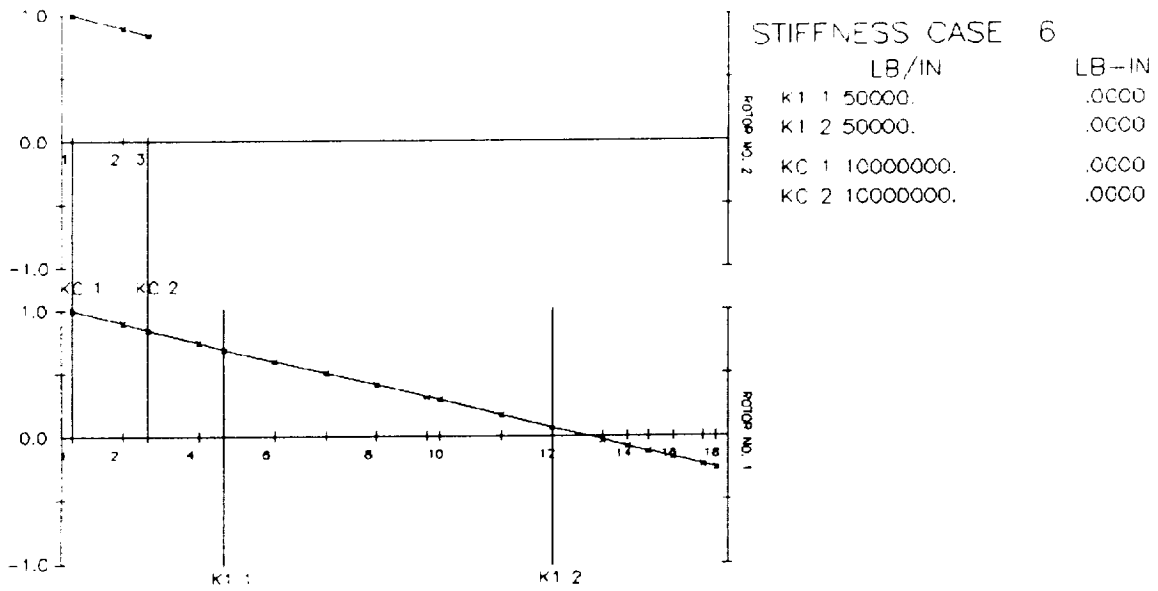
Three levels of stiffness were selected corresponding to the approximate magnitudes of the predicted bearing stiffness at minimum, maximum and nominal clearance. These are shown below along with the first three critical speeds.

Bearing Stiffness (lbf/in)	Baseline Critical Speed (rpm)		
	1	2	3
10,000	207,735	227,252	2,285,921
50,000	462,069	505,440	2,289,703
250,000	1,006,321	1,098,858	2,312,605

The undamped critical speed map and mode shapes are graphically shown below for a bearing stiffness of 50,000 lbf/in.

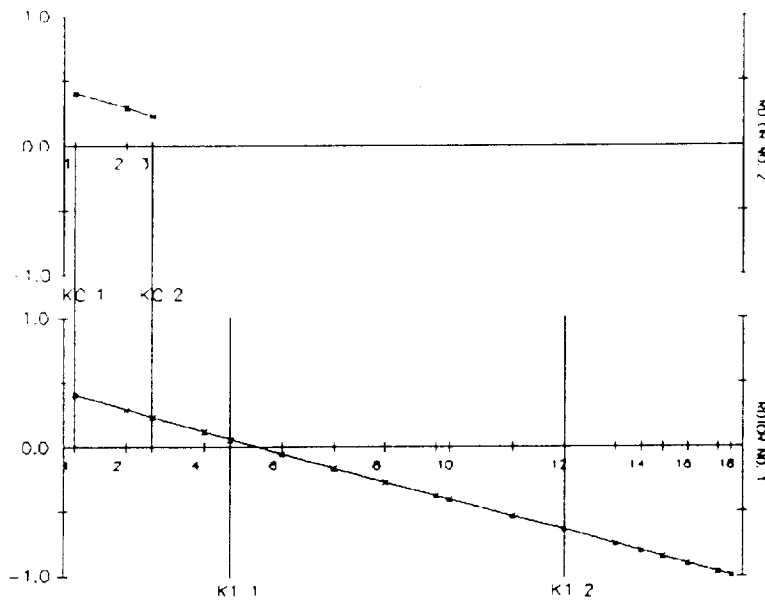


N = 462069. RPM



Liquid Hydrogen Boil-off Recovery System
Parameter Sensitivity Study
June 6, 1998 CDA

N = 505440. RPM



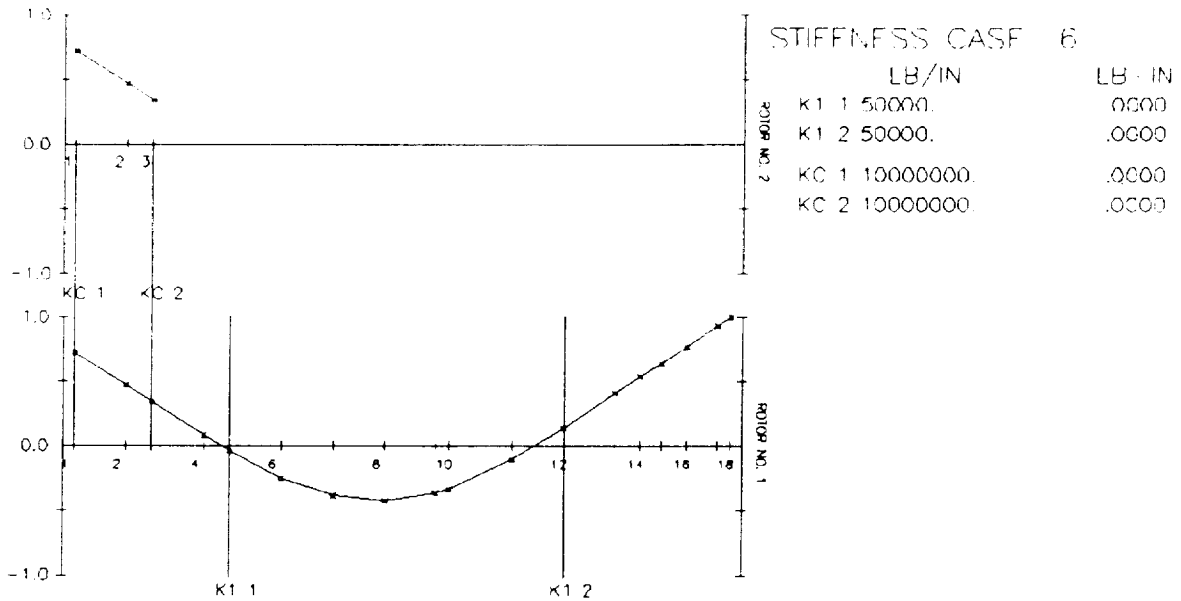
STIFFNESS CASE 6

	LB/IN	LB-IN
K1 1	50000.	.0000
K1 2	50000.	.0000
KC 1	10000000.	.0000
KC 2	10000000.	.0000

Liquid Hydrogen Boil-off Recovery System
Parameter Sensitivity Study
June 6, 1998

CDA

N = 2289703. RPM



Liquid Hydrogen Boil-off Recovery System
 Parameter Sensitivity Study
 June 6, 1998 CDA

The critical speed map plots the first four modes for a range of bearing stiffness from 1000 to 250,000 lbf/in at the two bearing locations. The mode shapes illustrate that the first two modes are rigid body modes associated with the overhung compressor and turbine. (The two shafts shown in the mode shape represent the actual rotor displacement and a shorter dummy rotor required by the analytical method.) The third mode is the first bending mode of the rotor. The bending modes are highly sensitive to unbalance in the rotor. These produce large bearing reactions and shaft vibrations. These modes require separation from the operating range to ensure smooth trouble free operation.

The frequencies for the critical speeds will be used as the baseline numbers and are based on the Phase I layout of the rotor. While used as a baseline, the critical speed map does show an important consequence of the current rotor design. The bending mode is located far above the operating speed and is insensitive to the bearing stiffness. At greater stiffness levels, the two rigid body modes approach the operating speed of 1,300,000 rpm.

Shaft Diameter

The shaft diameter was varied by $\pm 25\%$ of its current value. The critical speed calculation was carried out for each case and the results are tabulated below as a frequency and a percentage change over the baseline.

Bearing Stiffness (lbf/in)	<u>Shaft Diameter +25%</u> Critical Speed (rpm)		
	1	2	3
10,000	173,485	189,832	2,947,682
50,000	386,946	423,381	2,949,694
250,000	854,415	934,364	2,960,506
Bearing Stiffness (lbf/in)	<u>Shaft Diameter -25%</u> Critical Speed (rpm)		
10,000	252,705	286,888	1,573,624
50,000	554,211	632,967	1,585,708
250,000	1,109,307	1,308,506	1,694,537

What is apparent from the changes in the shaft diameter is that an increased diameter increases the frequency of the bending mode (3rd) and decreases the frequency of the rigid body modes (1st & 2nd). Since the bending mode is strongly affected by the shaft stiffness, a larger diameter shaft will have bending modes with higher frequencies. Since the absolute change in frequency was equal for an increase or decrease in diameter, only detrimental changes will be examined for the remaining design parameters.

Bearing Span, Thrust Disk Size, Compressor and Turbine Weight

The effects of increasing the bearing span and thrust disk size by 25% and the compressor and turbine weight by 100% were examined next. The results are tabulated below:

Bearing Stiffness (lbf/in)	<u>Bearing Span +25%</u> Critical Speed (rpm)		
	1	2	3
10,000	198,213	225,116	1,746,143
50,000	439,857	499,760	1,755,880
250,000	942,618	1,072,611	1,822,723
Bearing Stiffness (lbf/in)	<u>Thrust Disk Size +25%</u> Critical Speed (rpm)		
10,000	205,807	225,129	2,239,661
50,000	457,811	500,206	2,244,782
250,000	997,541	1,081,100	2,275,876
Bearing Stiffness (lbf/in)	<u>Compressor Weight +100%</u> Critical Speed (rpm)		
10,000	136,330	208,623	1,079,786
50,000	287,899	464,168	1,134,044
250,000	501,851	1,012,338	1,393,301
Bearing Stiffness (lbf/in)	<u>Turbine Weight +100%</u> Critical Speed (rpm)		
10,000	125,602	223,984	1,706,844
50,000	273,885	498,138	1,740,010
250,000	544,636	1,082,898	1,902,393

The increase in bearing span, possibly necessitated by an increase in bearing length, thrust disk enlargement or spatial restrictions on the exterior of the case, has a large impact on the location of the bending mode. Increased bearing span, i.e. shaft length, has an inverse relationship with the shaft stiffness. As with the shaft diameter, a decrease in shaft stiffness will lower the frequency of the bending mode. In this case, a 25% increase in span has dropped the bending mode by an equivalent amount. As can be seen in the table, the rigid body modes are not significantly affected by the increase in bearing span.

To examine thrust disk changes due to performance variations in either the compressor, turbine, or the thrust disk itself, a 25% increase in the diameter and thickness was analyzed. The results indicate that this magnitude of change does not affect the dynamic behavior of the rotor. Frequencies of the rigid and bending modes changed only slightly.

Performance variations, due to inaccurate predictions, machining errors, or changes in inlet/exit conditions, will also affect the compressor and turbine design. One of the impacts of these design changes is an increase the overhung weight at the shaft ends. A study was performed where the component weight at each end of the shaft was increased by 100%. While this may seem a large increase, changes to the overhung length in shaft and, not only, design changes to the turbine and compressor, will add weight in a similar fashion. Additionally, the results can be accurately interpolated for fractional changes in weight.

The increase in compressor weight had the greatest impact on the location of the critical speeds. Of great interest is the drop in frequency of the bending mode. For the increase in compressor weight noted, the bending mode has fallen below the operating speed of 1,300,000 rpm. This would impair operation of the rotor system.

The increase in turbine weight had a lesser impact on the frequency of the bending mode. The table shows a decrease of only 10% in frequency. The differences are due in part to the smaller overhang of the turbine versus the compressor.

Bearing Stiffness & Damping

Since the effects due to variations in the bearing damping can not be measured using an undamped analysis, the rotor's response to unbalance will be used. This is a forced response analysis and incorporates the bearing stiffness and damping characteristics. The predicted response at the turbine, mid-span and compressor will be used as the basis for comparison. The peak response and response at 1,300,000 rpm speed will be monitored for changes. Stiffness will be varied by the predicted curves for minimum, nominal and maximum clearance. Damping levels will be multiplied by $\frac{1}{2}$ and 2. A fixed level of unbalance placed at the turbine and compressor locations is used throughout the analysis. The magnitude of the unbalance is not meant as representative of expected levels, but merely selected to produce sufficient response levels for the analysis.

An additional measure of behavioral change for variations in damping is the stability of the rotor/bearing system. The log decrement is used to represent the system stability level. A positive log decrement indicates stable system.

Location	Baseline		
	Peak Response (mils)	Frequency (rpm)	Response @ 1,300,000 rpm
Turbine	2.34	320,000	1.88
Mid-Span	0.45	"	0.48
Compressor	2.61	"	0.25
	Stiffness (+)		
Turbine	7.29	640,000	3.86
Mid-Span	2.45	710,000	1.04
Compressor	9.01	710,000	2.13
	Stiffness (-)		
Turbine	1.57	580,000	1.55
Mid-Span	0.29	310,000	0.40
Compressor	1.62	310,000	0.39
	Damping (1/2x)		
Turbine	2.91	230,000	1.86
Mid-Span	0.62	"	0.48
Compressor	3.43	"	0.13
	Damping (2X)		
Turbine	1.90	600,000	1.86
Mid-Span	0.36	470,000	0.47
Compressor	1.93	"	0.49

Damping Levels	Log Decrement of Critical Speed		
	1	2	3
Baseline	0.697	0.693	0.012
½ x	0.343	0.337	0.0051
2 x	1.43	1.43	0.025

In the undamped analysis, increased stiffness due to the tighter clearance condition increased the frequency of the rigid body modes. The unbalance response analysis also predicted an increase in the peak response speed, roughly doubled. In addition, the response due to the unbalance also increases in some cases 3-4x the baseline values. In contrast, the reduced stiffness case corresponding to maximum clearance, has a minimal effect on the frequency of the peak response and lowers the response levels by 30-40%. These results indicate that at the higher stiffness levels, the bearing damping is less effective in controlling the rotor response at the turbine and compressor than at the lower stiffness levels.

In dynamic systems, damping is effective in reducing the vibration levels at speeds near or corresponding to critical speeds. Surprisingly, at speeds removed from critical speeds, increased damping levels will increase the response level of the rotor. This can be seen in the table. At the operating speed of 1,300,000 rpm, lower response levels are achieved at the compressor end with smaller damping levels as expected. However and more importantly, the peak response magnitude drops with increasing damping. Since this represents the maximum predicted vibration, it is the critical factor in determining the operability of the rotor.

Using an arbitrary level of destabilizing force in the rotor, stability of the rotor system improves as the damping is increased. This is as expected and indicates that excessive damping levels have not been reached. (Note: As with stiffness, unnecessarily large levels of damping will decrease the effectiveness of the damping in controlling the response of the turbine and compressor shaft ends to unbalance and improving the rotordynamic stability of the system.)

Recommendations

The following factors should be maximized to improve the dynamic behavior of the rotor/bearing system:

- *Shaft Diameter* - Increases in the shaft diameter lower the frequency of the rigid body modes and raise the bending modes. This enlarges the effective separation region in which trouble free operation can be expected.
- *Bearing Damping* - The reduction of the peak response levels and the increase in rotor stability indicate that optimal damping levels have not been reached. Bearing damping levels can usually be increased by lengthening the bearing. However, this does raise the sensitivity of the bearing stiffness to clearance and increase the bearing span, both detrimental effects.

The following are design items or details that should be minimized during the final design stages of the system:

- *Bearing Span* - Increases in the bearing span will lower the frequency of the first bending mode. This could place restrictions on the maximum safe operating speed.
- *Bearing Stiffness* - The study indicates that stiffness levels from 10,000 to 50,000 lbf/in are more desirable for the present rotor configuration than 250,000 lbf/in. The sensitivity of the stiffness to clearance changes can be reduced by shortening the bearing length, however this has a negative impact on the damping (see above.)
- *Overhung Weight* - The overhung weight (and moment) at the shaft ends should be kept as small as possible. This is especially true at the compressor end. The location of the bending mode is strongly dependent on the overhung weight at this location.
- *Thrust Disk* - While only a minor effect on the dynamic behavior, drastically increasing the size of the thrust disk will add weight to the center of the rotor. This will lower the frequency of the bending mode and may eventually encroach upon the operating speed.

Appendix C

Consultant's Report – Final Rotordynamic Analysis

.....
Critical Design Analysis

***Self-Acting, Liquid Hydrogen
Boil-Off Recovery System***

.....
*Final Turbocompressor Configuration
Rotordynamic Analysis*

Self-Acting, Liquid Hydrogen Boil-Off Recovery System

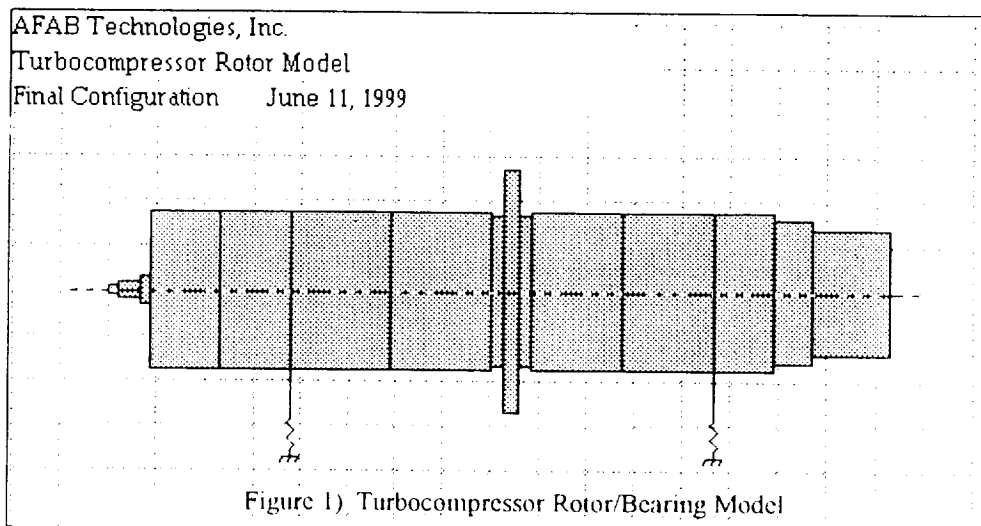
Final Turbocompressor Configuration Rotordynamic Analysis

Introduction

The final configuration of the turbocompressor rotor was provided by AFAB Technologies, Inc. The dimensions of the shaft were taken from drawing AT98003, 10/1/98. As with previous configurations, the dynamic behavior and integrity of the design is measured by performing a rotordynamic analysis. The analysis includes an undamped critical speed study, unbalance response calculation and a stability prediction.

The shaft material is titanium. Correspondingly, the density and Young's modulus used were 0.167 lbm/in^3 and $14.8 \times 10^6 \text{ lbf/in}^2$. The pitch diameter was used to model the mass and inertia of the compressor and turbine blading. Since the blading occurs at the shaft ends, shaft stiffness contributions of these components are negligible. Maximum operating speed is defined as 1,100,000 rpm.

The rotor/bearing system of the turbocompressor is displayed on Figure 1). The shaft is divided into 16 mass stations, each having a length-to-diameter ratio of less than 1.0. The beginning of each mass station contains the mass and inertia effects the surrounding shaft. Shaft stiffness is modeled in massless elements connecting the mass stations.



Grid spacing shown is 0.1". The overall length of the rotor is roughly 1.6" and the bearing span is ≈ 0.87 ". Bearing positions are indicated by the vertical spring schematics.

Undamped Critical Speed Analysis

The undamped analysis is used to give a general idea of the locations of the critical speeds and mode shapes of the turbocompressor. In this analysis, the bearing support stiffness is assumed and varied from 5000 to 500,000 lbf/in. Damping is neglected.

The first four mode shapes and corresponding frequencies for a support stiffness of 5000 lbf/in are shown on Figure 2). The first two modes are considered rigid body modes showing little bending in the shaft. Given this support stiffness, these would be expected to occur near 128,000 rpm in the operating range. The bearings are expected to absorb most of the potential energy of these modes since the shaft is behaving as a rigid body. The first two undamped bending modes occur at speeds above 1,500,000 rpm. These modes should be avoided during operation of rotating equipment. Since the energy produced by rotating forces is absorbed by the shaft bending, the bearing have little control on the amplitudes of vibration.

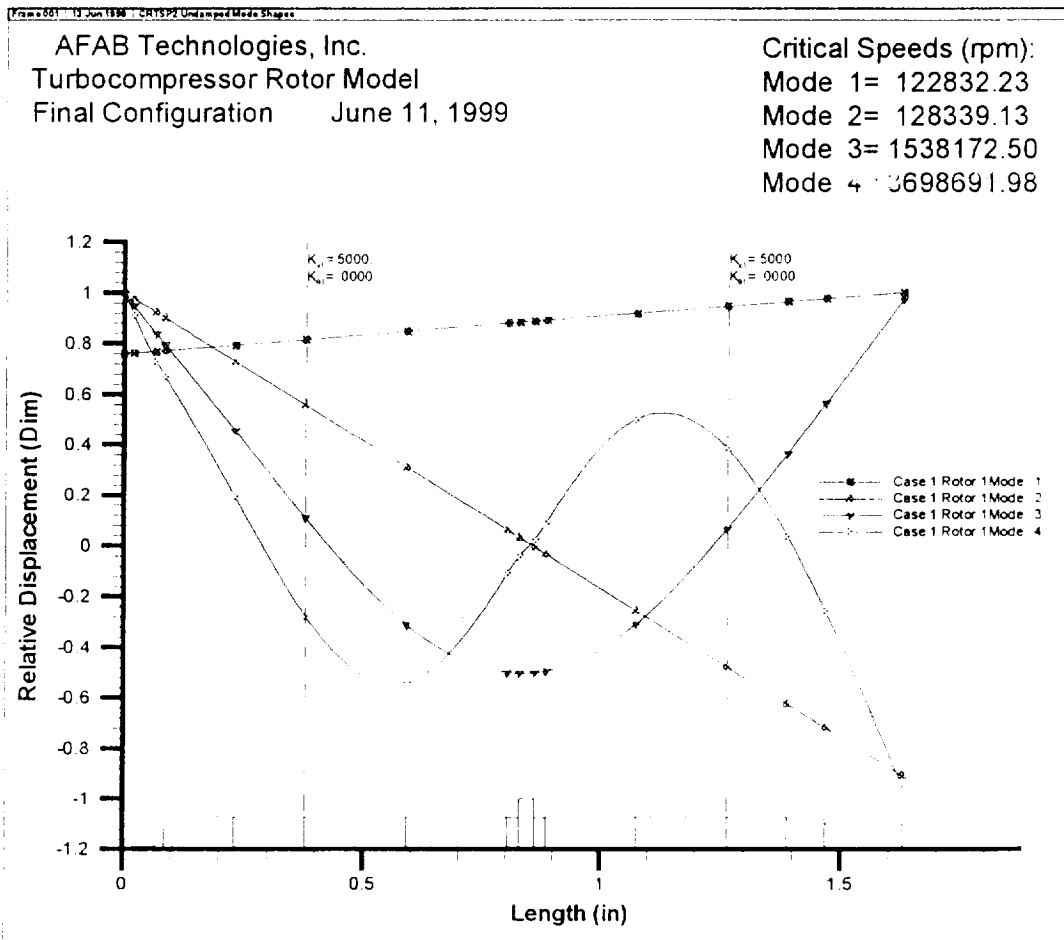


Figure 2) Undamped Mode Shapes at 5000 lbf/in

The analysis is repeated using a support stiffness of 500,000 lbf/in. In this instance, the bearing stiffness is now a larger percentage of the bending stiffness of the shaft. As expected, the first two mode shapes of the shaft now show some bending. Since the bearings are assumed stiffer by two orders of magnitude, shaft bending is now absorbing some of the potential energy. Additionally, the increased support stiffness has moved the frequency of these modes to $\approx 1,200,000$ rpm. To avoid operating near these critical speeds, bearing stiffness should be kept less than 500,000 lbf/in. The first two bending modes are still above 1,500,000 rpm and show little effects of the increase in support stiffness. This is due in part to the fact that the node points of these modes are occurring near the bearing locations.

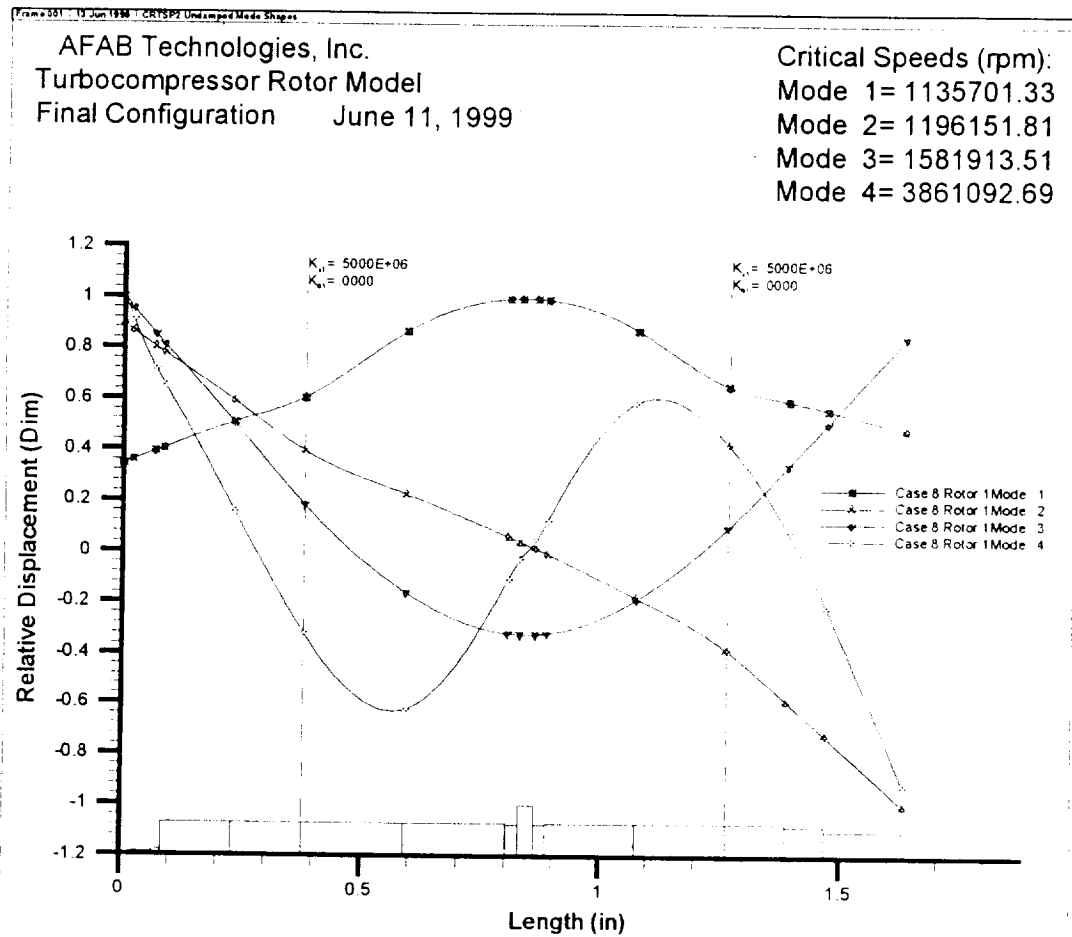


Figure 3) Mode Shapes at 500,000 lbf/in

AFAB Technologies, Inc.
Turbocompressor Rotor Model
Final Configuration June 11, 1999

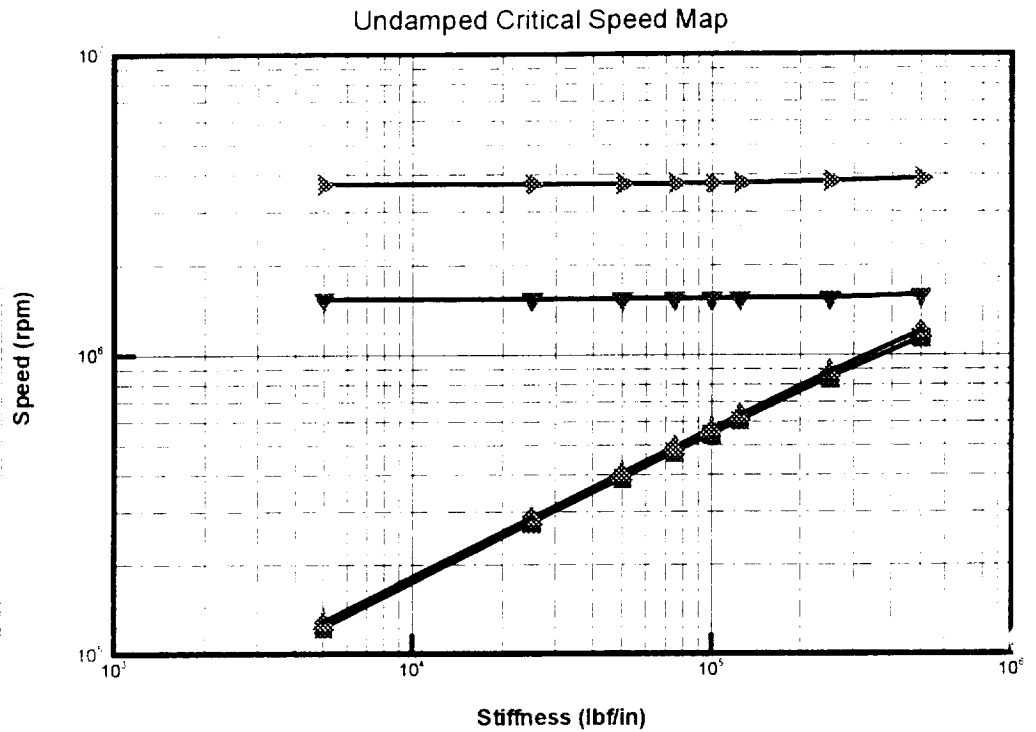


Figure 4) Undamped Critical Speed Map

Unbalance Response Analysis

The unbalance response analysis is used to determine how the rotor will react to unbalances caused by manufacturing deviations, machining tolerances, and wear. Three unbalance cases are examined in this study; compressor, turbine, and thrust disk unbalance. The turbine and compressor unbalance distributions should excite the first two modes predicted by the undamped analysis. The thrust disk unbalance will excite the first bending mode since it is located at the rotor center near the maximum deflection of that mode. Unbalance magnitudes of 0.00001 oz-in are used. However, the response is linear and can be directly scaled with unbalance levels.

The predicted bearing behavior versus speed is used in this study. Both stiffness and damping coefficients are incorporated in the calculations. As with the undamped analysis, the bearing stiffness determines the location of the critical speeds. The damping will determine to what extent the rotor will respond to the unbalance excitation. (As noted before, poor placement of the critical speeds, either by the shaft design or bearing stiffness, may hamper the effectiveness of the bearing damping in controlling the motion of the shaft.) The bearing coefficients used are contained in Table 1).

Speed (rpm)	Stiffness (lbf/in)	Damping (lbf-sec/in)
500,000	18,000	0.18
1,000,000	40,000	0.25
1,500,000	70,000	0.37

Table 1) Bearing Stiffness and Damping vs. Speed

Since the bearing coefficients are predicted to be symmetric (X dir = Y dir), the rotor response in the X- & Y-directions will be identical as well. The rotor response will be presented as the amplitude and phase angle at the compressor, thrust disk and turbine locations. Critical speeds are normally identified as peaks in the response curves. Additionally, rapid changes in the phase angle are also usually connected with the presence of a critical speed.

The first case presented is the rotor response to turbine unbalance. Figures 5-7) plot the response of the three stations. Notice that no peaks are evident in the response especially near the operating speed of 1,100,000 rpm. It is likely that the first two modes are occurring near 200,000 rpm. However, the bearings are effective in damping out the response of these rigid body modes. (The rapid phase change evident in the turbine response is due to the transition of the mode shape from conical to bending. The turbine response passes through zero at this point.)

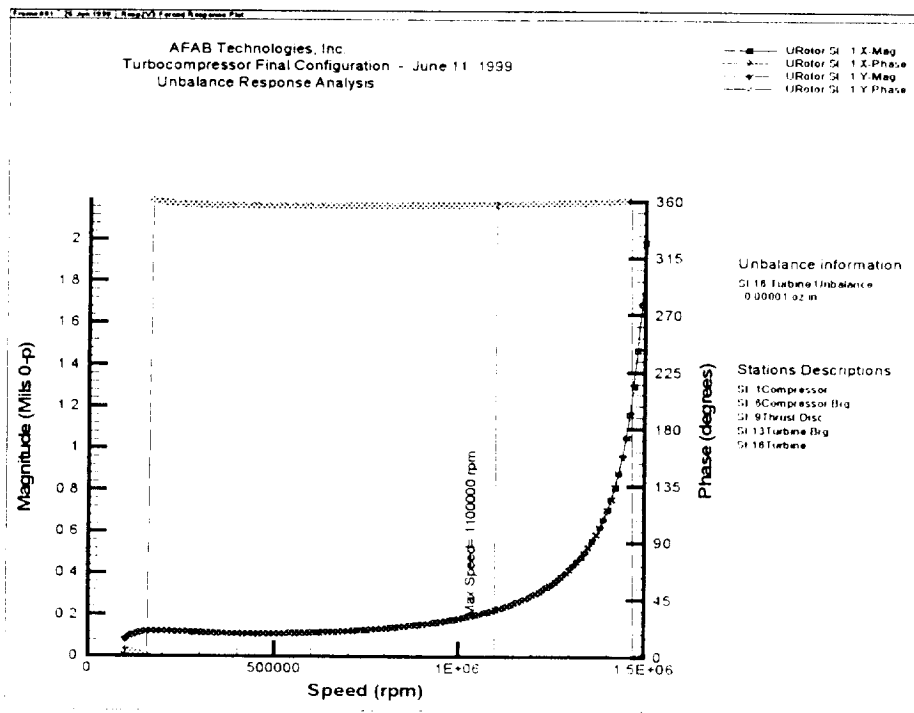


Figure 5) Turbine Unbalance -- Compressor Response

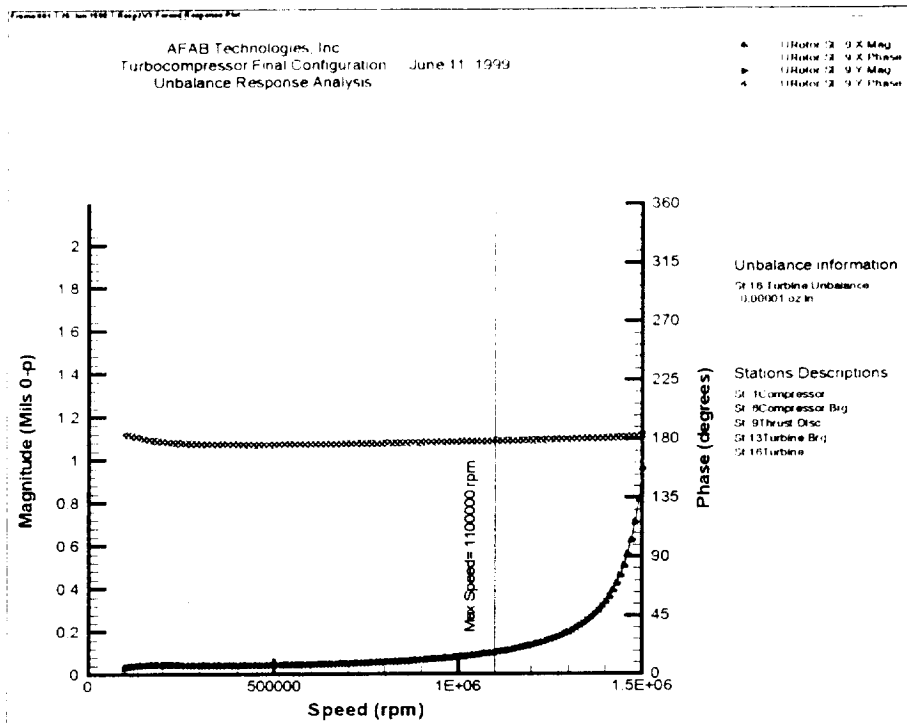


Figure 6) Turbine Unbalance – Thrust Disk Response

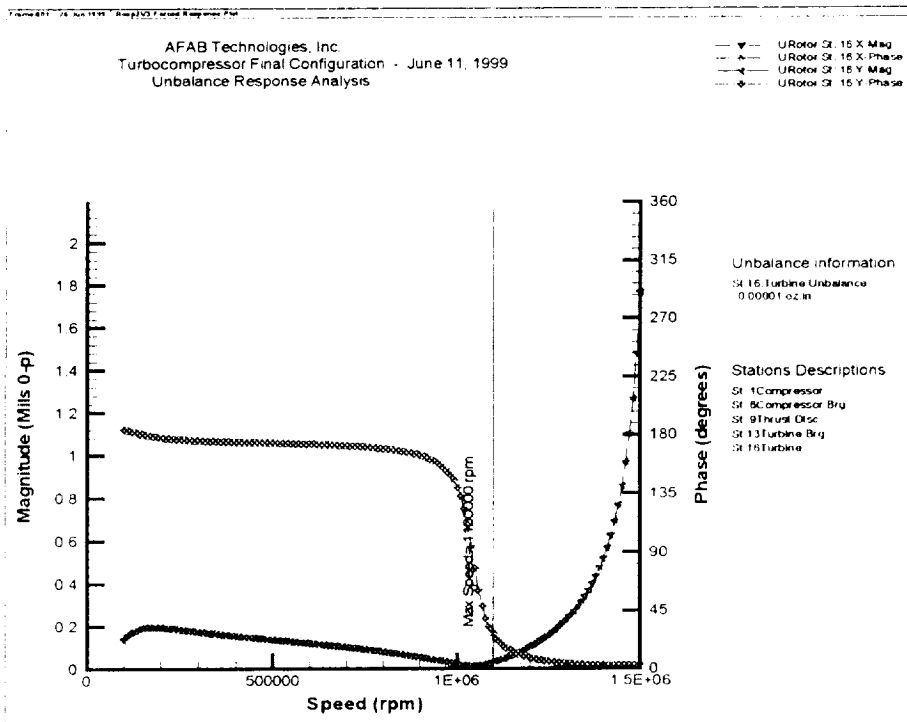


Figure 7) Turbine Unbalance – Turbine Response

The second case presented is the rotor response to compressor unbalance. Figures 8-10) plot the response of the three stations. Once again, no peaks are evident in the response especially near the operating speed of 1,100,000 rpm. As before, it is likely that the first two modes are occurring near 200,000 rpm. (The rapid phase change is evident in the compressor response as it passes through zero at this point.)

Finally, the response due to thrust disk or mid-span unbalance is presented. This distribution is intended to excite the third mode or first bending mode of the turbocompressor. It is predicted to occur above 1,500,000 rpm so the peak response will not be seen. Figures 11-13) contain the predicted response at the same three stations as before. No peaks are evident. However, the rapid rise in the response near the 1,500,000 rpm speed is indicative of the close proximity to a bending mode of the system. (The rapid phase change is evident in the thrust disk response as it passes through zero at this point.)

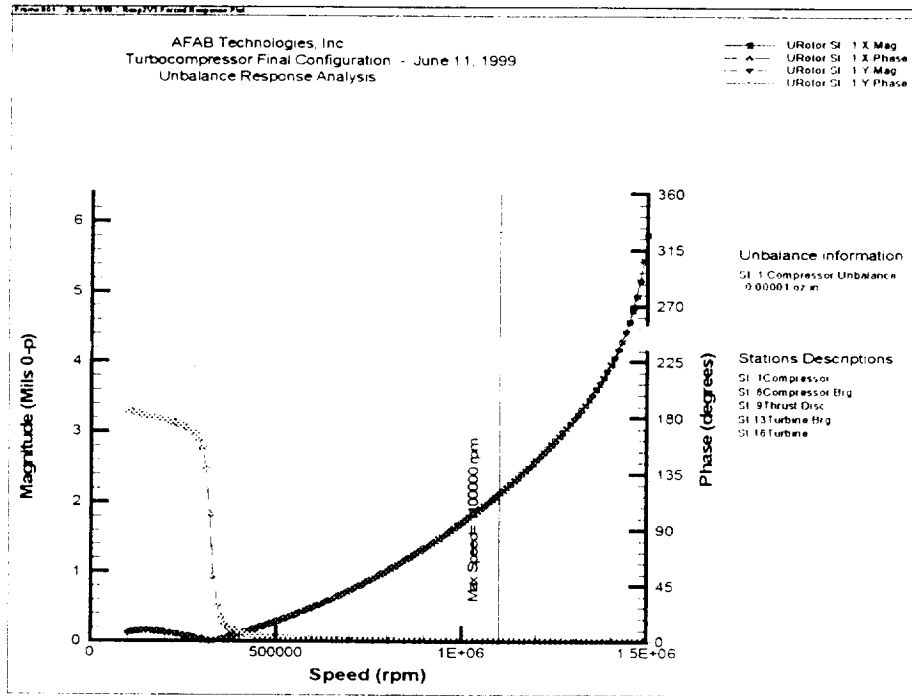


Figure 8) Compressor Unbalance – Compressor Response

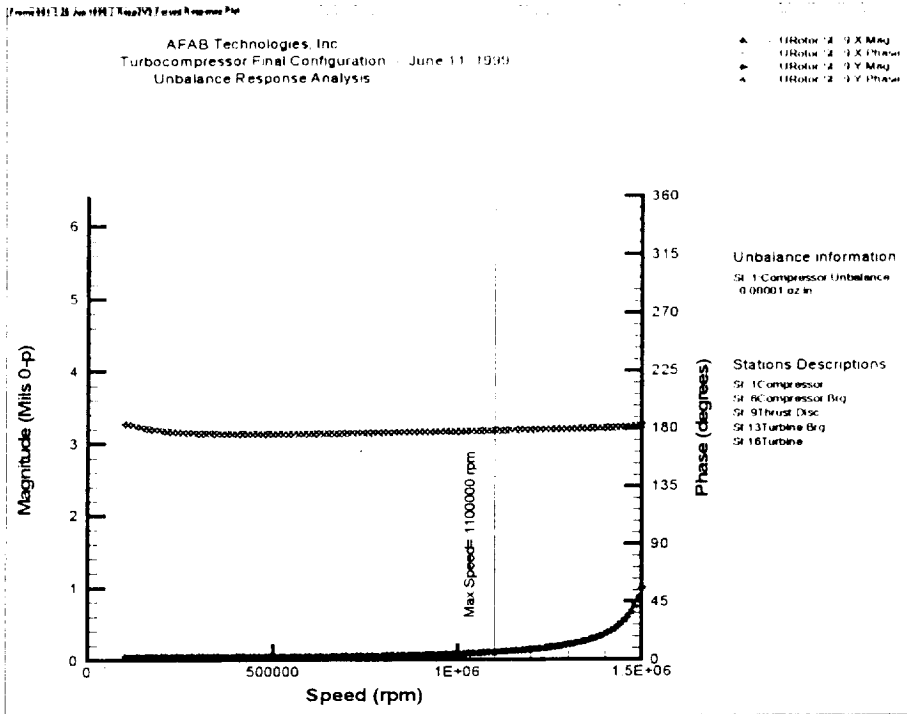


Figure 9) Compressor Unbalance – Thrust Disk Response

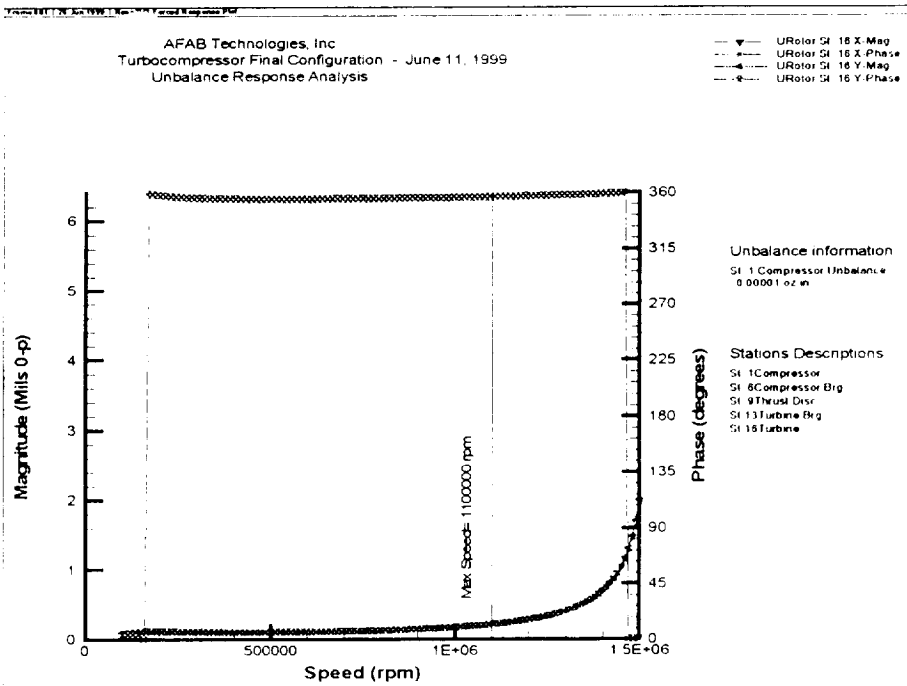


Figure 10) Compressor Unbalance – Turbine Response

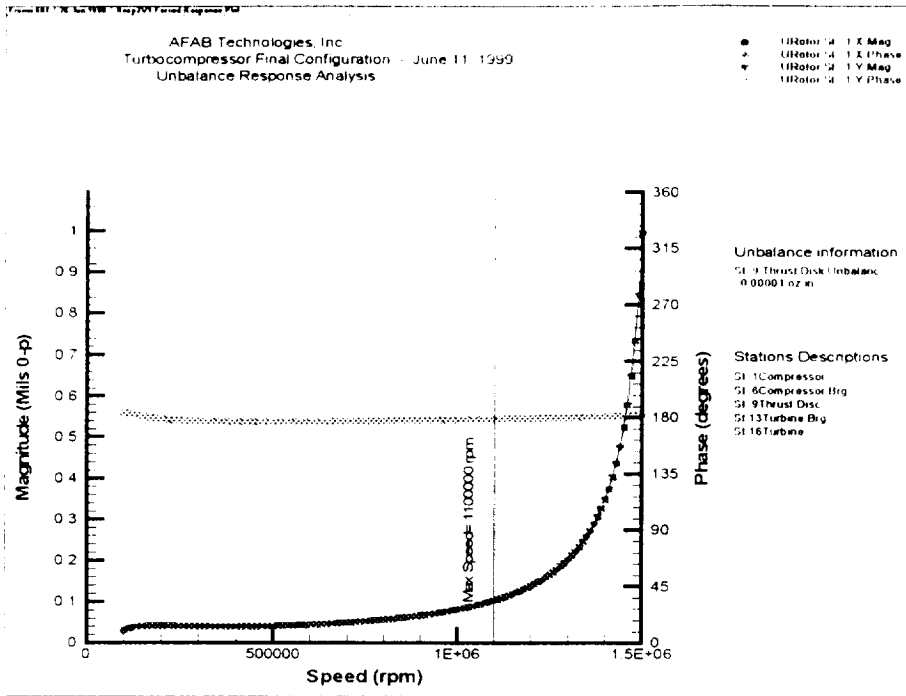


Figure 11) Thrust Disk Unbalance – Compressor Response

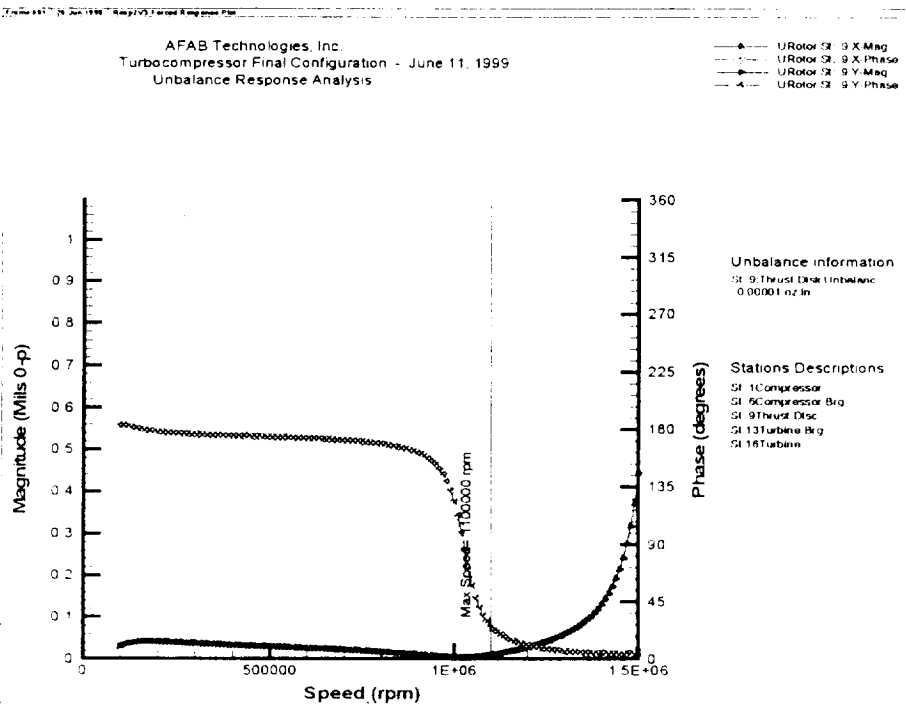


Figure 12) Thrust Disk Unbalance – Thrust Disk Response

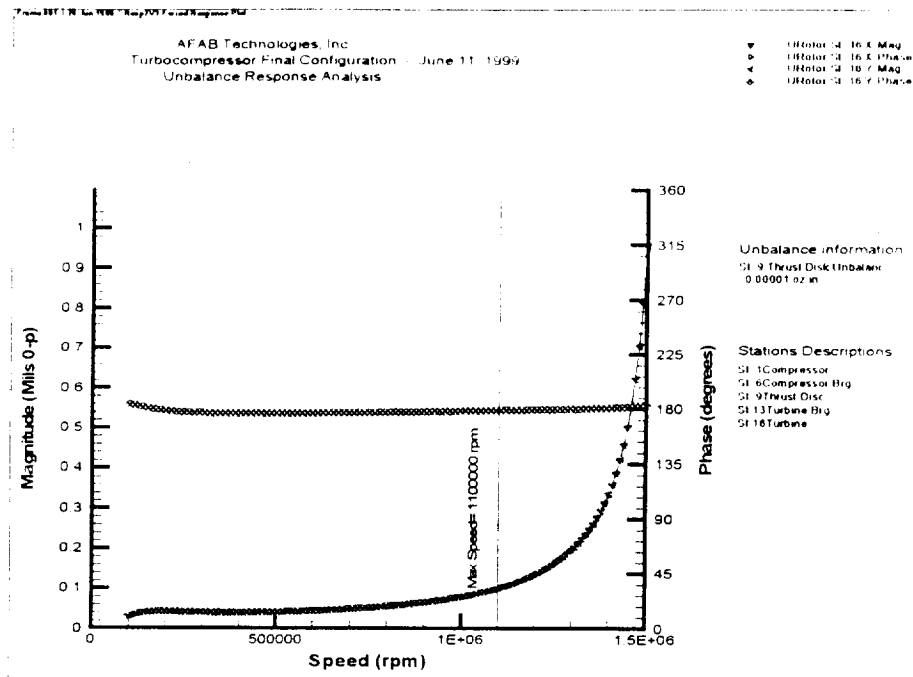


Figure 13) Thrust Disk Unbalance – Turbine Response

Stability Analysis

The rotor stability is critical to enable operation at full speed. Rotor instability can be caused by many factors including the aerodynamic forces in compressors and turbines. Rotor instability normally appears as a re-excitation of the first critical speed. This occurs while the rotor is operating at speeds greater than twice the frequency of the first mode. The vibration can become unbounded and lead to severe rotor damage and large transmitted forces.

Stability is measured by the logarithmic decrement (log dec). A stable system will have vibration levels that will return to normal levels after experiencing a perturbation (positive log dec). An unstable system will have levels that grow nearly unbounded following the perturbation (negative log dec).

Figure 14) illustrates the rotor model used in the stability analysis. Two additional springs are shown at the compressor and turbine locations. These represent the destabilizing forces placed at these locations. The destabilizing force is a cross-coupled stiffness term. Cross-coupling causes a movement in a direction perpendicular to the applied force. A cross-coupled stiffness term induces whirl or the tendency towards unbounded growth in the vibrations. The bearing damping counteracts these terms. A magnitude of 300 lbf/in is placed at each location. This is considerably larger than expected for this size of equipment operating in hydrogen.

The results of the stability analysis are shown on Table 2). The operating speed used in the analysis is 1,100,000 rpm. Maximum speed represents the worst case scenario for the analysis.